

คลังเตอร์ของคาร์บอนนาโนสเฟียร์เพื่อเป็นตัวนำส่งยา



นางสาวจิราพร สีหมอก

จุฬาลงกรณ์มหาวิทยาลัย

CHULALONGKORN UNIVERSITY

บทคัดย่อและแฟ้มข้อมูลฉบับเต็มของวิทยานิพนธ์ตั้งแต่ปีการศึกษา 2554 ที่ให้บริการในคลังปัญญาจุฬาฯ (CUIR)

เป็นแฟ้มข้อมูลของนิสิตเจ้าของวิทยานิพนธ์ ที่ส่งผ่านทางบัณฑิตวิทยาลัย

The abstract and full text of theses from the academic year 2011 in Chulalongkorn University Intellectual Repository (CUIR)

are the thesis authors' files submitted through the University Graduate School.

วิทยานิพนธ์นี้เป็นส่วนหนึ่งของการศึกษาตามหลักสูตรปริญญาวิทยาศาสตรดุษฎีบัณฑิต

สาขาวิชาปิโตรเคมี

คณะวิทยาศาสตร์ จุฬาลงกรณ์มหาวิทยาลัย

ปีการศึกษา 2558

ลิขสิทธิ์ของจุฬาลงกรณ์มหาวิทยาลัย

CLUSTER OF CARBON NANOSPHERES AS DRUG CARRIER

Miss Jiraporn Seemork



A Dissertation Submitted in Partial Fulfillment of the Requirements
for the Degree of Doctor of Philosophy Program in Petrochemistry

Faculty of Science

Chulalongkorn University

Academic Year 2015

Copyright of Chulalongkorn University

Thesis Title	CLUSTER OF CARBON NANOSPHERES AS DRUG CARRIER
By	Miss Jiraporn Seemork
Field of Study	Petrochemistry
Thesis Advisor	Associate Professor Supason Wanichwecharungruang, Ph.D.
Thesis Co-Advisor	Associate Professor Tanapat Palaga, Ph.D.

Accepted by the Faculty of Science, Chulalongkorn University in Partial Fulfillment of the Requirements for the Doctoral Degree

..... Dean of the Faculty of Science
(Associate Professor Polkit Sangvanich, Ph.D.)

THESIS COMMITTEE

..... Chairman
(Assistant Professor Warinthorn Chavasiri, Ph.D.)

..... Thesis Advisor
(Associate Professor Supason Wanichwecharungruang, Ph.D.)

..... Thesis Co-Advisor
(Associate Professor Tanapat Palaga, Ph.D.)

..... Examiner
(Associate Professor Voravee Hoven, Ph.D.)

..... Examiner
(Professor Mongkol Sukwattanasinitt, Ph.D.)

..... External Examiner
(Prasat Kittakoop, Ph.D.)

..... External Examiner
(Kriengsak Lirdprapamongkol, Ph.D.)

จิราพร สีมอก : คลัสเตอร์ของคาร์บอนนาโนสเฟียร์เพื่อเป็นตัวนำส่งยา (CLUSTER OF CARBON NANOSPHERES AS DRUG CARRIER) อ.ที่ปรึกษาวิทยานิพนธ์หลัก: รศ. ดร.ศุภคร วณิชเวชารุ่งเรือง, อ.ที่ปรึกษาวิทยานิพนธ์ร่วม: รศ. ดร.ธนาภัทร ปาลกะ, 83 หน้า.

เป็นการเตรียมคลัสเตอร์ของคาร์บอนนาโนสเฟียร์ (cluster of carbon nanospheres) หรือเรียกอีกชื่อหนึ่งว่า oxidized carbon nanospheres (OCSs) เพื่อใช้สำหรับเป็นตัวนำส่งยา โดยได้ทำการเปรียบเทียบประสิทธิภาพในการนำส่งกับสารในกลุ่มเดียวกันซึ่งเป็น oxidized carbon particulates ที่มีรูปร่างแตกต่างกัน ได้แก่ oxidized carbon nanotubes (OCTs) และ oxidized graphene sheets (OGShs) จากการทดสอบความสามารถในการยึดเกาะกับเซลล์เมมเบรน (lipid bilayer membrane) พบว่าอนุภาค OCSs มีการยึดเกาะที่ดีกับเซลล์เมมเบรน และสามารถแทรกผ่านเข้าไปในไลโปโซม ซึ่งใช้เป็นโมเดลจำลองของเซลล์สิ่งมีชีวิต เมื่อเทียบกับอนุภาคแบบอื่น ในขณะที่ OCTs มีการยึดเกาะกับเซลล์เมมเบรนในระดับปานกลาง และ OGShs ไม่สามารถยึดเกาะกับเซลล์เมมเบรนได้ เมื่อพิจารณาผลของชนิดลิปิด ที่เป็นองค์ประกอบของเซลล์เมมเบรน พบว่า OCSs มีการยึดเกาะที่ดีกว่ากับเมมเบรนที่ประกอบด้วยลิปิดที่จัดเรียงตัวแบบไม่เป็นระเบียบ ซึ่งเมมเบรนชนิดนี้จะมีความเป็นของไหลมากกว่าเมมเบรนที่ประกอบด้วยลิปิดที่จัดเรียงตัวแบบเป็นระเบียบ ส่งผลให้ free energy ในการโค้งงอของเมมเบรนมีค่าต่ำกว่า นอกจากนี้อนุภาค OCSs ยังสามารถนำส่งสารต่างๆ เข้าไปได้ทั้งในไซโทพลาสซึมและนิวเคลียสของเซลล์มะเร็งปอด (A 549) ซึ่งในงานวิจัยนี้ใช้ curcumin เป็นโมเดลของสารที่ต้องการนำส่ง ในขณะที่ OCTs สามารถนำส่ง curcumin เข้าไปได้ในไซโทพลาสซึม และ OGShs ไม่สามารถนำส่งได้ นอกจากนี้ยังพบว่าการดัดแปลงพื้นผิวของอนุภาค โดยการเติมสายโซ่พอลิเอทิลีนไกลคอล (mPEG) จะลดความสามารถของอนุภาคในการยึดเกาะกับเมมเบรน จากผลการทดสอบฤทธิ์การทำลายเซลล์มะเร็ง พบว่าอนุภาค OCSs สามารถนำส่งยาต้านมะเร็งทั้งแบบที่ละลาย และไม่ละลายน้ำเข้าไปในเซลล์มะเร็งปอดได้ และยังพบว่าในกรณีของยาที่ไม่ละลายน้ำ การนำส่งด้วย OCSs สามารถให้ฤทธิ์การทำลายเซลล์มะเร็งที่เทียบเท่ากับการใช้ยาในตัวทำละลายอินทรีย์ ซึ่งเป็นข้อดีของการใช้อนุภาคชนิดนี้ในการนำส่ง เนื่องจากสามารถหลีกเลี่ยงการใช้ตัวทำละลายอินทรีย์ในระบบนำส่งได้

สาขาวิชา ปีโตรเคมี

ปีการศึกษา 2558

ลายมือชื่อนิสิต

ลายมือชื่อ อ.ที่ปรึกษาหลัก

ลายมือชื่อ อ.ที่ปรึกษาร่วม

5572805623 : MAJOR PETROCHEMISTRY

KEYWORDS: CLUSTER OF CARBON NANOSPHERES / LIPID BILAYER MEMBRANE / SHAPE / ANTI-CANCER

JIRAPORN SEEMORK: CLUSTER OF CARBON NANOSPHERES AS DRUG CARRIER.
 ADVISOR: ASSOC. PROF. SUPASON WANICHWECHARUNGRUANG, Ph.D., CO-ADVISOR:
 ASSOC. PROF. TANAPAT PALAGA, Ph.D., 83 pp.

Cluster of carbon nanospheres, or the so called oxidized carbon nanospheres (OCSs) were successfully synthesized. The use of OCSs as drug carrier was, then, investigated by comparison to the different shaped oxidized carbon particulates, oxidized carbon nanotubes (OCTs) and oxidized graphene sheets (OGShs). The result reveals that OCSs possessed highest ability to associate with lipid bilayer membrane and highest level of penetration into cell-sized liposomes, whereas OCTs showed the moderate adhesion with lipid membrane without liposome penetration and OGShs exhibited no adhesion to the membrane. Regarding lipid composition of the membrane, the OCSs more preferably adhere on the liquid-disordered (Ld) membrane (composes of high fluidity lipid molecules) as compared to the liquid-ordered (Lo) membrane (composes of less fluid lipid molecules), owing to the more favorable free energy of membrane curvature. OCSs could effectively deliver cargo, here curcumin was used as model cargo, into A549 lung cancer cells and allowed accumulation of curcumin in both cytoplasm and nucleus of the cells. OCTs could induce only moderate uptake of curcumin into the cytosol of the cells, whereas OGShs were rarely internalized into cells. Surface modification of oxidized carbon particulates by mPEG decreases their ability to associate with lipid bilayer membrane. In addition, the OCSs could deliver both hydrophobic and hydrophilic anti-cancer drugs into cancer cells, A549 and A549RT-eto. The results reveal that delivering of paclitaxel, which is a hydrophobic drug, by OCSs showed anti-cancer activity at the same level as use of the free drug in DMSO. This could be implied that delivery by OCSs improve cellular uptake ability of the water insoluble drug and avoid use of organic solvent.

Field of Study: Petrochemistry

Academic Year: 2015

Student's Signature

Advisor's Signature

Co-Advisor's Signature

ACKNOWLEDGEMENTS

First and foremost, I would like to express my deepest appreciation and gratitude to my supervisor, Associate Professor Supason Wanichwecharungruang, for her great supervision, helpful suggestion, thoughtful guidance and kind support to complete my doctoral study. I would not have been able to complete my degree without her farsighted advice and professional encouragement. I also appreciate my co-advisor, Associate Professor Tanapat Palaga, for his contributions of time, knowledge and experience on the biological parts.

Secondly, I would like to give my best appreciation to the members of my committee: Assistant Professor Warinthorn Chavasiri, Associate Professor Voravee Hoven and Professor Mongkol Sukwattanasinitt, of Chulalongkorn University, Dr. Prasat Kittakoop and Dr. Kriengsak Lirdprapamongkol, of Chulabhorn Research Institute for their helpful reviews and comments.

I am profoundly grateful to Associate Professor Tsutomu Hamada and Professor Masayuki Yamaguchi of JAIST for their generous hospitality, support and valuable advice during my completion some parts of the research in Japan. Without their kind support, I would not have been able to achieve and complete my study. I am particularly very grateful to Chulalongkorn University Dutsadiphiphat Scholarship for financial support throughout my doctoral study and CU-JAIST Dual degree program for giving me the great opportunity to be a Ph.D. candidate through this program.

I am indebted to my many colleagues who supported me throughout my study especially to Ms. Khajeelak Chiablaem of Chulabhorn Research Institute, all present and former members of Associate Professor Supason's laboratory, Chulalongkorn University and also members of Hamada laboratory, JAIST. Finally, I would like to extend my deepest gratitude to my beloved family and friends for their unconditional love and support. Without their love, it is definitely hard to finish my Ph.D. degree.

CONTENTS

	Page
THAI ABSTRACT	iv
ENGLISH ABSTRACT	v
ACKNOWLEDGEMENTS	vi
CONTENTS	vii
LIST OF TABLES	xi
LIST OF FIGURES	xii
CHAPTER I INTRODUCTION.....	1
CHAPTER II LITERATURE REVIEWS	3
2.1 Administration Routes	3
2.1.1 Oral	3
2.1.2 Inhalation.....	3
2.1.3 Injection	3
2.1.4 Transdermal	4
2.2 Carrier Types.....	4
2.2.1 Liposomes	4
2.2.2 Polymeric Micelles.....	6
2.2.3 Polymeric Nanoparticles.....	8
2.2.4 Inorganic Nano- or Microparticles.....	10
2.2.5 Viral Delivery	11
2.3 Cellular Uptake.....	12
2.3.1 Active Uptake (Endocytosis)	13
Clathrin-Mediated Endocytosis (CME).....	13

	Page
Caveolae-Mediated Endocytosis	13
Phagocytosis	14
Macropinocytosis	15
2.3.2 Passive Uptake (Non-endocytic Delivery)	15
2.3.3 Endosomal Escape	16
2.3.4 Delivery to Nucleus	18
2.4 Carriers and Uptake Ability	19
2.4.1 Shape.....	20
2.4.2 Size.....	21
2.4.3 Surface Charge.....	23
2.5 Cell-Size liposomes.....	25
2.6 Carbon Materials as Drug Carrier	25
2.6.1 Carbon Nanotubes.....	26
2.6.2 Graphene Oxide	28
2.6.3 PEGylation	30
2.7 Research objective.....	31
CHAPTER III EXPERIMENTAL.....	32
3.1 Synthesis and Characterization of Oxidized Carbon Nanospheres (OCSs), Oxidized Graphene Sheets (OGShs) and Oxidized Carbon Nanotubes (OCTs)...	32
3.2 PEGylation of Oxidized Carbon Nanospheres (OCSs), Oxidized Graphene Sheets (OGShs) and Oxidized Carbon Nanotubes (OCTs) and Characterization	34
3.3 Rhodamine- and Fluorescein-Labeling of Oxidized Carbon Materials	35
3.4 Curcumin Loading	36

	Page
3.5 Anti-cancer Drugs Loading	37
3.6 Liposome Preparation and Interaction of Oxidized Carbon Materials with Lipid Bilayer Membrane.....	38
3.7 Anthocyanin Leakage.....	39
3.8 Penetration of Lipid-loaded OCSs into Liposome.....	39
3.9 Association of Curcumin-loaded OCSs on Lipid Membrane	39
3.10 Adsorption of Lipid on OCSs' Surface at Different pH	40
3.11 Cytotoxicity of Oxidized Carbon Materials.....	40
3.12 Cellular Uptake of Oxidized Carbon Materials.....	41
CHAPTER IV RESULTS AND DISCUSSION	43
4.1 Synthesis and Characterization of Oxidized Carbon Nanospheres (OCSs), Oxidized Graphene Sheets (OGShs) and Oxidized Carbon Nanotubes (OCTs)...	43
4.2 Polyethylene oxide functionalization	50
4.3 Interaction of Oxidized Carbon Materials with Lipid Bilayer Membrane	52
4.3.1 Effect of Particle Shape	52
4.3.2 Effect of Lipid Compositions of liposomes and Surface Functional Group of Oxidized Carbon	56
4.3.3 Effect of Incubation Time.....	58
4.3.4 Effect of Cargo	61
4.3.5 Effect of pH	62
4.4 Cytotoxicity of Oxidized Carbon Materials.....	63
4.5 Cellular Uptake of Curcumin-loaded Oxidized Carbon Materials	64
4.6 Anti-cancer Activity	67
CHAPTER V CONCLUSION	69

	Page
REFERENCES	71
APPENDIX.....	82
VITA.....	83



LIST OF TABLES

Table 3.1 Gradient centrifugation.....	33
Table 4.1 Hydrodynamic diameter, zetapotential and osmolality of oxidized carbon materials and mPEO-OCS.....	48



LIST OF FIGURES

Figure 2.1 Amphiphilic monomers and polymers self-aggregate in water form lamellar bimolecular lipid membranes (BLM), reducing the interphase lipophilic hydrocarbon tails and water. (B) BLM rearrange to spherical liposomes either spontaneously or assisted (i.e.t by shear or ultrasonication) further reduce the tail/water interphase [8].	6
Figure 2.2 Multifunctional polymeric micelles containing super paramagnetic paricles, anti-cancer drug and targeting ligand for targeted drug delivery [29].	7
Figure 2.3 Synthesis of glycidol-chtiosan-deoxycholic (G-CS-DCA) acid and encapsulation of doxorubicin into G-CS-DCA nanoparticles for delivery into cells [49].	9
Figure 2.4 Schematic illustration of (a) chemical structure of disulfide-bridged PCL-SS-PEEP block copolymer and (b) redox-responsive nanoparticles for overcoming multidrug resistance of cancer cells [50].	10
Figure 2.5 Covalently coupling of gold nanoparticles the adenovirus through an amide bond formation [55].	11
Figure 2.6 Cellular uptake of nanoparticles into cell by active (receptor-mediated) or passive transport across the cell membrane [61].	12
Figure 2.7 Clathrin- and -caveolae-mediated internalization pathways [60]. MVBs = multivesicular bodies.	14
Figure 2.8 The endocytotic pathways in a mammalian cell [69].	15
Figure 2.9 Passive internalization of nanoparticles through lipid bilayer membrane [58].	16
Figure 2.10 Intercellular uptake and intracellular trafficking of nanoparticles.	18
Figure 2.11 Schematic illustration of the cellular barriers faced by bioactive molecules such as drugs or therapeutic DNA en route to the nucleus [80].	19

Figure 2.12 Schematic illustration of characteristics of carriers on cellular uptake efficacy [69].....	20
Figure 2.13 CLFM images of cellular uptake of NaYF_4 nanoparticles having various morphologies, hexagonal prism (1), sphere (2) and elongated sphere (3), against A375 cells (a). Quantitative analysis of the cellular uptake using flow cytometry by measuring the fluorescent intensity of the A-375 cells [83].	21
Figure 2.14 AFM images of particle associated with lipid bilayer. (left) lipid bilayer formation over a substrate with 5-20 nm silica nanoparticles (a-d) and (right) lipid bilayer formation over a substrate with mixed 5-140 nm silica particles (e-h). The formation of membrane occurs orderly from a-d (for left side) and e-h (for the right side) [56].	22
Figure 2.15 Schematic illustration size-dependence of particles association with lipid bilayer membrane having different fluidity [84].	23
Figure 2.16 Confocal microscopy images of the adhesion of positively charged polystyrene nanoparticles on giant unilamellar liposome. (a) 0min, without particle, (b) 50 min (c) 100 min, (d) 140 min. (left to right) Merged fluorescence images, dye-labeled lipids (red), nanoparticles (green), and encapsulated rh-dex (orange) [85].	24
Figure 2.17 Molecular models of various types of hybridized carbon nanostructures with different dimensionalities, 0D, 1D, 2D, and 3D [97].....	26
Figure 2.18 Schematic representation of paclitaxel conjugation to SWNT functionalized by phospholipids with branched PEG chains [103].	27
Figure 2.19 Schematic illustration of the covalent functionalization of CNTs with PEI (left) and non-covalent functionalization of CNTs with cetylpyridinium [104].	28
Figure 2.20 Schematic demonstration of PEGylated nanographene oxide for targeted drug delivery [33].	29
Figure 2.21 Schematic demonstration of Ce6 loaded on GO-PEG [107].....	30
Figure 3.1 Synthesis of mPEO-COOH.	34

Figure 3.2 Synthesis of mPEO-grafted oxidized carbon materials.	35
Figure 4.1 SEM (top) and TEM (bottom) photographs of (a) OCSs, (b) OCTs and (c) OGShs.	43
Figure 4.2 ATR-FTIR spectra of Graphite, SWCNTs, OCSs, OCTs and OGShs.	44
Figure 4.3 C 1s and O 1s XPS spectra of graphite, SWCNTs, OCSs, OCTs and OGShs.	45
Figure 4.4 Raman spectra of OCSs, OCTs and OGShs.	46
Figure 4.5 X-ray diffraction patterns of Graphite, OCSs, SWCNTs and OCTs.	47
Figure 4.6 Appearance of OCSs dispersibility in various solvents.	49
Figure 4.7 Hydrodynamic size distributions of an aqueous suspension of OCSs obtained at various post sonication times.	50
Figure 4.8 ^1H NMR spectrum of mPEO-COOH.	51
Figure 4.9 ATR-FTIR spectra of OCSs and mPEO-OCSs.	52
Figure 4.10 Association of OCSs _{Flu} (top), OCTs _{Flu} (middle) and OGShs _{Flu} (bottom) with Ld liposomes at 30 min after mixing. The graphs shown on the left represent fluorescence intensity along the white dash line of each corresponding image obtained from ImageJ software.	54
Figure 4.11 Schematic illustration of membrane association of OCS, OCT and OGSh.	54
Figure 4.12 Anthocyanin leakage from the anthocyanin-filled liposome without (top) and with (bottom) OCSs at various incubation times, <i>i.e.</i> , 0, 30, 60 and 120 min.	55
Figure 4.13 Association of OCSs _{Flu} (a and b) and mPEO-OCSs _{Flu} (c and d) with Ld (a and c) and Lo (b and d) membranes after the incubation time of 30 min. Plots showing fluorescence intensity (F.I.) along the white dotted line of each image are shown next to the images.	57

- Figure 4.14** Association of OCS_{S_{Rho}} with BODIPY-labeled Ld liposome (bottom) compared to BODIPY-labeled Ld liposome without OCS_{S_{Rho}} (top) at the incubation time of 30 min. (a) BODIPY-labeled Ld liposome, (b) OCS_{S_{Rho}} and (c) DIC images..... 58
- Figure 4.15** Association of OCS_{S_{Rho}} with Ld as a function of incubation time. The graphs below each corresponding image represent quantitative fluorescence intensity along the white dash line. Scale bars = 10 μ m..... 59
- Figure 4.16** Fluorescence intensity of OCS_{Rho} outside, inside the first and second layer of liposome as a function of incubation time. Scale bars = 10 μ m..... 60
- Figure 4.17** Association of OCS_{S_{Rho}} and DOPC-loaded OCS_{S_{Rho}} on the Ld membrane. The images were obtained with fluorescence mode (top) and DIC mode (bottom). . 61
- Figure 4.18** Interaction of OCS_{S_{Rho}} (150 ppm) and curcumin-loaded OCS_{S_{Rho}} (75 ppm curcumin, 150 ppm OCS_{S_{Rho}}) with cell-sized liposomes (0.1 mM of the DOPC). Fluorescence images of the Ld liposomes after 30 min incubation with OCS_{S_{Rho}} (row 1) and curcumin-loaded OCS_{S_{Rho}} (row 2): shown as the merged images of both curcumin fluorescence and OCS_{S_{Rho}} fluorescence (column a), only curcumin signal (green, column b), and OCS_{S_{Rho}} signal (red, column c)..... 62
- Figure 4.19** Amount of un-adsorbed DMPE-RhB as a function of filtration time at pH 7.4 (red) and 5.5 (blue) compared with control (no OCSs, black). 63
- Figure 4.20** Cytotoxicity of (column a): OCS (blue), OCT (red) and OGSh (green) and (column b): mPEO-OCS (blue), mPEO-OCT (red) and mPEO-OGSh (green) against A459 and A549RT-eto cell lines at the incubation time of 72 h..... 64
- Figure 4.21** Delivery of curcumin into A549 cells by rhodamine-labeled oxidized carbon materials: control cells (row 1), cells incubated with curcumin-loaded OCS_{S_{Rho}} (row 2), curcumin-loaded OCT_{S_{Rho}} (row 3), curcumin-loaded OGSh_{S_{Rho}} (row 4), curcumin-loaded mPEO-OCS_{S_{Rho}} (row 5), curcumin-loaded mPEO-OCT_{S_{Rho}} (row 6), curcumin-loaded mPEO-OGSh_{S_{Rho}} (row 7). Column a shows image in DIC mode, Column b-d represents the fluorescence mode showing the fluorescence signals from nucleus staining with Hoechst (blue, b), curcumin (green, c) and rhodamine-

labeled oxidized carbon materials (red, d). The concentration of oxidized carbon materials was controlled at 10 $\mu\text{g}/\text{mL}$ with the incubation time of 4 h. 66

Figure 4.22 Anti-cancer activity against A549 (top) and A549RT-eto (bottom) cell lines of OCSs, PTX, PTX-loaded OCSs, DOX and DOX-loaded OCSs with various concentrations. Incubation time was 72 h. Statistical significant difference was calculated using one-way ANOVA (* $p < 0.01$)..... 68

Figure A1 Hydrodynamic size distributions of an aqueous suspension of OCSs obtained at various times post sonication..... 82



CHAPTER I

INTRODUCTION

There are many diseases which cause the death of people in the world. The effective therapeutic method is needed to cure the patients and overcome this problem. Therefore, it becomes a critical scientific issue for both pharmaceutical and medical fields. Even though numerous high potential drugs and bioactive molecules such as proteins, peptides and nucleic acids, have been widely developed for therapeutic purposes, limited treatment efficiency is still observed [1,2]. One obstacle for the treatment efficiency problem is that the active molecules cannot get into the problematic cells and thus cannot perform their functions. In order to improve the therapeutic efficiency, many approaches have been intensively studied [3-7]. Among them, drug delivery system is an outstanding candidate since it has ability to increase bioactivity of the drug, prolong life time of the drug in circular system, and in some cases can help targeting the active molecules to the required sites [8-14]. In facts, new strategies for fabricating of targeted-drug delivery systems in the past decades have brought us to a more precise and effective treatment [15-20].

Recently, various types of drug delivery carriers, *i.e.*, liposomes, polymeric micelle, polymeric particles, inorganic particles and viral vector, have been fabricated [21-28]. The major function of these carriers is to enhance the delivery efficiency of drug molecules. Other advantages such as controlled release, increase of drug loading efficiency, reduction of drug dose, prolongation of drug life time in circulation system and organelle targeting are also considered. A carrier with multi-responsiveness such as thermoresponsive, pH sensitive and irradiation triggering, have attracted more attention to improve the treatment efficiency [29-31].

Carbon materials, *i.e.*, graphene oxide and carbon nanotubes, have become the candidates of drug carriers because of their versatile properties such as various morphologies, large surface area, water dispersibility, easy surface modifications, good stability and good biocompatibility [32-36]. Among various carbon materials, one type of carbon particulates was serendipitously found during the oxidation of graphite. This

particle is called cluster of carbon nanospheres [37]. It shows an ability to deliver cargoes into mammalian cells and enhances cellular uptake ability of the cargo. Furthermore, the cluster of carbon nanospheres possess endosomal escape, making them remarkable for biomedical applications such as gene therapy.

Even though several morphologies of carbon materials have been widely used as drug carrier, comparison of the cellular uptake and delivery efficiency between various shapes of the carbon materials have not been studied yet. Consequently, this research is focused on the ability of the three shapes of oxidized carbon materials, oxidized carbon nanospheres (OCSs), oxidized carbon nanotubes (OCTs) and oxidized graphene sheets (OGShs), to deliver curcumin into mammalian cells. In addition, the interaction of the carbon particulates with lipid bilayer membrane is intensively studied.



CHAPTER II

LITERATURE REVIEWS

2.1 Administration Routes

In order to deliver matter into cells, administration route is one of important factors which decide treatment efficiency. However, the appropriate administration route depends on the properties of the drug and also type of the disease.

2.1.1 Oral

The oral administration route is the most common and convenient way to deliver drug into the body, because this route does not cause pain to the patient and need no specific tools. The drug is uptaken via mouth and then, transferred to gastrointestinal tract (GI tract) for further absorption. Nevertheless, this route is not appropriate for some kinds of drug such as protein, peptides and nucleic acids since they are poorly absorbed and they have to go through the digestion parts, which leads to the degradation [10,38].

2.1.2 Inhalation

Inhalation is a needle-free method. The drug is uptaken into the body via the lungs. It is an effective administrative route for medication of the pulmonary disease because the drug can go directly to the respiratory system. Therefore, the drug can provide the rapid effect to the targeted area. Furthermore, it requires less dose of the drug, resulting in reduction of side effect [38,39].

2.1.3 Injection

In the case of the drugs which the oral route is not suitable, injection is the major alternative delivery method. However, it possesses various limitations such as pain, burst drug release, needle phobia, specific tool and risk of infections. For some chronic diseases such as insulin-dependent diabetes, which repeated administration is needed, these problems become more severe. To overcome these limitations, new technologies have been fabricated. Among them, drug carrier with controlled release

character is one of the candidates because the carrier decreases drug dose and prolongs the drug life time by control drug release. Therefore, the frequency of injection can be reduced [40].

2.1.4 Transdermal

Since the delivery via oral and injection possess some problems, alternative route by delivering drugs across the skin becomes more attractive. This method has some advantages such as less side effects, pain and degradation of drug in the digestion system. Nevertheless, it possesses some limitation because of the nature of the skin, which behaves as a barrier to prevent the penetration of guest substances. Therefore, various technologies, *i.e.*, electroporation, ionophoresis, sonophoresis, jet injection, laser irradiation, and microneedles have been developed to improve the penetration. However, this method requires specific tools. Therefore, it is presumably not convenient for some treatment. On the contrary, development of drug carriers, which possess ability to penetrate across skin overcomes the drawback and makes this method more suitable for various treatments [41].

2.2 Carrier Types

In the past decade, technologies to fabricate the carrier for delivery drug into cells have been widely studied. For the effective delivery, types of the carrier have to be considered.

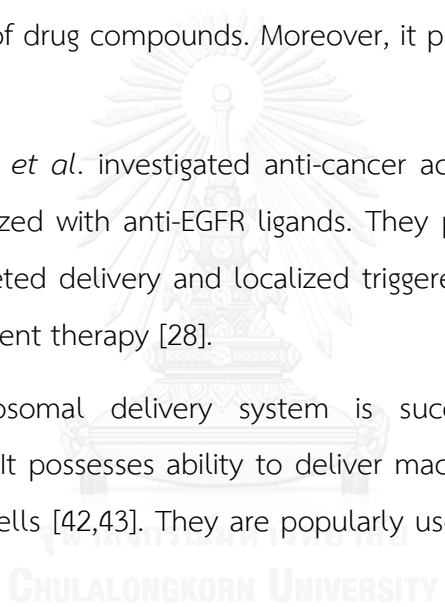
2.2.1 Liposomes

Liposome mostly composes of phospholipids self-assembling in water to form vesicle having bilayer structure. Its structure is similar to cell membrane. Therefore, liposome can be used to mimic the real cell membrane. Beside this function, liposome has been used as drug carrier. It is able to deliver both hydrophobic and hydrophilic drugs into cells by either fusion with cell membrane or diffusion through the lipid bilayer of cell membrane [22]. However, delivery of liposomes is limited due to uncontrolled release and unstability *in vivo* in humans because the classical liposomes are rapidly eliminated from blood circulation system. Many attempts have been

established to improve the efficiency of liposomal delivery. In 2013, An *et al.* studied controlled release of drug loaded into thermosensitive liposomes with embedded gold nanoparticles (AuNPs) in the lipid bilayer. The thermosensitive liposomes were designed to release the loaded drug at the temperature beyond the lower critical solution temperature (LCST). Since the AuNPs can absorb UV and convert into heat, irradiation by near-IR can induce phase transition and drug release [21].

In 2015, Cosco *et al.* fabricated resveratrol- and 5-fluorouracil-loaded ultradeformable liposomes for treatment of non-melanoma skin cancer via transdermal route. They found that the ultradeformable liposome is able to increase the skin permeation of drug compounds. Moreover, it provided controlled release of the drugs [24].

In 2016, Haeri *et al.* investigated anti-cancer activity of the thermosensitive liposomes functionalized with anti-EGFR ligands. They proposed that the fabricated liposomes show targeted delivery and localized triggered release of the anti-cancer drug, resulting in efficient therapy [28].

Recently, liposomal delivery system is successfully industrialized and commercialized [42]. It possesses ability to deliver macromolecules such as nucleic acid and siRNA into cells [42,43]. They are popularly used for both investigation and therapeutic purposes. 

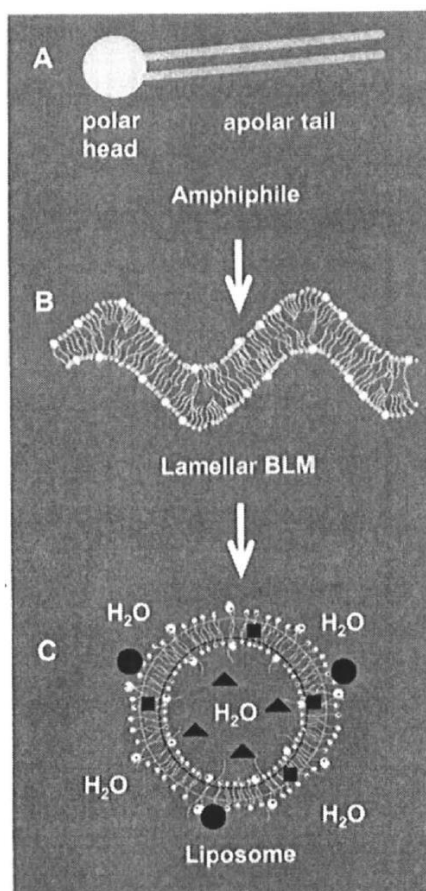


Figure 2.1 Amphiphilic monomers and polymers self-aggregate in water form lamellar bilayer lipid membranes (BLM), reducing the interphase lipophilic hydrocarbon tails and water. (B) BLM rearrange to spherical liposomes either spontaneously or assisted (i.e.t by shear or ultrasonication) further reduce the tail/water interphase [8].

2.2.2 Polymeric Micelles

Polymeric micelle is a core–corona structure forming from self-assembly of amphiphilic polymers, which are several hundred block copolymers containing hydrophilic and hydrophobic moieties, in water. It is one of the important classes of drug carriers. The self-assembly process of amphiphilic molecules into polymeric micelles usually occurs when concentration of the amphiphilic molecules is higher than a critical micelle concentration (CMC) [44]. Since the polymeric micelles usually possess the hydrophobic interior with hydrophilic corona, they can be loaded with

hydrophobic drugs. Therefore, this carrier is able to overcome the limitation of the aqueous insoluble drugs. Moreover, the hydrophilic corona can exhibit stealth behavior, depending on type of polymer, which prevents the recognition by the immune system and thus prolongs the circulation time of the drug in the blood circulation system. In addition, the polymeric corona can be modified by targeting molecules to enhance the precise accumulation in the targeted organelles [26,45,46].

In 2006, Nasongkla *et al.* synthesized diblock copolymer of maleimide-terminated poly(ethylene glycol) and poly(D,L-lactide) (MAL-PEG-PLA) and used for the preparation of multifunctional polymeric micelles containing superparamagnetic iron nanoparticles for MRI application, c(RGDf(ε-S-acetylthioacetyl)K as targeting ligand and doxorubicin as chemotherapeutic agent. The tumor treatment experiment in vivo indicated that the multifunctional polymeric micelles possessed specific targeting to the $\alpha_v\beta_3$ -integrin receptor with MRI contrast characteristics. Moreover, controlled release of doxorubicin from this carrier could be achieved [29].

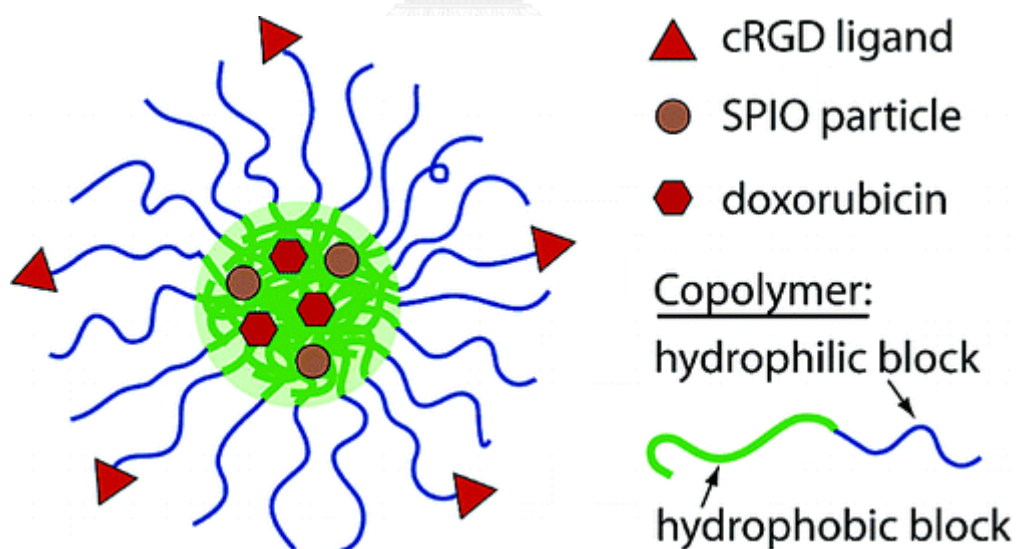


Figure 2.2 Multifunctional polymeric micelles containing super paramagnetic particles, anti-cancer drug and targeting ligand for targeted drug delivery [29].

In 2015, Gupta *et al.* compared therapeutic efficiency between polymeric micelle prepared block copolymers of poly(ethylene oxide)-co-poly(D,L-Lactide) (PEG-PDLA) and nanoemulsion of perfluorocarbon with the presence of polymeric micelles. Paclitaxel was used as a chemotherapeutic agent. They found that the nanoemulsion stabilized with polymeric micelles exhibit low hematological toxicity with high efficacy of tumor treatment compared with the corresponding micelles. making them become more preferable as drug carrier [44].

2.2.3 Polymeric Nanoparticles

The other type of drug carriers, which is similar to the polymeric micelles, is polymeric nanoparticles. The polymeric nanoparticles are particulate dispersions forming from entangled polymeric matrix with the size range from 10-1000nm. This types of carrier possesses a matrix-like structure of amphiphilic copolymers. Either drugs or active compounds can be entrapped into the matrix [23,47,48].

In 2010, Zhou *et al.* synthesized chitosan derivatives with amphiphilic structure by grafting hydrophobic moieties, deoxycholic acid (DCA), and hydrophilic moieties, glycidol onto the chitosan backbone and found that the copolymers could self-assemble in water and form into polymeric nanoparticles with the size ranging from 160 to 210 nm. Then, they investigated the anti-tumor ability of the nanoparticles toward MCF-7 cells using doxorubicin as an anti-cancer drug. The result suggested that doxorubicin-loaded nanoparticles could be uptaken into MCF-7 cells with the controlled release of doxorubicin [49].

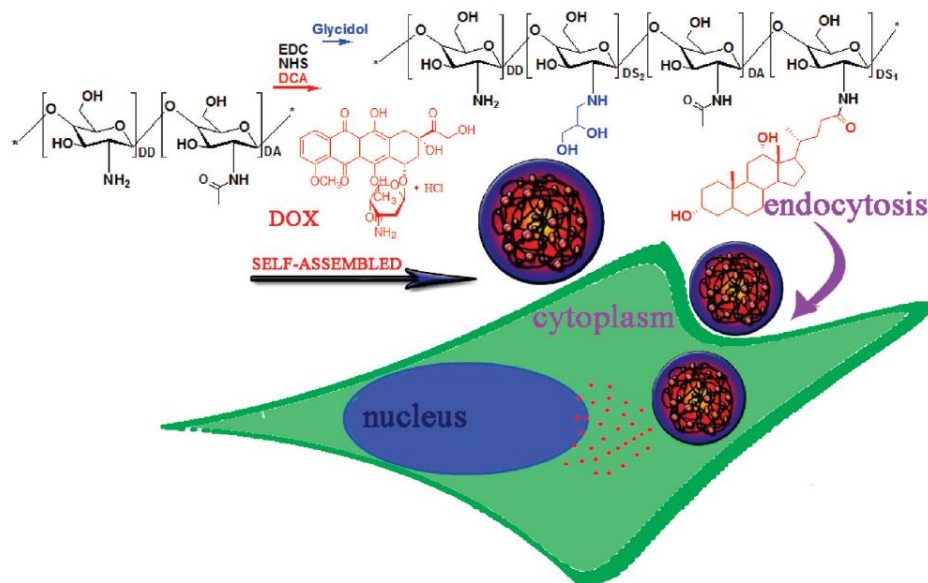


Figure 2.3 Synthesis of glycidol-ctiosan-deoxycholic (G-CS-DCA) acid and encapsulation of doxorubicin into G-CS-DCA nanoparticles for delivery into cells [49].

In 2011, Wang *et al.* fabricated redox-responsive nanoparticles from the single disulfide bond-bridged block copolymer of poly(ϵ -caprolactone) and poly(ethylethylene phosphate) (PCL-SS-PEEP) and used for delivering of doxorubicin into multidrug resistance (MDR) cancer cells, MCF-7. They found that the carrier enhanced the accumulation of doxorubicin in the cancer cells and also increased retention time in MDR cells. In addition, rapid release of doxorubicin in the cells could be achieved by the reductive condition in the cells [50].

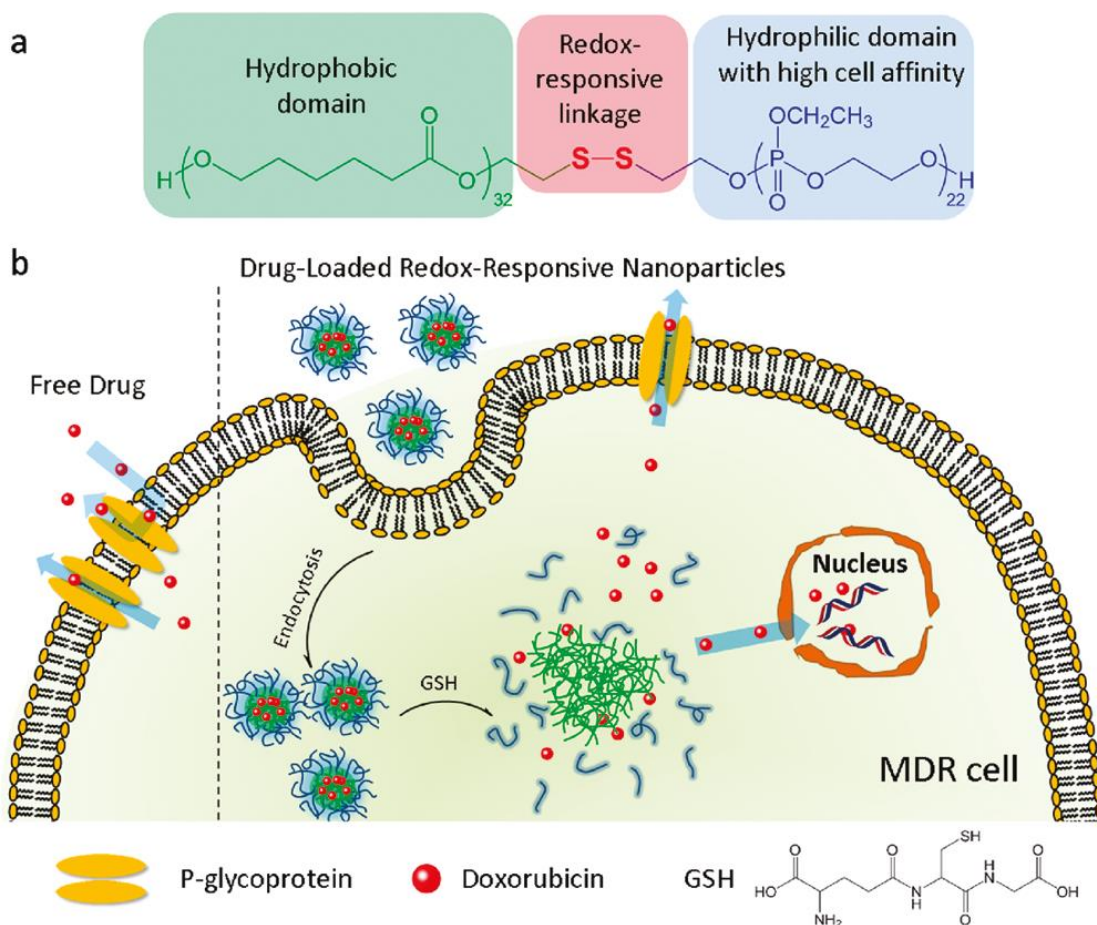


Figure 2.4 Schematic illustration of (a) chemical structure of disulfide-bridged PCL-SS-PEEP block copolymer and (b) redox-responsive nanoparticles for overcoming multidrug resistance of cancer cells [50].

2.2.4 Inorganic Nano- or Microparticles

Inorganic nanoparticles such as metal, silica or superparamagnetic particles are also widely used as drug carriers owing to their unique properties such as size-dependent physical and chemical properties, magnetic characteristic and semiconductor property.

In 2012, Nasrolahi Shirazi *et al.* investigated cellular uptake of cyclic peptide-capped gold nanoparticles (CPAuNPs) into human ovarian adenocarcinoma (SK-OV-3)

cells. In addition, they reported that CPAuNPS could more effectively drugs into cells compared to the uptake of the pure drug [51].

In 2013, Han et al. prepared highly uniform α -NaYF₄:Yb/Er hollow microspheres and used to encapsulated doxorubicin hydrochloride (DOX). The obtained microspheres exhibit pH-dependent controlled release of DOX in vitro [52].

2.2.5 Viral Delivery

Beside the non-viral carriers, which are reviewed above, a delivery system using virus has also attracted more attention. Drug delivery by viral vector has been intensively studied these days since the viruses possess highly efficient structures and mechanisms to infect in cells with the good targeting with specific types of cells. Therefore, viral vectors can be used as vehicles for gene delivery [3,53,54].

In 2006, Everts *et al.* reported use of adenovirus as a vector to deliver gold nanoparticles. The adenoviral vector was covalently linked with gold nanoparticles and infected into Hela cells. The carrier showed targeted delivery together with an amplifying nanoparticle payload [55].

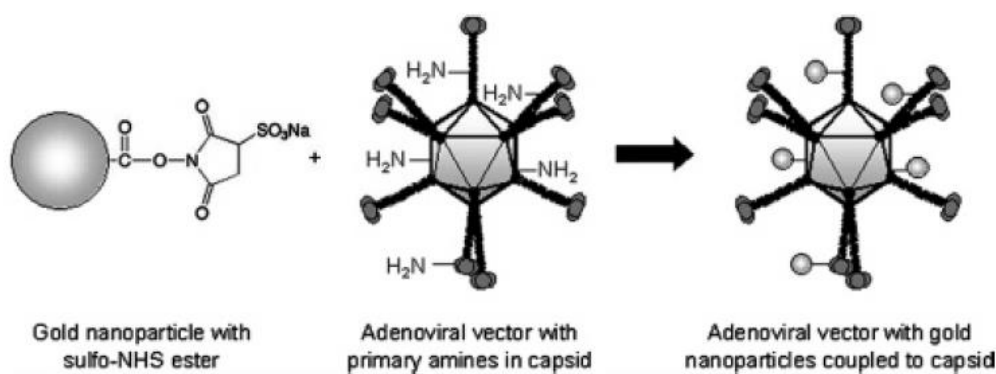


Figure 2.5 Covalently coupling of gold nanoparticles the adenovirus through an amide bond formation [55].

2.3 Cellular Uptake

In order to deliver the matter into cells, the first barrier of the cell that the matter has to cross is plasma membrane. The plasma membrane, so called cell membrane, primary consists of bilayer structure of lipid molecules and embedded proteins. Major type of the lipid of the plasma membrane is phospholipid, which composes of hydrophilic phosphate group and hydrophobic tail of fatty acid chains. The cell cytoplasm is surrounded by the plasma membrane in order to protect and separate cell organelles from the outside environment. The membrane, moreover, serves as selective barriers for transportation of the matters between inside and outside of the cell, which means it allows some molecules to diffuse across the membrane, whereas some molecules are not allowed [56-58]. There are several pathway for the cell to uptake the matter. Generally, the uptake mechanism can be divided into two major groups; active and passive internalization [59,60].

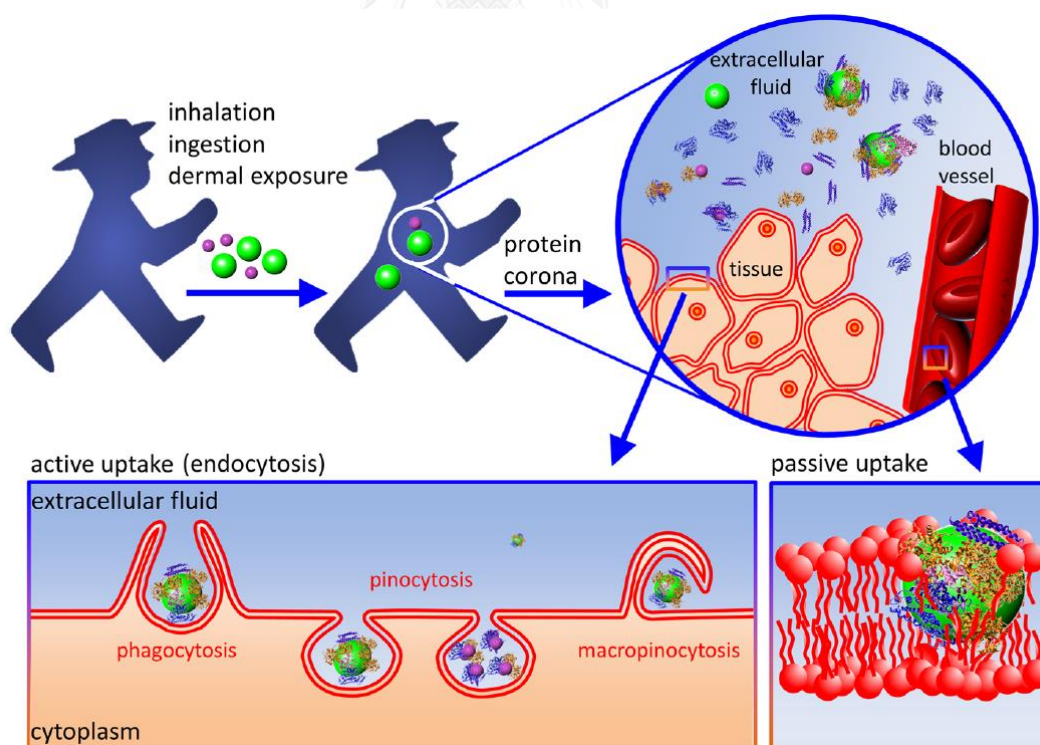


Figure 2.6 Cellular uptake of nanoparticles into cell by active (receptor-mediated) or passive transport across the cell membrane [61].

2.3.1 Active Uptake (Endocytosis)

Endocytosis is one of the mechanisms that cells uptake guest molecules. The endocytic pathway can be categorized into two subgroups: clathrin-mediated endocytosis (CME) and caveolae-mediated endocytosis [62].

Clathrin-Mediated Endocytosis (CME)

This pathway is receptor-mediated endocytosis and is the main mechanism for the uptaking in most cell types. Through this pathway, matters are uptaken into cells by binding with surface receptors. Upon contact with the cell membrane, the guest molecules are recognized by protein complexes, which allows polymerization of clathrin, leading to the formation of a clathrin-coated pit. These pits will form into the endocytic vesicles. The vesicles are then uncoated prior to fusing with early endosomes. The endosomes vesicle is transported into the cytosol of the cell, before being fused with lysosomes. Then, the cargoes are either being destroyed by lysosomes or released into the cytosol [60,63].

Caveolae-Mediated Endocytosis

Caveolae-mediated endocytic pathway is a clathrin-independent uptake mechanism. The caveolae are characteristic flask-shaped protein that typically exist around cell membrane invaginations, of which the size is around 50–80 nm,, and move into lipid raft fractions, which are cholesterol and sphingolipids-enriched and high dynamicity membrane fractions. Caveolae consists of a 21kDa coated protein called caveolin-1 (or caveolin-3 in muscle cells). During the caveolae-mediated internalization, caveolin-1 moves into the cytoplasm along with the vesicles. Then, the cargoes are translocated into cytosol [64-66].

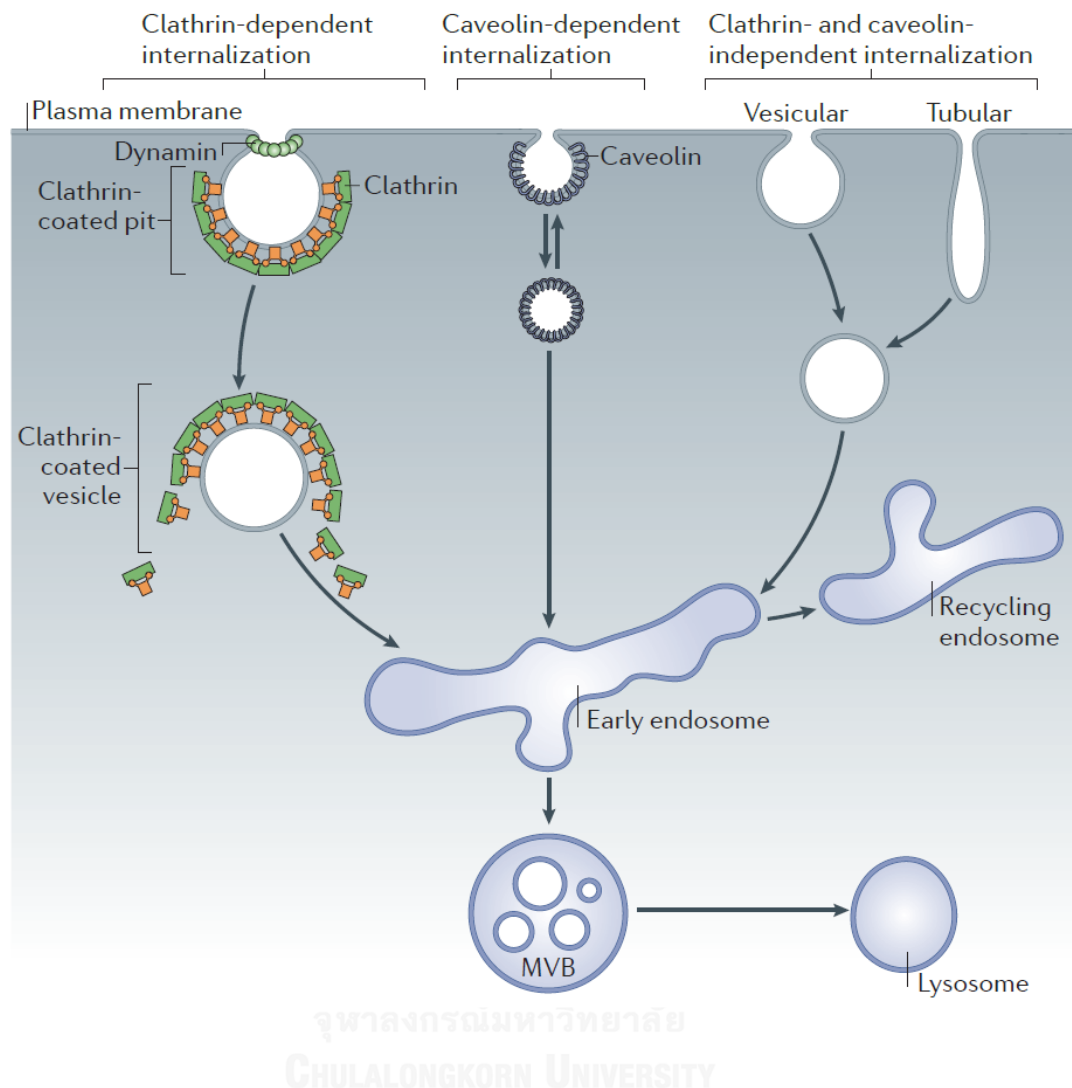


Figure 2.7 Clathrin- and -caveolae-mediated internalization pathways [60]. MVBs = multivesicular bodies.

Phagocytosis

Phagocytosis is one of endocytic pathways. It is different from the other endocytosis mechanisms because it is a special uptake phenomenon for specific cell types such as macrophage. The phagocytosis occurs by the binding of guest molecules with membrane receptor surface, followed by drawing of cell membrane like a cup-shaped invagination and engulfment the matter inward the cell. The engulfed membrane vesicle becomes the phagosome. The phagosome then matures by fusion

with the endosomes and lysosomes, resulting in the digestion of the matter. This process is a main mechanism used to destroy or remove pathogens and death cells and it often takes place in an organism's immune system [59,62].

Macropinocytosis

Macropinocytosis is an endocytic pathway, which is similar to phagocytosis. During the internalization process of micropinocytosis, cell membrane generates vesicles through membrane ruffling, of which the size is heterogeneous. This process occurs owing to actin polymerization. Since the vesicle size of macropinocytosis is larger than those of the other endocytic pathways, it is a highly effective pathway for non-selective endocytosis of macromolecules. Therefore, it has attracted more attention as an important route for drug delivery because several types of cell-penetrating peptides internalize into the cell through this pathway [67,68].

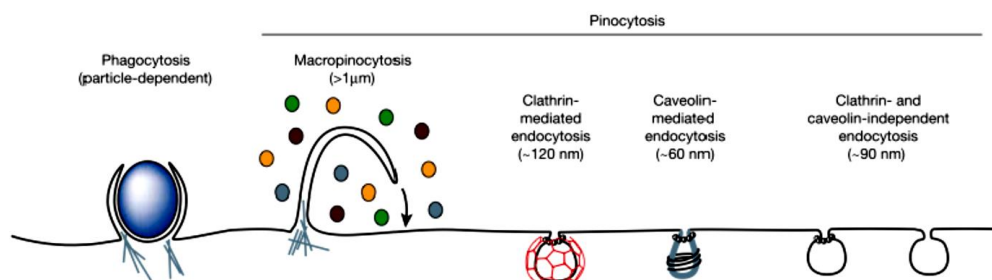


Figure 2.8 The endocytotic pathways in a mammalian cell [69].

2.3.2 Passive Uptake (Non-endocytic Delivery)

Even though the endocytosis pathway can effectively internalize macromolecules into mammalian cells, it lacks an ability to transport the matter to the targeted site such as nucleus because the matter will be entrapped by the endosome and finally, digested by lysosome. In order to overcome this drawback, transportation of the cargoes that can avoid the endocytic route has to be considered.

From drug delivery points of view, use of the carriers which avoids endosomal entrapment or have ability to escape from the endosome to the cytosol have become more attractive. Typically, small guest molecules are able to pass through lipid bilayer membrane of the cell via passive diffusion driven by a concentration gradient. In the case of molecules having the size larger than 40–45 kDa, they, nevertheless, require specific targeting signals to cross the membrane. This phenomenon also occurs at the nuclear membrane, which separates cytosol from nucleus [58,69,70].

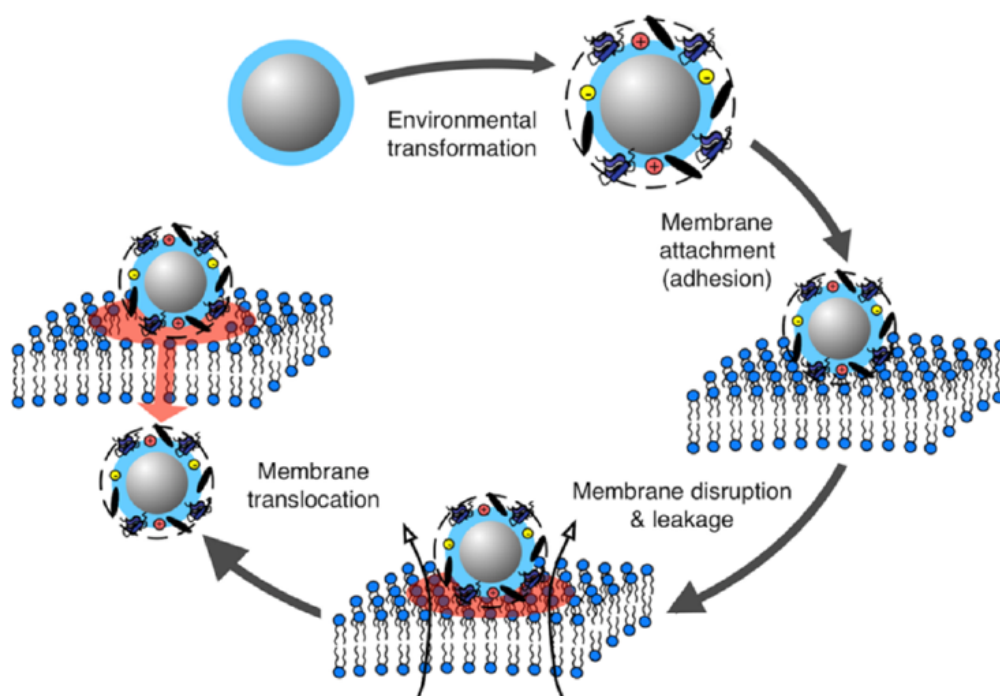


Figure 2.9 Passive internalization of nanoparticles through lipid bilayer membrane [58].

2.3.3 Endosomal Escape

As mentioned previously, ability of nanoparticles to avoid the endosome internalization and degradation by lysosome entrapment are required for efficient delivery of cargoes to targeted organelles. This behavior is popularly called endosomal escape, which refers to the release of cargoes from endosome before the fusion process of the endosome and lysosome. Researches have demonstrated that the endosomal escape can be induced various means such as by pore formation in the

endosomal membrane [71], pH-buffering effect (“proton sponge” effect) [72], a fusogenic mechanism [73,74], or a photochemical disruption of the endosome membrane [75]. Various kinds of cationic polymers, such as poly(ethylenimine), poly(amidoamine), propylacrylic acid and poly(L-Lysine), exhibit endosomal escape induction property through the proton sponge mechanism, which is a result of an osmotic effect. The chemical process involves that the materials containing uncharged amines absorb the protons, resulting in an inhibition of endosomal acidification; an existence of excess protons allows an influx of counter ions into endosomes, leading to an increase of osmotic pressure and thus, rupture of the endosome membrane [76,77]. The endosomal escape can be achieved using fusogenic peptides which are short sequences of amino acids that can insert in to lipid membrane and destabilize the lipid bilayer by the formation of highly bent lipid segments. The mechanism of the destabilization of the endosomal membrane is because this peptide changes the conformation upon pH trigger in endosome. Therefore, it is able to insert into endosomal membrane and thus, fuse with the membrane, leading to the endosomal escape [74].

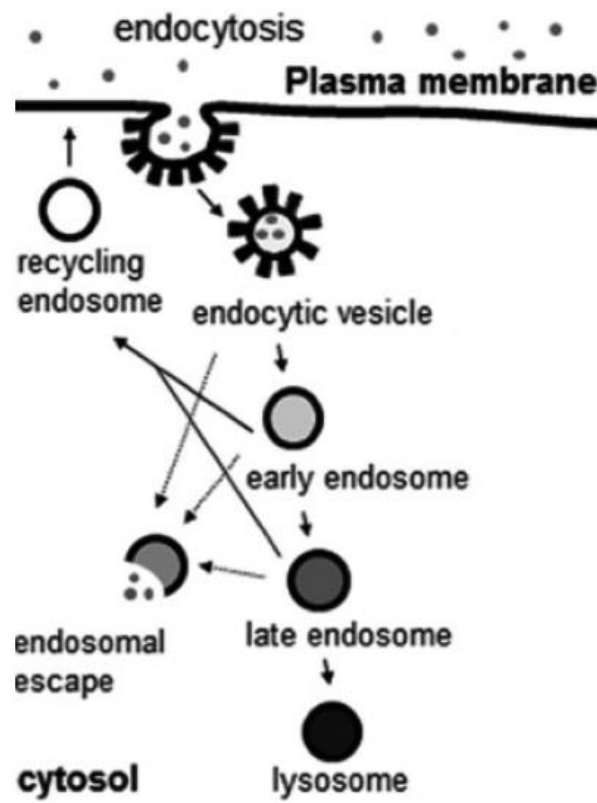


Figure 2.10 Intercellular uptake and intracellular trafficking of nanoparticles.

2.3.4 Delivery to Nucleus

Targeted sites of many therapeutic methods are in nucleus, especially for gene therapy and some chemotherapy. In the case of molecules smaller than 40–45 kDa, the passive diffusion through nuclear pore complexes can take place. In addition, carrier with the size smaller than 10 nm can cross the cell nucleus without targeting sequences. On the contrary, larger molecules have to be targeted with some specific signals such as the nuclear localization sequence (NLS) in order to pass through the nuclear membrane [69,78-80].

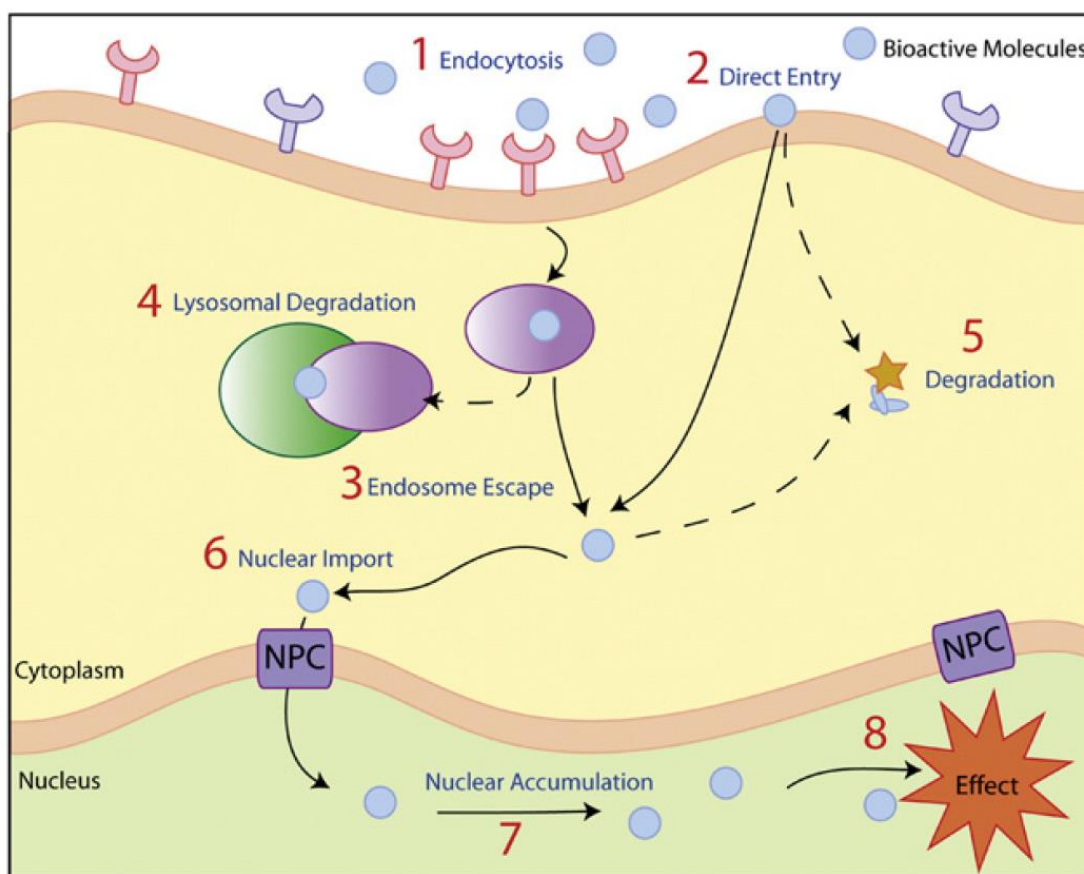


Figure 2.11 Schematic illustration of the cellular barriers faced by bioactive molecules such as drugs or therapeutic DNA en route to the nucleus [80].

CHULALONGKORN UNIVERSITY

2.4 Carriers and Uptake Ability

Uptake ability plays an important role for drug delivery system because it decides cytotoxicity against the cells and capability for treatment of the diseases. The most important organelle of cell for uptake procedure is cell plasma membrane, which composes of lipid bilayer structure, because it is the frontier barrier of cell that contacts with surrounding environment and other matters. Generally, transportation of ions and proteins with size in nanometers across the membrane occurs through specific membrane-transportation protein channels. While, the other macromolecules are uptaken into cell via endocytosis upon contact of the guess molecules with the cell membrane [56,81]. There are many factors for particulate materials to be uptaken into

cytosol or nucleus of mammalian cells through the plasma membrane, e.g., size, hydrophobicity/hydrophilicity, surface charge and in particular, shape of the materials [81].

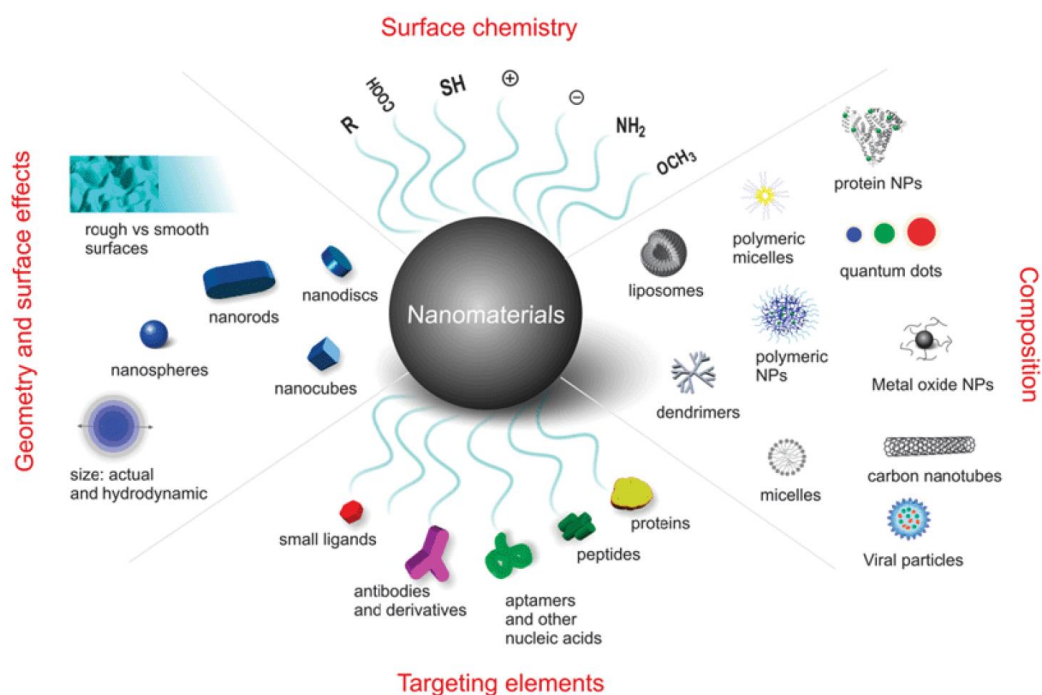


Figure 2.12 Schematic illustration of characteristics of carriers on cellular uptake efficacy [69].

2.4.1 Shape

In the past decade, many researches have revealed that the interaction of cell membrane is significantly affected by shape. In 2012, Shimoni *et al.* studied the cellular uptake of poly(methacrylic acid) hydrogel capsules preparing on spherical and rodlike silica template against Hela cells. The results indicated that the cellular internalization rate of the capsules greatly depended on their aspect ratio. The spherical one showed high internalization rate as compared to the other capsules having higher aspect ratio [82].

In 2015, Tree-Udom *et al.* prepared lanthanide-doped NaYF₄ nanoparticles with three different morphologies, sphere, elongated sphere and hexagonal prism, and evaluated the effect of shape on lipid bilayer membrane association as well as intracellular uptake. They found that the NaYF₄ nanoparticles with elongated spherical morphology exhibits high cellular internalization as compared to the other shapes. This result also agrees well with the interaction of the nanoparticles with lipid bilayer membrane [83].

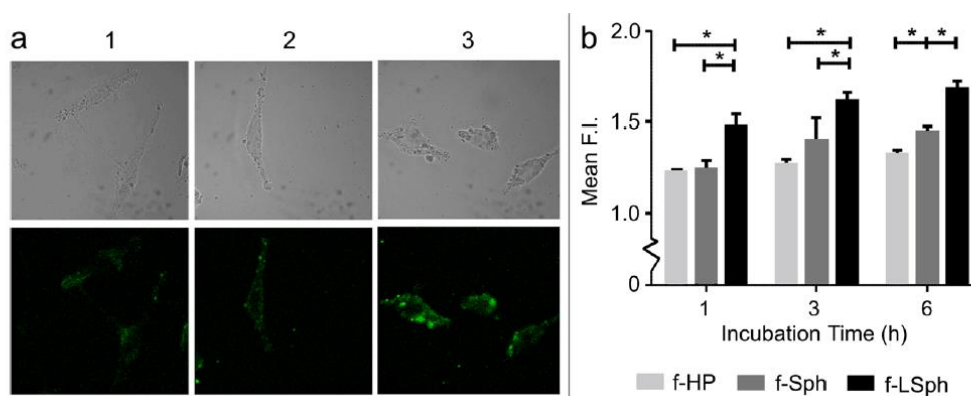


Figure 2.13 CLFM images of cellular uptake of NaYF₄ nanoparticles having various morphologies, hexagonal prism (1), sphere (2) and elongated sphere (3), against A375 cells (a). Quantitative analysis of the cellular uptake using flow cytometry by measuring the fluorescent intensity of the A-375 cells [83].

2.4.2 Size

Apart from shape, size of carrier also has strong influence on cellular uptake. As reported by Roiter in 2008, they studied the formation of lipid membrane prepared from L-R-dimyristoyl phosphatidylcholine (DMPC) over a substrate having silica nanoparticles with several radii using atomic force microscopy. They concluded that particles with radii range from 1.2 to 22 nm were not covered by the bilayer membrane, while the particles with radii other from this range were covered by the bilayer membrane, during the membrane formation on the substrate. This result indicates that

size of particle strongly has influence on the membrane curvature and also interaction between particle and membrane [56].

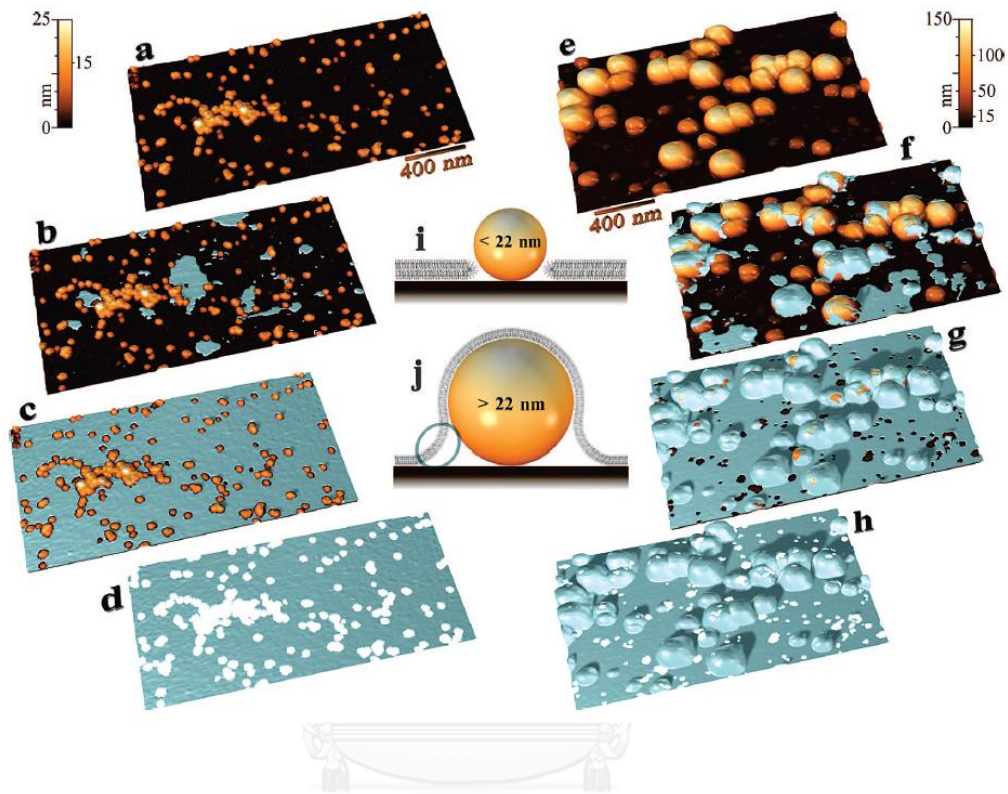


Figure 2.14 AFM images of particle associated with lipid bilayer. (left) lipid bilayer formation over a substrate with 5-20 nm silica nanoparticles (a-d) and (right) lipid bilayer formation over a substrate with mixed 5-140 nm silica particles (e-h). The formation of membrane occurs orderly from a-d (for left side) and e-h (for the right side) [56].

In 2012, Hamada *et al.* investigated the partitioning of nano/micro particles in heterogeneity membrane. Polystyrene particles having various sizes were used as a model and two types of lipid membrane with high (Ld) and low (Lo) fluidity were prepared. They found that size of the particle intensely affected the selective association with lipid bilayer membrane. The particles with the size smaller than the threshold (200 nm) preferred the low fluidity membrane. On the contrary, the particles

having larger size than the threshold adhered on high fluidity membrane. This phenomenon can be described based on free energy of membrane curvature [84].

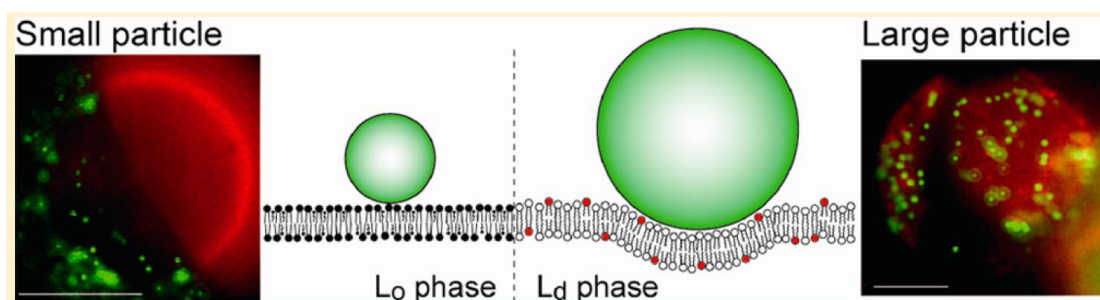


Figure 2.15 Schematic illustration size-dependence of particles association with lipid bilayer membrane having different fluidity [84].

2.4.3 Surface Charge

Since the lipid membrane consists of self-assembled lipid molecules, which the negatively hydrophilic heads locate at the outer membrane, surface charge of the particle coming into contact with the membrane surface is considered to be important. Generally, the membrane surface exhibits negative charge due to the phosphate groups of phospholipid molecules. Particles with the negative charge usually show electrostatic repulsion with the membrane surface. On the contrary, positively charged particles preferably bind with the lipid membrane. In addition, the positively charged particles can also cause embedding of the particle into the bilayer and membrane flipping by increase tilt angle of the membrane head groups, resulting in depolarization of the membrane [81].

In 2013, Li and Malmstadt studied interaction of positively charged nanoparticles with lipid membrane of the giant unilamellar liposomes. They reported that the cationic polystyrene nanoparticles with the size of 20 nm show strong adhesion on the membrane surface. In addition, the adhesion of this cationic nanoparticles induces membrane protrusions, leading to shrinkage of the liposomes.

They also proposed that the adhesion of cationic particles generates transient pore on the lipid bilayer membrane, which was proofed by leakage of a polymer with high molecular weight from the liposome vesicle [85].

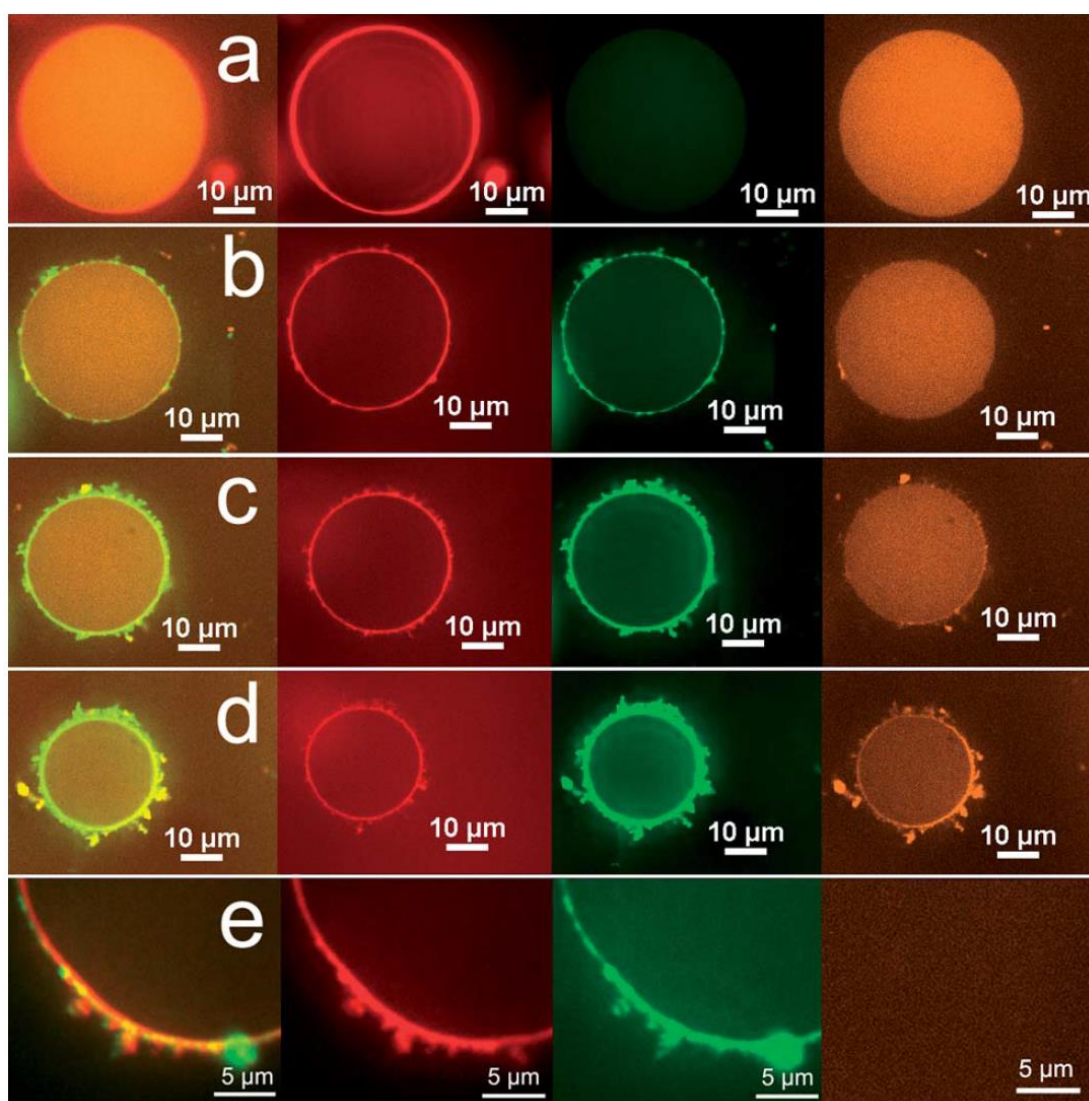


Figure 2.16 Confocal microscopy images of the adhesion of positively charged polystyrene nanoparticles on giant unilamellar liposome. (a) 0min, without particle, (b) 50 min (c) 100 min, (d) 140 min. (left to right) Merged fluorescence images, dye-labeled lipids (red), nanoparticles (green), and encapsulated rh-dex (orange) [85].

2.5 Cell-Size liposomes

As described previously, liposomes mostly consist of self-assembled phospholipid molecules, making them similar to the plasma membrane of living cells. Consequently, liposomes have been intensively studied and used as a simple model to mimic the cell membranes. Size of the cell-size liposomes varies from 50 nm to 10 μm or larger. Due to the limitation of the optical microscopy resolution, cell-sized liposomes should be $\sim 10 \mu\text{m}$ in diameter. On the other hand, the small-sized liposomes are not suitable for being studied because they are not so stable and usually exhibit aggregation or fusion, which is a result of high curvature [86,87].

2.6 Carbon Materials as Drug Carrier

At present, there are numerous shapes of carbon nanomaterials, some of which are in fascinating morphologies, with novel physical and chemical properties. Well-known examples are graphite, carbon nanotubes, fullerene, graphene and graphene oxide. They are used in various applications such as nanoelectronic devices, composite materials, solar cell, conducting polymers, supercapacitors and also nanomedicine. Thus far, many researchers have explored on the use of carbon nanomaterials, especially graphene oxide, in biomedical applications such as drug delivery, gene delivery, cellular imaging and cancer therapy. It has been shown that the material is non-toxic and possesses ease of performing chemical modification and high capability for molecular loading [88-96]. There are several types of well characterized carbon nanomaterials, *e.g.*, graphite, graphene, carbon nanotubes and fullerene and they are 3D, 2D 1D and 0D of sp^2 -hybridized carbon network structures [97]. Nevertheless, the most two widely uses for drug delivery application are carbon nanotubes and graphene oxide [88,98-102].

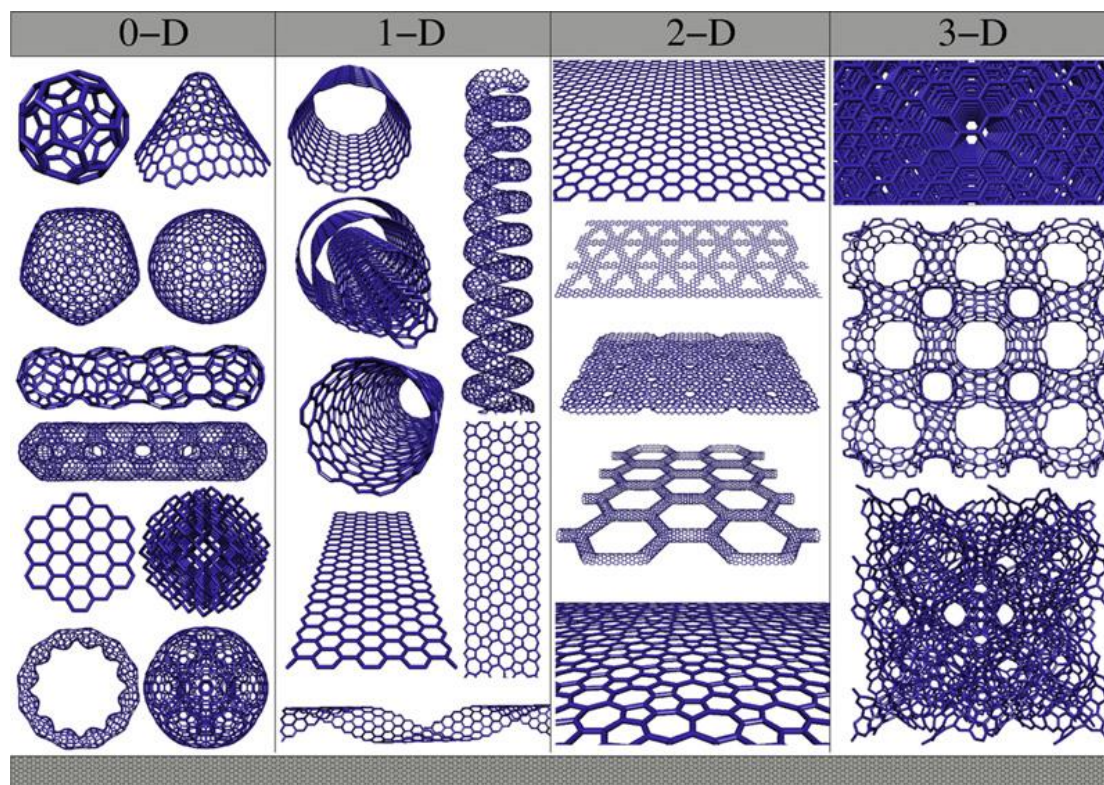


Figure 2.17 Molecular models of various types of hybridized carbon nanostructures with different dimensionalities, 0D, 1D, 2D, and 3D [97].

2.6.1 Carbon Nanotubes

Carbon nanotube is a main member of carbon materials. Pristine carbon nanotubes have highly hydrophobic surfaces, and are not soluble in aqueous solutions. Therefore, the carbon nanotubes have to be surface functionalized in order to improve water dispersibility so that they are applicable in biomedicines. Carbon nanotubes are widely used as drug carrier since they possess biocompatibility and low toxicity. Moreover, the carbon nanotubes have high surface area, making them useful for adsorbing various active molecules. Hence, delivery by carbon nanotubes can enhance bioactivity of the active molecules [88].

In 2008, Liu *et al* synthesized poly(ethylene glycol) (PEG)-grafted single-walled carbon nanotubes (SWCNTs) and conjugated them with paclitaxel. The material

showed promise in tumor-targeted accumulation in mice, and exhibited biocompatibility, excretion, and little toxicity. It also showed high treatment efficacy and minimum side effects for cancer therapy with low drug doses [103].

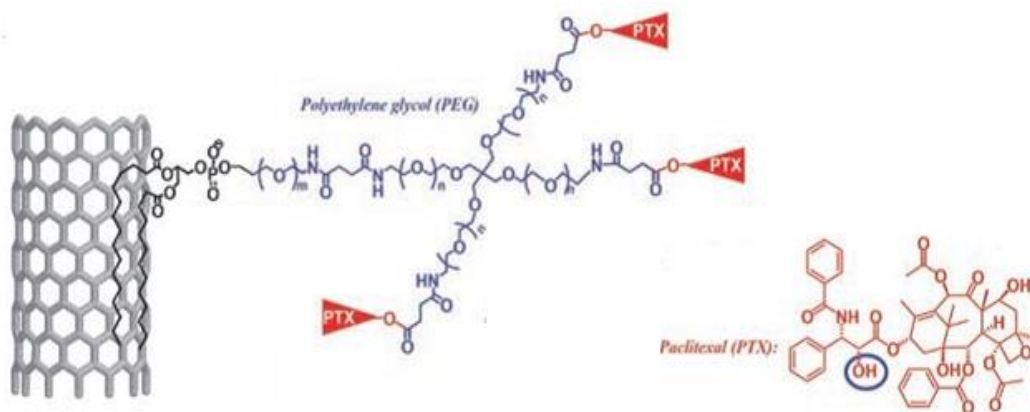


Figure 2.18 Schematic representation of paclitaxel conjugation to SWNT functionalized by phospholipids with branched PEG chains [103].

In 2011, Varkouhi *et al* studied the use of carbon nanotubes as carrier for siRNA. The carbon nanotubes were functionalized with a cationic polymer, polyethylenimine (PEI) and pyridinium, via covalent and non-covalent bond, respectively. Then, the functionalized carbon nanotubes were bound with luciferase specific and non-specific siRNA via simple mixing. Next, silencing activity and cell viability were investigated. CNTs-PEI and CNTs-pyridinium showed 10–30% silencing activity and 10–60% cytotoxicity. However, they did not significantly increase the silencing activity as compared with standard transfection systems [104].

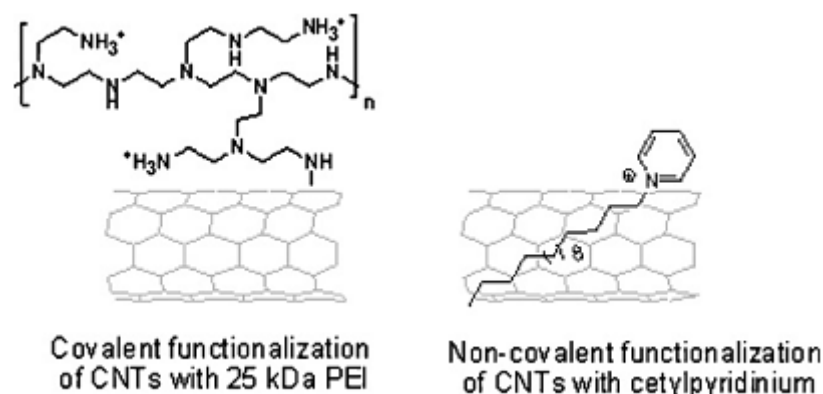


Figure 2.19 Schematic illustration of the covalent functionalization of CNTs with PEI (left) and non-covalent functionalization of CNTs with cetylpyridinium [104].

2.6.2 Graphene Oxide

Graphene oxide is a two dimensional material derived from graphite or graphene by oxidation. Due to the oxidative functionalization, oxygen species such as hydroxyl, epoxide and carbonyl moieties are introduced into the carbon network structure. Graphene oxide has attracted much interest because of its versatile properties, making it available for numerous applications such as electronics, conductive films, electrode materials, composites as well as biomedical applications [100,105,106].

In 2008, Sun *et al* synthesized and evaluated the biological applications of nano-graphene oxide (NGO). They chemically functionalized NGO with PEG star-polymers in order to improve its solubility in aqueous media. Anticancer drug with aromatic substructure, doxorubicin, was loaded onto the PEGylated NGO sheets via simple physisorption. The drug was selectively delivered into cancer cells by antibody-conjugated NGO and showed effective anti-cancer activity. It was concluded that the novel graphitic nanostructures with multi-functionalities showed promise in biological applications [33].

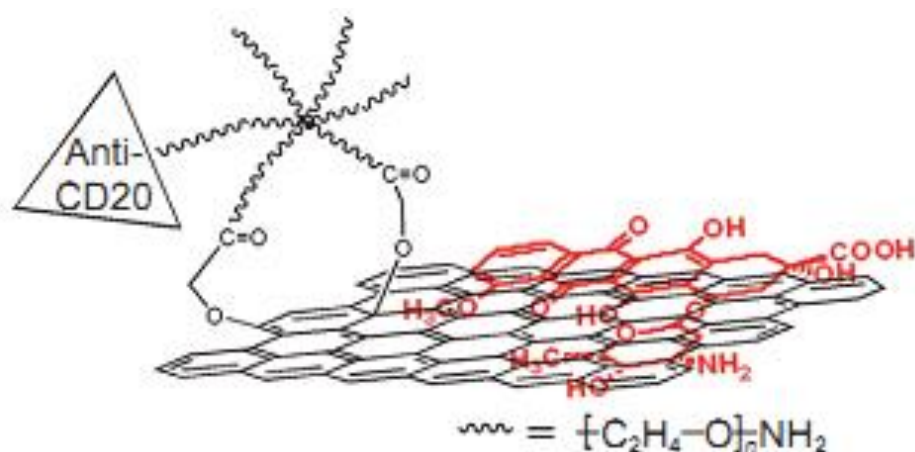


Figure 2.20 Schematic demonstration of PEGylated nanographene oxide for targeted drug delivery [33].

In 2011, Tian *et al* fabricated photosensitizer-loaded PEG-functionalized graphene oxide (GO) with excellent water solubility. The obtained graphene carrier exhibited capability for photodynamic therapy (PDT). Chlorin e6 (Ce6, (17S,18S)-18-(2-carboxyethyl)-20-(carboxymethyl)-12-ethenyl-7-ethyl-3,8,13,17-tetramethyl-7,18,22,23-tetrahydroporphyrin-2-carboxylic acid), which is a photosensitizer molecule, could generate cytotoxic singlet oxygen under light excitation, leading to destruction of human nasopharyngeal epidermal carcinoma KB cells. Furthermore, exposing the graphitic structure to near-IR at a low power density could promote delivery of Ce6, resulting in enhancement of activity in photodynamic cancer therapy [107].

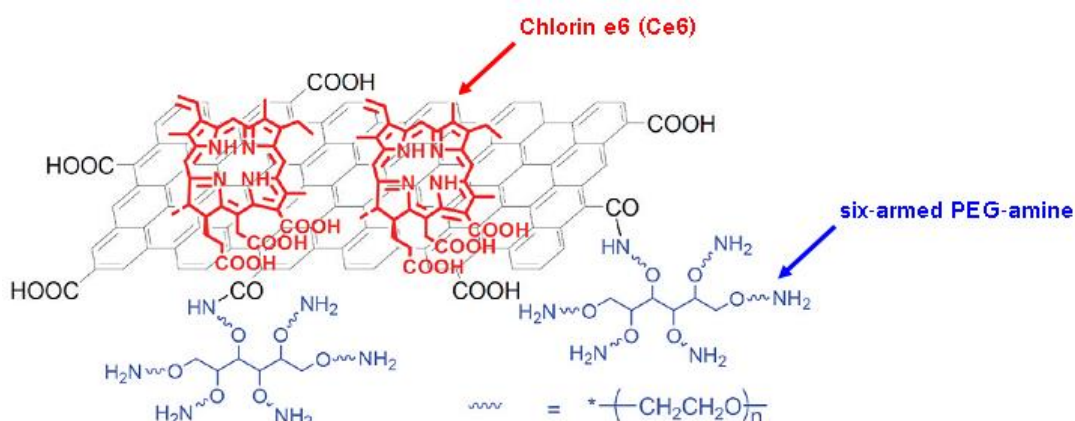


Figure 2.21 Schematic demonstration of Ce6 loaded on GO-PEG [107].

In 2013, Di *et al* demonstrated the use of functional graphene oxide with polyethylenimine and poly(ethylene glycol) (GO-PEI-PEG) as a plasmid-based Stat3-specific small interfering RNA (siRNA) carrier for antitumor therapeutics *in vivo*. The Stat3 (signal transducer and activator of transcription 3) is a transcription factor, which is encoded by the Stat3 gene in human. The results indicated significant decrease in tumor growth after treatment with plasmid-based Stat3 siRNA delivered by GO-PEI-PEG [101].

2.6.3 PEGylation

According to previous literatures, there are several strategies to reduce toxicity of carbon-based materials e.g., modification with biocompatible polymers to make them water dispersible, and conjugation with specific targeting molecules to direct them towards required sites [11,108-110].

In 2011, Bottini *et al* reviewed the research articles on the application of poly(ethylene glycol)-modified carbon nanotubes (PEG-modified CNTs) as *in vitro* and *in vivo* therapeutic and imaging tools and described what was known about the interaction between the PEG-modified CNTs and biological systems. They summarized that the PEG-modified CNTs possess good biological performance, i.e., pharmacokinetic profile, biocompatibility and cell internalization, trafficking and excretion [34].

In 2011, Robinson et al developed potential photothermal therapy using nanosized reduced graphene oxide (nano-rGO) sheets. The material was functionalized with poly(ethylene glycol). It exhibited high near-infrared (NIR) light absorbance and is biocompatible. Moreover, a targeting peptide bearing the Arg-Gly-Asp (RGD) motif which is specific with human glioblastoma-astrocytoma (U87MG), was attached to the materials. The results indicated that nano-rGO with the NIR irradiation provided highly effective photoablation of the cells *in vitro* and was applicable for photothermal treatment of tumor *in vivo*. [95].

2.7 Research objective

Cluster of carbon nanospheres, or the so called oxidized carbon nanospheres (OCSs), is a new morphology of carbon material, composed of cluster of carbon nanomaterials derived from an assembly of graphene oxide sheets together with giant fullerenes and/or giant bulky balls during oxidation/exfoliation process of graphite or graphene nanoplatelet. OCSs properties including water dispersability, size and biocompatibility, encourage me to explore its applications in biomedical applications. Here, the OCSs are synthesized and applied as carriers for delivery of organic molecules and anti-cancer drugs. As mentioned above, there are many other oxidized carbon materials that have shown delivery ability in drug delivery application, therefore, I would like to compare them with the OCSs. I have, therefore, in this thesis, investigated effect of morphology of the oxidized carbon materials on intercellular uptake toward cancer cells. In addition, the mechanism of the uptake ability will be studied in details using cell-sized liposomes. Furthermore, effect of lipid membrane composition, surface property of the carriers as well as cargos on the carrier-membrane interaction are also elucidated.

CHAPTER III

EXPERIMENTAL

3.1 Synthesis and Characterization of Oxidized Carbon Nanospheres (OCSs), Oxidized Graphene Sheets (OGShs) and Oxidized Carbon Nanotubes (OCTs)

Oxidized carbon nanospheres (OCSs) and oxidized graphene sheets (OGShs) were prepared using the following protocol. Firstly, graphite powder (1 g, Thai Carbon and Graphite Co., Ltd., Bangkok, Thailand) and sodium nitrate (1 g, Suksapan, Bangkok, Thailand) were grinded and mixed together. Then, the mixed powder was dispersed in 18 M sulfuric acid (50 mL, Sigma-Aldrich, St. Louis, USA) and stirred until the homogeneous suspension was obtained. After that, the sonication was applied to the suspension with the frequency of 40 kHz at room temperature for 1 h. Next, 6 g of KMnO_4 (Suksapan, Bangkok, Thailand) was slowly added into the suspension with stirring for 90 min, followed by the addition of 100 mL of water. Then, the reaction temperature was allowed to increase up to 90 °C for 30 min. Next, the additional 300 mL of water was added and the suspension was stirred for 10 min. After that, 50 mL of 5% (w/v) H_2O_2 was added and the mixture was stirred at room temperature for 30 min to remove the excess KMnO_4 . Finally, the mixture was purified by dialysis against water (CelluSep T4, MWCO of 12,000–14,000 Da, Membrane Filtration Products, USA), until pH 5-6 was reached. After that, OCSs and OGShs were separated from the mixture using gradient centrifugation as follows. Firstly, the suspension was centrifuged at 9,400 g for 10 min to separate the big size residues. Then, the supernatant was collected and centrifuged at 11,300 g for 15 min. After that, the supernatant collected from this step was centrifuged at 21,100 g for 15 min to precipitate OGShs. Finally, the obtained supernatant was centrifuged at 37,000 g for 30 min. OCSs are in the supernatant obtained from the final step. Oxidized carbon nanotubes (OCTs) were prepared by oxidizing of single-walled carbon nanotubes (SWCNTs, Sigma-Aldrich, St. Louis, USA) using the same protocol as OCSs and OGShs. However, the sonication step was omitted and the reaction time was decreased to be 30 min. For functional groups characterization, OCSs, OGShs and OCTs were subjected to an attenuated total

reflectance fourier transform infrared spectrometer (ATR-FTIR, Nicolet 6700, Thermo Electron Corporation, Massachusetts, USA) and an X-ray photoelectron spectrometer (XPS, Kratos AXIS Ultra DLD instrument, Kratos, Manchester, England) operated using a monochromatic Al K α X-ray source at 1486.6 eV, 150 W, 15 kV and 10 mA. Furthermore, an X-ray diffractometer (XRD, Rigaku DMAX 2200/Ultima+, Rigaku, Tokyo, Japan) using a Cu K α radiation source and operating at 40 kV and 30 mA was used to investigate crystallinity of the materials. Morphology of all materials was determined by a scanning electron microscope (SEM, JSM-6400, JEOL, Tokyo, Japan), with gold ion sputtering under vacuum at 15 kV for 90 s and observed at an accelerating voltage of 20 kV, and transmission electron microscopy (TEM; JEM-2100, JEOL, Tokyo, Japan) operated at 100–120 kV. In addition, hydrodynamic diameter and zeta potential value were evaluated by a zetasizer (nanoseries model S4700, Malvern Instruments, Worcestershire, UK). Osmolality of the aqueous suspension of all materials was also investigated by an osmometer (210 Micro-Sample Osmometer, Fiske®, Pennsylvania, USA).

Table 3.1 Gradient centrifugation.

Rotation speed (RCF)	Time (min)	Precipitate
9,400 g	10	Big size residues
11,300 g	15	Big tubes and sheets
21,100 g	15	OGShs
37,000 g	30	OCSs (supernatant)

3.2 PEGylation of Oxidized Carbon Nanospheres (OCSs), Oxidized Graphene Sheets (OGShs) and Oxidized Carbon Nanotubes (OCTs) and Characterization

In order to modify surface's functional groups of the three oxidized carbon materials with methoxy-terminated polyethylene oxide carboxylic acid (mPEO-COOH), the mPEO-COOH was first prepared using the following procedure. Firstly, 10 g of polyethylene glycol methyl ether (mPEG, Mn 5,000, Sigma-aldrich, Missouri, USA) were dissolved in dimethyl formamide (20 mL), followed by the addition of an excess amount of succinic anhydride (Acros Organics, Geel, Belgium) and a catalytic amount of pyridine (?? drops, Carlo Erba Reagents, Val de Reuil, France). The mixture was stirred at 60 °C overnight. After that, it was dialyzed against water using benzoylate dialysis tubing (MWCO 2000; Sigma-Aldrich, St Louis, MO, USA), before being freeze dried. The product was subject to a 400 MHz nuclear magnetic resonance spectrometer (¹H NMR, Varian Company, California, USA), in D₂O.

Yield = 60%, ¹H NMR (D₂O, 400 MHz, ppm): 2.51 (-COCH₂CH₂COOH), 4.11 (-OCH₂CH₂OCOCH₂CH₂-COOH), 3.35–3.70 (-OCH₂CH₂OCH₃) and 3.20 (-OCH₂CH₂OCH₃).

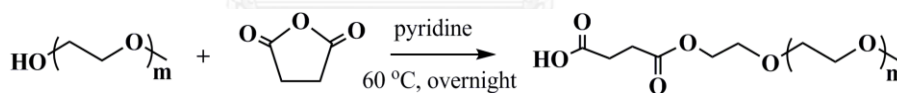


Figure 3.1 Synthesis of mPEO-COOH.

The obtained mPEO-COOH was, then, grafted onto carbon materials' surface by coupling reaction as follows. Firstly, 5 mg of mPEO-COOH were dissolved in deionized water (1 mL) until the clear solution was obtained. After that, aqueous solution of 1-ethyl-3-(3-dimethylaminopropyl)carbodiimide (EDCI, 0.30 mg) was slowly added and the mixture was stirred under N₂ atmosphere at 0 °C for 30 min. Then, N-hydroxysuccinimide (NHS, 0.25 mg in 0.5 mL water) was added into the reaction. Finally, 5 mg of the carbon materials (400 ppm, 12.5 mL) was added. The reaction was

further stirred overnight and then, purified by dialysis against water using the cellulose membrane (CelluSep T4, MWCO of 12,000–14,000 Da, Membrane Filtration Products, USA). The mPEO-grafted oxidized carbon materials were characterized by ATR-FTIR.

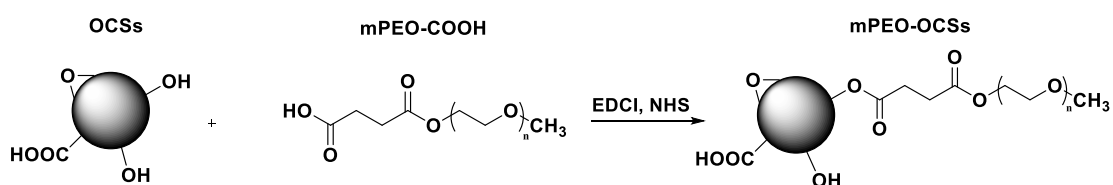


Figure 3.2 Synthesis of mPEO-grafted oxidized carbon materials.

3.3 Rhodamine- and Fluorescein-Labeling of Oxidized Carbon Materials

Two types of fluorescence dye, rhodamine B sulfonyl chloride (Lissamine, Life Technologies, California, USA) and 6-aminofluorescein (Sigma-Aldrich, Missouri, USA), were used to track the oxidized carbon materials. Rhodamine was grafted on the oxidized carbon materials via chemical reaction between sulfonyl group of rhodamine and hydroxyl group of the oxidized carbon materials. Rhodamine B sulfonyl chloride (2 mg) was dissolved in DMF (50 μ L). Then, aqueous suspension of oxidized carbon materials (4 mg in 2 mL of water) was added. The reaction was stirred under N_2 atmosphere for overnight. The product was purified by dialysis against water. In the case of 6-aminofluorescein, it was grafted onto the oxidized carbon materials' surface through the coupling reaction using EDCI and NHS. Firstly, aqueous suspension of the oxidized carbon materials (400 ppm, 5 mL) was stirred with the slow addition of 2.2 mg of EDCI in water (1 mL) at 0 $^{\circ}$ C, under N_2 atmosphere. The mixture was, then, stirred for 30 min, followed by the addition of aqueous solution of NHS (1.3 mg in 1 mL MilliQ water). Then, the solution of 6-aminofluorescein in acetone (2000 ppm, 0.5 mL) was slowly dropped into the reaction and the mixture was further stirred for overnight. The unreacted reagents were eliminated by dialysis against water using cellulose membrane. Degree of substitution of the dyes was determined by indirect

method as follows. Dialysate was collected every 3 h during the dialysis, and subjected to a uv-vis spectrophotometer (Optizen POP, Mecasys, Daejeon, Republic of Korea) to quantify the amount of unreacted dye. This step was repeated until the absorption peak of the dye could not be detected. The percentage of covalently bound dye was calculated by the following equation:

$$\text{Covalently bound dye (\%)} = [(W_{\text{initial dye}} - W_{\text{unreacted dye}}) / W_{\text{oxidized carbon}}] \times 100 \quad (1)$$

where $W_{\text{initial dye}}$ is the initial weight of dye, $W_{\text{unreacted dye}}$ is the weight of unreacted dye, and $W_{\text{oxidized carbon}}$ is the weight of oxidized carbon materials.

3.4 Curcumin Loading

Curcumin was loaded on the oxidized carbon materials by simple mixing method. Firstly, curcumin solution (0.2 mg in 0.2 mL ethanol) was slowly added into aqueous suspension of the oxidized carbon material (400 ppm, 1 mL) under sonication, followed by incubation under light protection at room temperature for 4 h. After that, unloaded curcumin was eliminated by dialysis against water using cellulose membrane. The dialysate was replaced every 3 h with pure water at least 5 times or until there is no curcumin absorption peak could be detected from the dialysate. Loading content of curcumin was determined by indirect method. During the dialysis, the dialysate was collected. Unloaded curcumin in the dialysate was quantified using uv-vis spectroscopy at the maximum wavelength of 425 nm. Loading of curcumin was, then, calculated using the following equation:

$$\text{Loading of curcumin (\%)} = [(W_{\text{initial}} - W_{\text{unloaded}}) / W_{\text{total}}] \times 100 \quad (2)$$

where $W_{initial}$ is the initial weight of curcumin, $W_{unloaded}$ is the weight of unloaded curcumin and W_{total} is the weight of curcumin-loaded carbon material.

3.5 Anti-cancer Drugs Loading

Paclitaxel (PTX, Sigma-aldrich, Missouri, USA) and doxorubicin (DOX, Merck, Darmstadt, Germany), the hydrophobic and hydrophilic anti-cancer drugs, respectively, were separately loaded onto the OCSs by the simple mixing method as used for curcumin loading. For paclitaxel, 1 mM of stock solution was firstly prepared by dissolving 1 mg of paclitaxel in 1.15 mL of dimethyl sulfoxide (DMSO, RCI Labscan, Bangkok, Thailand). Then, 100 μ L of paclitaxel stock solution was slowly dropped into OCSs aqueous suspension (400 ppm, 10 mL), followed by incubation under light protection at 4 °C for 3 h. Next, unloaded paclitaxel was eliminated by dialysis against water. In order to evaluate the loading content of paclitaxel, the same protocol was used but the stock solution of paclitaxel was prepared using methanol (Merck, Darmstadt, Germany) instead of DMSO and the purification by the dialysis was omitted. The amount of unloaded paclitaxel was quantified by the following procedure. Firstly, the mixture after incubation was filtering centrifuged at 2,350 g for 10 min. This step was repeated 3 times until all fluid was centrifuged downward through the membrane. The filtrates from all steps were collected and subjected to the uv-vis spectroscopy to measure the absorption of paclitaxel at 232 nm with the aid of calibration curve. In the case of doxorubicin, it was prepared using the same protocol as paclitaxel but DMSO was used as a solvent for all experiment. The stock solution of doxorubicin was prepared by dissolving 1.2 mg of doxorubicin in 1 mL of DMSO. Then, 268 μ L of the doxorubicin stock solution was slowly added into the OCSs aqueous suspension (400 ppm, 10 mL). The amount of unloaded doxorubicin was also detected using uv-vis spectroscopy at 480 nm. Loading content of the anti-cancer drugs was calculated using the following equation:

$$\text{Loading of drug (\%)} = [(W_{\text{initial}} - W_{\text{unloaded}}) / W_{\text{total}}] \times 100 \quad (3)$$

3.6 Liposome Preparation and Interaction of Oxidized Carbon Materials with Lipid Bilayer Membrane

Two types of cell-size liposomes, liquid-disordered phase liposome (Ld) and liquid-ordered phase liposome (Lo), were prepared by dehydration method from dioleoyl L- α phosphatidylcholine (DOPC, Avanti Polar Lipid, Alabama, USA) and dipalmitoylphosphatidylcholine (DPPC, Avanti Polar Lipid, Alabama, USA) with the presence of cholesterol (Avanti Polar Lipid, Alabama, USA), respectively. Firstly, 20 μL of the lipid solution in chloroform (2 mM) was added into glass vial. Then, 12 μL of glucose in methanol (10 mM) was mixed with the lipid solution. After that, the mixed solution was dried up by flowing nitrogen gas to make a thin film. The dried film was kept under vacuum for 3 h, before the addition of MilliQ water (200 μL). Next, the suspension was kept at 37 $^{\circ}\text{C}$ for 3 h to hydrate the lipid film and allow the formation of cell-size liposomes. In addition, liquid-disordered phase liposome (Ld) with the fluorescence labeling was prepared from DOPC with the presence of 23-(dipyrrometheneboron difluoride)-24-norcholesterol (BODIPY-cholesterol, Avanti Polar Lipid, Alabama, USA). Ninety microliters of DOPC solution in chloroform (10 mM) was mixed with 90 μL of BODIPY-cholesterol (0.1 mM). Then, the same protocol for preparing Ld and Lo cell-sized liposomes was used. To observe interaction of the oxidized carbon materials with cell-sized liposomes, the obtained liposome suspension in water was mixed with the aqueous suspension of oxidized carbon materials. The final concentrations of liposome and oxidized carbon materials after mixing were controlled at 0.1 mM and 100 $\mu\text{g/mL}$, respectively. Then, the mixture was dropped on the glass slide with silicon chamber and observed using a confocal laser fluorescent microscope (CLFM, FV-1000, Olympus, Tokyo, Japan). To investigate incubation time-dependence of interaction between OCS_{Rho} and cell-sized liposome, the mixture was observed at 0, 1, 2, 3 and 4 h after mixing.

3.7 Anthocyanin Leakage

Cell-size liposomes containing anthocyanin were prepared using the same protocol as the Ld liposomes preparation but 1000 $\mu\text{g}/\text{mL}$ anthocyanin solution (freshly made) in MilliQ water (2 mL) was used to hydrate the lipid film instead of pure water. Then, the solution was kept at 37 $^{\circ}\text{C}$ for 2-3 h to allow the formation of cell-size liposomes containing anthocyanin inside the vesicle. In order to eliminate excess anthocyanin outside liposomes, the liposome suspension was left to allow sedimentation. Then, certain volume of water above the sediment liposomes was carefully removed, followed by the addition of same volume pure MilliQ water. This step was repeated 2 times until the solution has no color. The obtained liposomes was mixed with MPC with concentration of 750 $\mu\text{g}/\text{mL}$ and observed using laser confocal microscope (Nikon Digital Eclipse C1-Si/C1 Plus, Nikon, Tokyo, Japan) with excitation and emission wavelengths of 488/525 nm.

3.8 Penetration of Lipid-loaded OCSs into Liposome.

Transient pore formation upon surface activity of OCSs was investigated. The OCSs were reduced their surface activity by being loaded with lipid molecules prior to observation of the penetration into liposomes. DOPC (0.8 mg) was loaded on OCSs_{Rho} by the addition of the OCSs_{Rho} aqueous suspension into dried lipid with the weight ratios of DOPC/OCSs_{Rho} = 10:1. Next, the DOPC-loaded OCSs_{Rho} (400 ppm, 500 μL) was mixed with Ld liposomes (0.2 mM, 500 μL). The final concentrations of liposome and lipid-loaded OCSs_{Rho} were controlled at 0.1 mM and 200 $\mu\text{g}/\text{mL}$, respectively. Then, the mixture was subjected to CLFM to observe the penetration compared with OCSs_{Rho}.

3.9 Association of Curcumin-loaded OCSs on Lipid Membrane

In order to evaluate the effect of cargo on the ability to penetrate through lipid bilayer membrane of OCS, curcumin-loaded OCSs_{Rho} and Ld liposomes consisting of DOPC (0.2 mM) were prepared as described in the previous section. After that,

curcumin-loaded OCSs_{Rho} (300 ppm, 100 μ L) were mixed with the Ld liposomes (0.2 mM, 100 μ L). The final concentration of curcumin-loaded OCSs_{Rho} and liposomes were controlled at 150 ppm and 0.1 mM, respectively. The mixture was, then, observed by CLFM with $\lambda_{ex}/\lambda_{em} = 488/525, 561/595$.

3.10 Adsorption of Lipid on OCSs' Surface at Different pH

Lipid adsorption ability of OCS at pH 5.5 and 7.4 was compared using 1,2-dimyristoyl-sn-glycero-3-phosphoethanolamine-N-(lissamine rhodamine B sulfonyl) (DMPE-RhB, Avanti Polar Lipid, Alabama, USA) as a representative lipid. DMPE-RhB was loaded on the OCSs as follows. Three hundred microliters of DMPE-RhB in chloroform (1.0 mg/mL) were added into a glass vial. Then, chloroform was evaporated by flowing N₂ gas. Next, 3.0 mL of OCSs suspension (200 μ g/mL) in PBS (pH 5.5 or 7.4) were added into the dried lipid before shaking. The suspension was left at room temperature for 2 h to allow adsorption of the lipid molecules onto the OCSs. After that, the un-adsorbed lipid was removed by the addition of ethanol to give the final concentration of 60 % (v/v). The suspension was filtering centrifuged using a cellulose membrane filter (10kDa, Millipore, Massachusetts, USA) at 4700 g. After that, the residue was diluted with 500 μ L of 60 % (v/v) ethanol and the filtration was repeated four times. The total filtrate was collected and subjected to UV-visible spectrophotometric analysis at 550 nm to quantify the amount of DMPE-RhB, with the aid of the calibration curve constructed with DMPE-RhB standard solutions.

3.11 Cytotoxicity of Oxidized Carbon Materials

Adenocarcinomic human alveolar basal epithelial cells (A549, ATCC, Virginia, USA) and the cells resistant to etoposide (A549RT-eto, developed and kindly provided by Chulabhorn Research Institute, Bangkok, Thailand) were cultured in RPMI1640 culture medium, supplemented with 10% (v/v) fetal bovine serum, penicillin (100 U/mL), streptomycin (100 μ g/mL) and amphotericin B (125 ng/ mL) (all antibiotics were

obtained from Gibco, New York, USA), in a 80% relative humidified atmosphere of 5% (v/v) CO₂ at 37 °C. Cell viability was determined by the MTT method. Cell suspensions in culture medium were seeded in 96-well plates (100 µL/well) with the cell amount of 1×10⁴ cells/well and incubated at 37 °C in a humidified atmosphere of 5% (v/v) CO₂ for 24 h to allow adhesion of cells on the plate. After that, 100 µL of culture medium containing the desired concentration of sample was added to each well, followed by further incubation for 72 h. Next, the fluid in each well was removed. Then, fresh culture media containing 0.5 mg/ml of (3-[4,5-dimethylthiazol-2-yl]-2,5-diphenyltetrazolium bromide) (MTT, Sigma-Aldrich, Missouri, USA) was added, followed by incubation for 2 h at 37 °C. After 2 h, the medium was removed and DMSO (100 µL/well) was added to dissolved the crystal. Finally, the absorbance was measured at 550 and 650 nm in a micro plate reader. The difference between the absorbance at 550 and 650 nm was used to evaluate the relative number of viable cells. Assays were performed in triplicate independently and data are presented as the percent viability compared to control.

3.12 Cellular Uptake of Oxidized Carbon Materials

The intracellular uptake of all materials was investigated against A549 cells. The cells were cultured in six-well plates in 1 mL of culture medium supplemented with antibiotics as described in previous section. Then, the plate containing cells was incubated in 80% relative humidified atmosphere of 5% (v/v) CO₂ at 37 °C for overnight to allow the adhesion. Next, the cells were treated with the samples, of which final concentration was controlled at 10 µg/mL, and incubated at 37 °C under 5% (v/v) CO₂ for 4 h. After that, the media were removed and the cells were washed twice with culture medium. Next, Hoechst was used to stain the nucleus with the concentration of 0.1 mg/mL in culture media. The media was, then, removed and the cells were washed with culture media, followed by being fixed with 4% paraformaldehyde. The cells were, finally, washed with culture media before being observed by a confocal laser fluorescent microscope (CLFM) equipped with Plan Apochromat VC 100x, a 32-

channel-PMT-spectral-detector (Nikon Digital Eclipse C1-Si/C1 Plus, Nikon, Tokyo, Japan). Excitation was carried out using diode lasers (405, 488 and 561 nm; Melles Griot, New Mexico, USA), and fluorescent spectral signals at 450, 525 and 595 nm were collected



CHAPTER IV

RESULTS AND DISCUSSION

4.1 Synthesis and Characterization of Oxidized Carbon Nanospheres (OCSs), Oxidized Graphene Sheets (OGShs) and Oxidized Carbon Nanotubes (OCTs)

Oxidized carbon nanospheres and oxidized graphene sheets were prepared from oxidation by modified Hummers' method. After gradient centrifugation, OCSs and OGShs were obtained, whereas OCTs were achieved by oxidizing of SWCNTs. Morphology of the oxidized carbon materials were observed by scanning electron microscopy (SEM) and transmission electron microscopy (TEM) as shown in Figure 4.1. OCSs possess the spherical shape with the diameter of 100-200 nm, whereas OCTs have tubular shape with the aspect ratio of 10 and an average length of 1 μm , and OGShs exhibit sheet shape with the size of 0.5 x 0.5 μm .

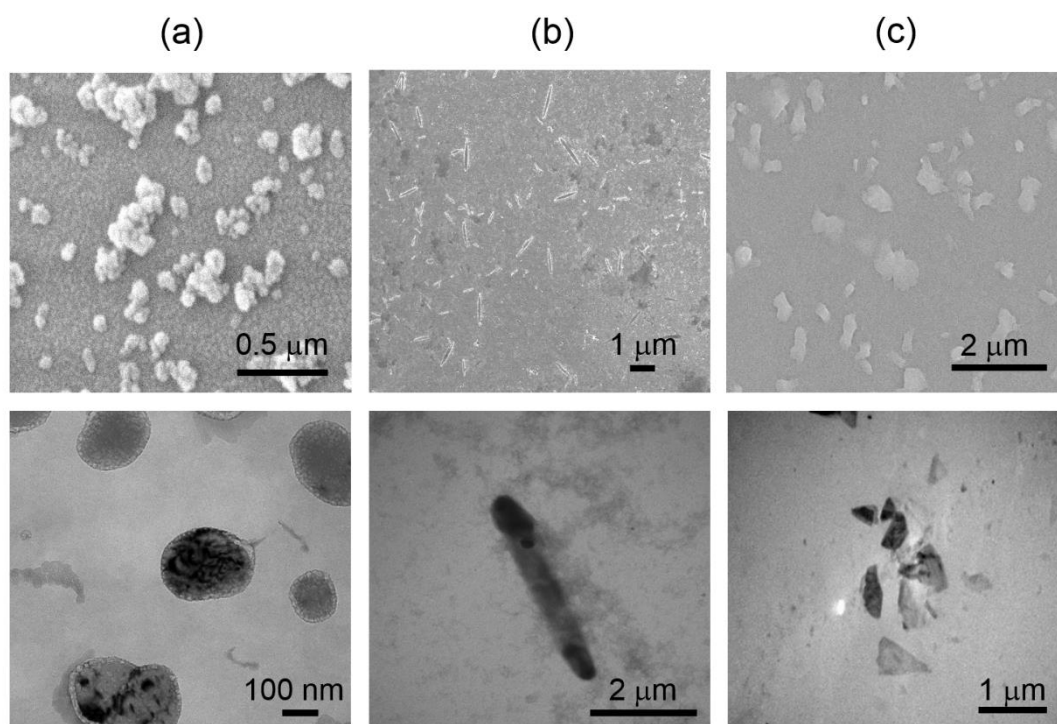


Figure 4.1 SEM (top) and TEM (bottom) photographs of (a) OCSs, (b) OCTs and (c) OGShs.

Next, the materials were characterized by ATR-FTIR and XPS. As shown in Figure 4.2, ATR-FTIR spectra of OCSs and OGShs exhibit the same functional groups, *i.e.*, O-H stretching ($3360\text{-}3367\text{ cm}^{-1}$), C=O stretching ($1712\text{-}1715\text{ cm}^{-1}$), C=C stretching ($1612\text{-}1614\text{ cm}^{-1}$) and C-O stretching ($1028\text{-}1042\text{ cm}^{-1}$). While, the spectrum of OCTs shows C=O and C=C stretching at around 1706 cm^{-1} and 1609 cm^{-1} , respectively.

For XPS analysis, the functional groups at the surface around 8 nm depth could be obtained. OCSs, OCTs and OGShs show the similar C1s spectra, which indicate C-C (283.6 eV), C=C (284.3 eV), C-O (286.3 eV), C=O (288.1 eV) and O-C=O (289.4 eV) functional groups. The O 1s spectra of the three materials indicated the presence of COOH (529.5 eV), C=O (531.7 eV), C-OH/C-O-C (533.0 eV) functional groups on the surface of the materials (Figure 4.3). These results indicate that graphite and SWCNTs were successfully oxidized into the oxidized carbon materials of different morphologies, *i.e.*, sphere (OCSs), tube (OCTs) and sheet (OGShs).

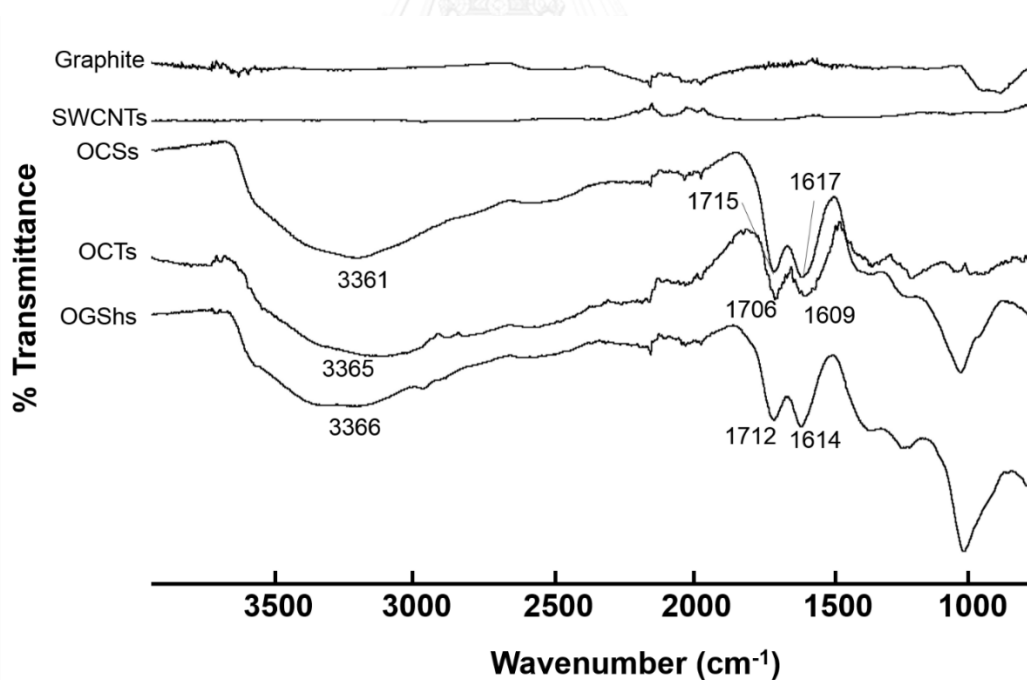


Figure 4.2 ATR-FTIR spectra of Graphite, SWCNTs, OCSs, OCTs and OGShs.

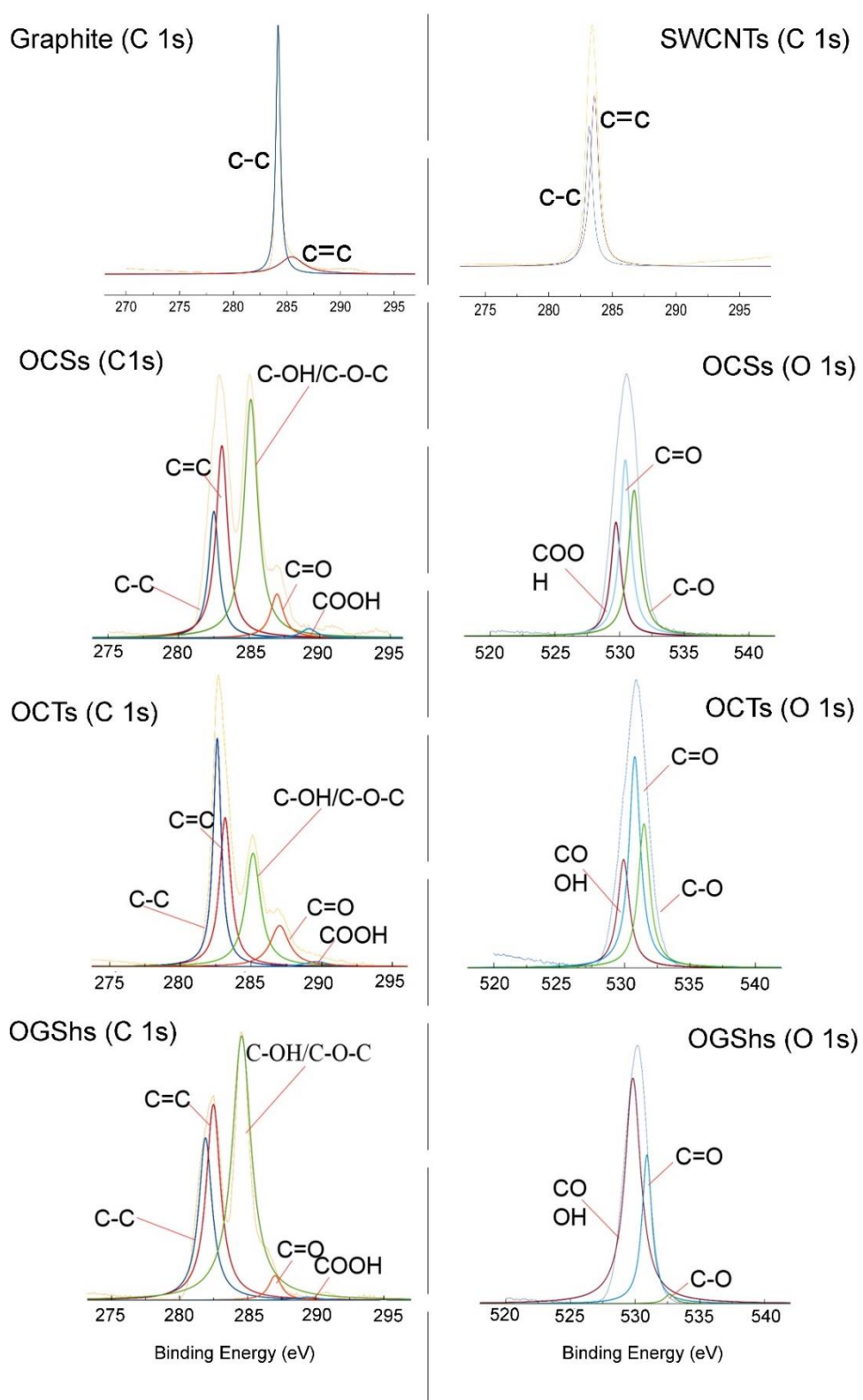


Figure 4.3 C 1s and O 1s XPS spectra of graphite, SWCNTs, OCSs, OCTs and OGShs.

Then, Raman spectroscopy was used to confirm the successful oxidation. As shown in Figure 4.4, the Raman spectra of the three oxidized carbon materials show two strong broad absorption bands at 1360 cm^{-1} (D band, tetrahedral sp^3 bonded carbons) and 1590 cm^{-1} (G band, sp^2 bonded carbons) with the three small peaks at 2720 , 2920 , and 3200 cm^{-1} (2D or G' band of disordered planar (sp^2) planes). The existence of the broad D and G bands indicates that the carbon network exhibits the disordered of the molecular plane, which is a result of oxidation process.

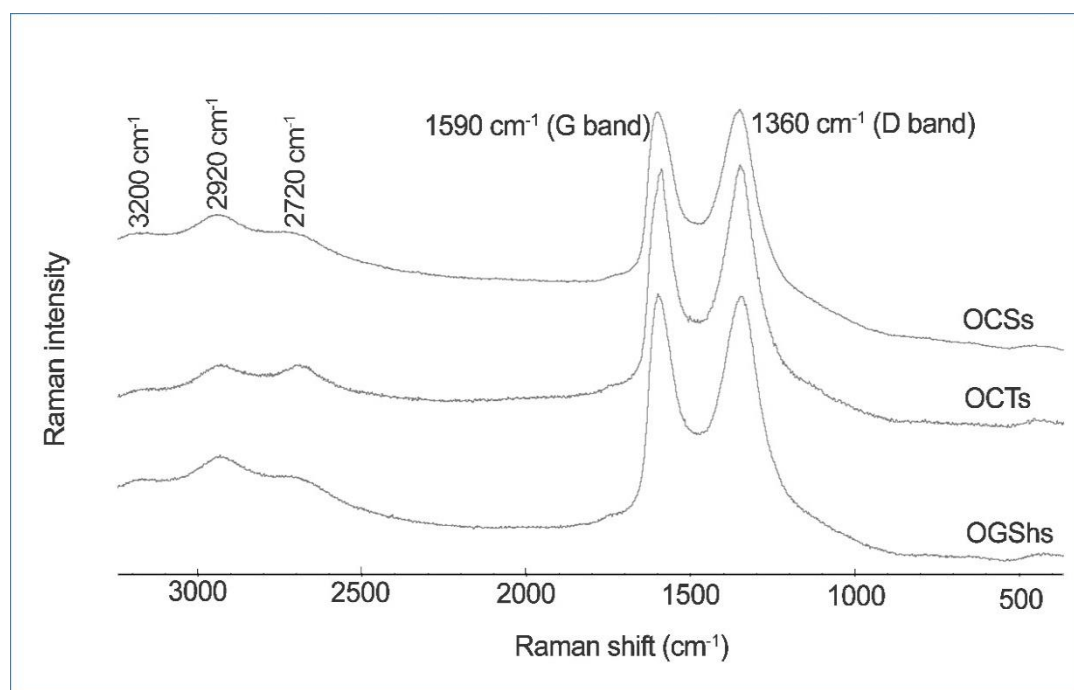


Figure 4.4 Raman spectra of OCSs, OCTs and OGShs.

Figure 4.5 shows X-ray diffraction patterns of pristine graphite, OCSs, SWCNTs and OCTs. As seen in the result, graphite exhibits a strong diffraction peak at 2θ around 26° . After oxidation, the OCS, nevertheless, show the broad diffraction peak around 10° . This result suggests that graphite was successfully oxidized into OCSs because the crystal stacking was broken down by the oxidation. In the case of OCTs, the diffraction pattern is almost the same as that of SWCNTs. This is because the

starting material SWCNTs did not possess the same level of ordered structure as graphite, the SWCNTs were already less crystalline and by oxidizing them, not much change of the crystallinity could be introduced. In addition, oxidation of SWCNTs was carried out shortly in order not to break down the tube structure. Therefore, no significant difference could be observed.

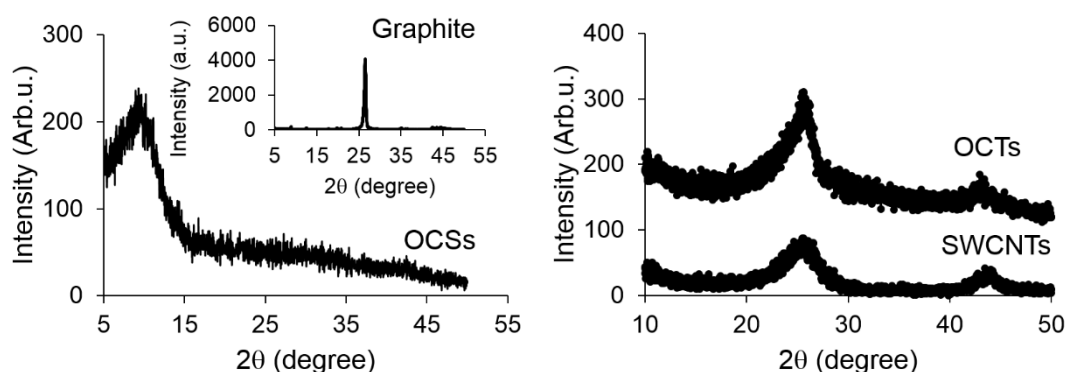


Figure 4.5 X-ray diffraction patterns of Graphite, OCSs, SWCNTs and OCTs.

After obtaining the three shapes of the oxidized carbon materials, hydrodynamic size and zeta potential were measured by dynamic light scattering (DLS) technique. The hydrodynamic diameter of OCS corresponds with the value estimated from SEM and TEM images (Table 4.1). All types of the oxidized carbon materials possess the negative charge of zeta potential, -42.6 ± 0.07 for OCS, -58.5 ± 1.27 for OCT and -71.4 ± 0.99 for OGSh. In the case of mPEO-OCS, hydrodynamic diameter becomes large compared with that of OCS without PEG modification, owing to swelling of mPEO moiety in water. The osmolality of all materials are almost zero. Dispersibility of OCSs in various solvents was, then, investigated. Dispersibility experiments revealed that the freeze-dried OCSs could be dispersed in several types of polar solvent, *i.e.*, water, cell culture media (DMEM), methanol, ethanol, dimethylformamide, dimethyl sulfoxide and ethyl acetate. The appearance of the OCSs suspension in various organic

solvents, water and cell culture media are shown in Figure 4.6. As seen in the figure, OCSs can disperse well in water and also polar organic solvents.

Table 4.1 Hydrodynamic diameter, zeta potential and osmolality of oxidized carbon materials and mPEO-OCS.

	OCS	OCT	OGSh	mPEO-OCS
Hydrodynamic diameter (nm) \pm SD	134.5 \pm 19.7	-	-	272.7 \pm 28.0
PDI	0.54	-	-	0.71
Zeta potential (mV) \pm SD	-42.6 \pm 0.07	-58.5 \pm 1.27	-71.4 \pm 0.99	-41.4 \pm 0.85
Osmolality (Osm/kg)	0	0	0	1

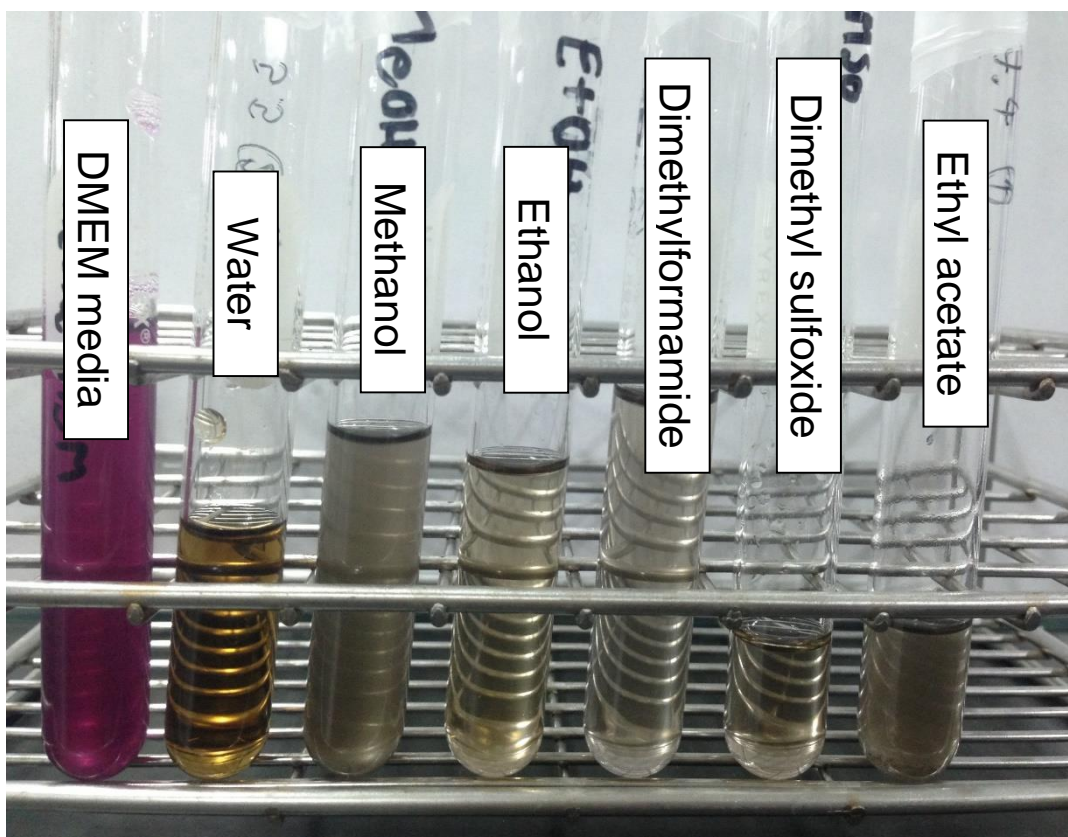


Figure 4.6 Appearance of OCSs dispersibility in various solvents.

The stability of OCSs suspension in aqueous media was, further, studied. OCSs aqueous suspension (400 ppm) was sonicated at 40 kHz prior to measurement of hydrodynamic diameter as a function of post sonication time using DLS. The result is shown in Figure 4.7 (see Figure A1 in the appendix for their size distribution profiles). As seen in the result, right after the sonication, OCS possesses the hydrodynamic diameter around 50-80 nm with a monodispersion. After being left at room temperature for a while, *i.e.*, 20, 30 min, 1, 2, 3, 4 and 8 h, the hydrodynamic diameter becomes large and the distribution curve shows a polydispersion with the broad peaks. This result indicates that OCSs exhibit some aggregation after keeping for long time. However, the aggregation could be reversed to the well dispersion by applying the sonication.

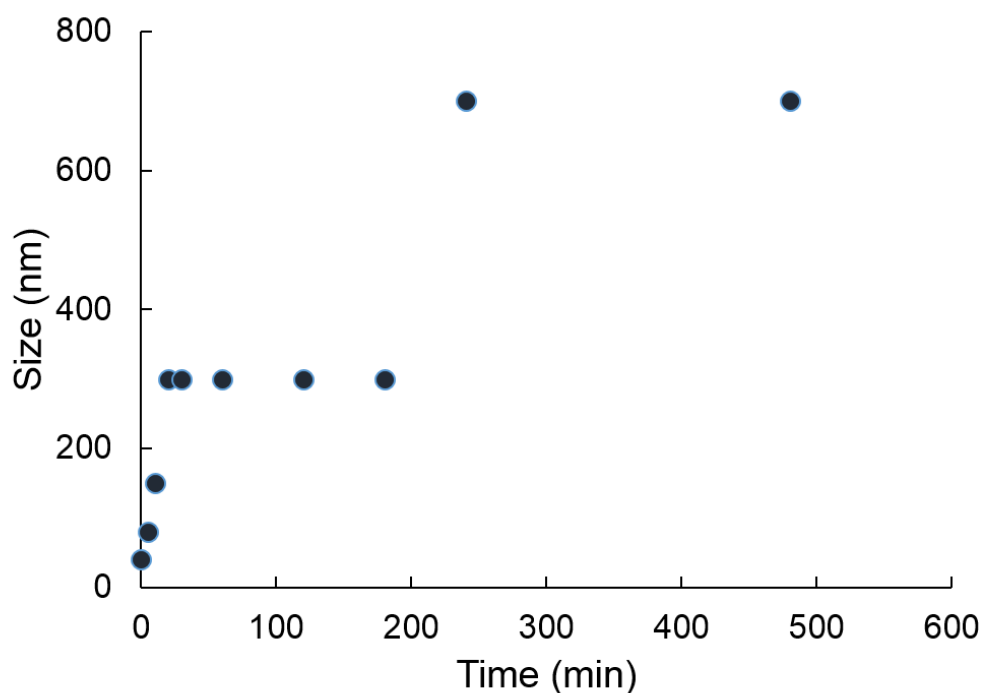


Figure 4.7 Hydrodynamic size distributions of an aqueous suspension of OCSs obtained at various post sonication times.

4.2 Polyethylene oxide functionalization

Methoxy-terminated poly(ethylene oxide) carboxylic acid (mPEO-COOH) was synthesized from the reaction between polyethyleneglycol methyl ether and succinic anhydride at 60 °C with a catalytic amount of pyridine. The obtained product is white powder and well-dissolved in aqueous media. The product was, then, characterized by ^1H NMR in D_2O as shown in Figure 4.8. As seen in the figure, protons at chemical shift 2.51 ppm represented methylene protons of succinyl group. This could be implied that the succinyl group was successfully grafted on the poly(ethyleneglycol) chain.

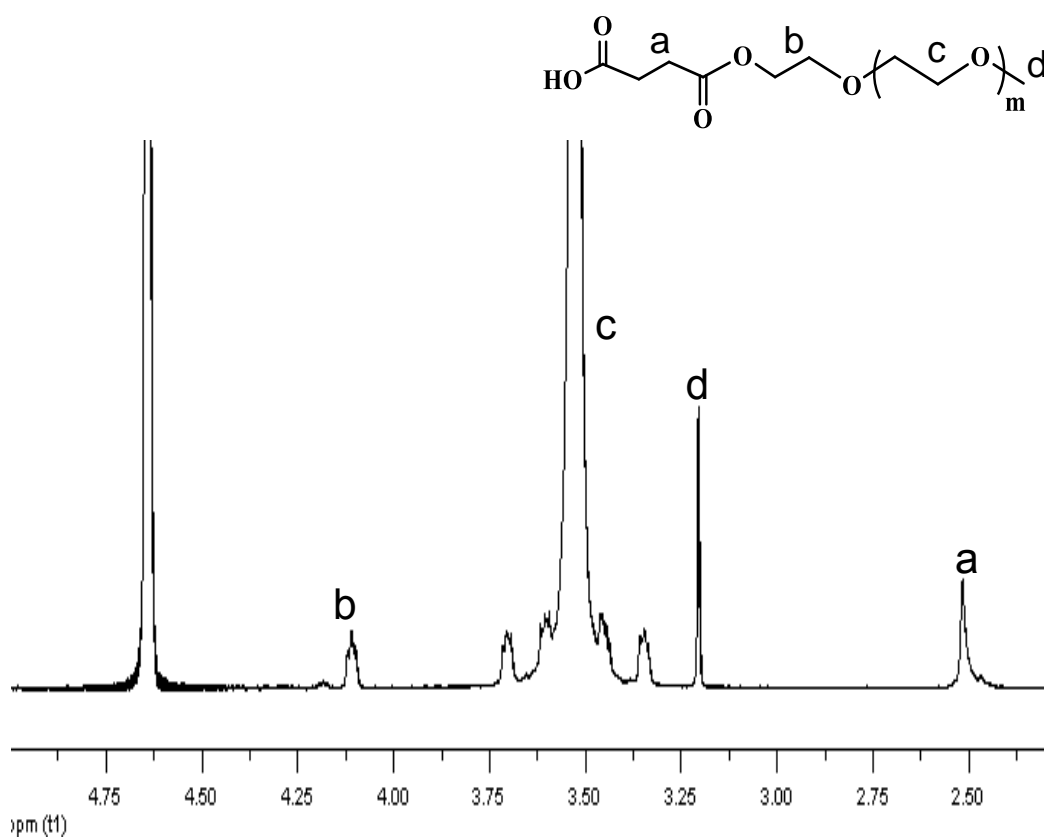


Figure 4.8 ^1H NMR spectrum of mPEO-COOH.

Next, the surface of OCSs, OCTs and OGSs were modified with mPEO-COOH using general coupling reaction of EDCI and NHS. The mPEO-OCSs were further characterized by ATR-FTIR. As shown in Figure 4.9, mPEO-OCS shows the characteristic peak of mPEG around 1094 cm^{-1} , which corresponds to C-O stretching of PEO chain. Moreover, a decrease in intensity of the peak around 3483 cm^{-1} , attributing to O-H stretching, in mPEO-OCSs spectrum indicates that mPEO-COOH was successfully grafted on hydroxyl groups of OCSs.

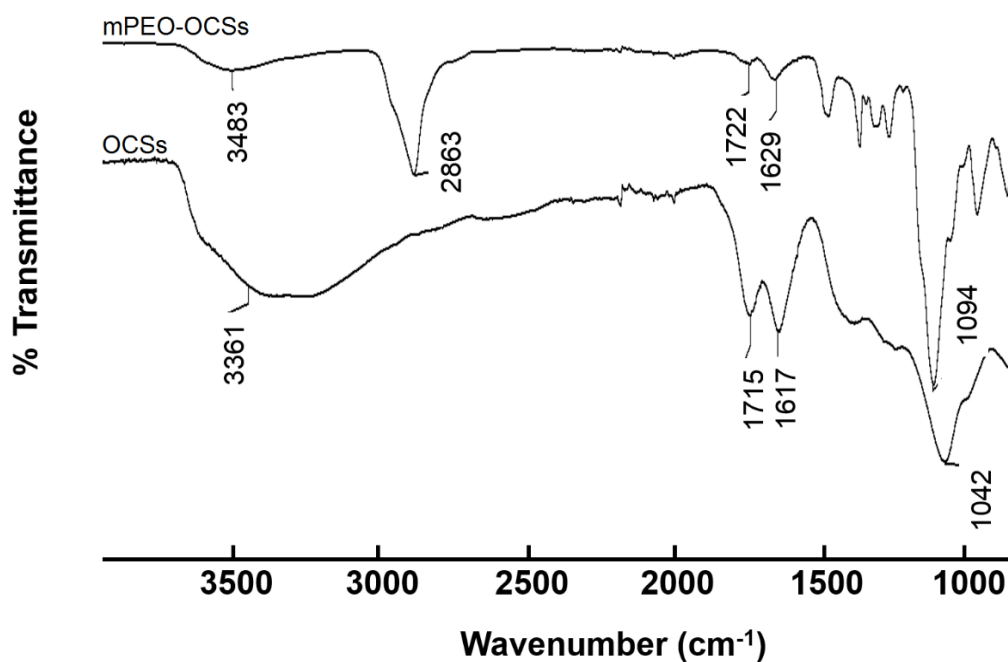


Figure 4.9 ATR-FTIR spectra of OCSs and mPEO-OCSs.

4.3 Interaction of Oxidized Carbon Materials with Lipid Bilayer Membrane

In order to investigate the effect of shape on the ability of lipid membrane association for the oxidized carbons, cell-sized liposomes were used (to mimic the cell plasma membrane). Then, the oxidized carbon materials were fluorescently labeled with rhodamine-B or fluorescein so the particles could be tracked under fluorescence microscope. Degree of the grafting of the dyes on the three materials were adjusted by trial and error (during the grafting reaction) to be in the same range (20-30%, specifically at 28.6%, 25.4% and 20.1%, for OCSs, OCTs, and OGShs, respectively).

4.3.1 Effect of Particle Shape

The effect of shape of the oxidized carbon materials on interaction with lipid bilayer membrane was evaluated using fluorescence-labeled oxidized carbon materials. Firstly, fluorescein-labeled oxidized carbon materials, OCS_{FLU}, OCT_{FLU} and OGSh_{FLU}, were mixed with liposomes consisting of 1,2-dioleoyl-*sn*-glycero-3-phosphatidylcholine (DOPC), which is a liquid disordered phase (Ld). Then, the mixed suspension was observed by mean of confocal laser fluorescence microscope (CLFM).

Figure 4.10 illustrates fluorescence intensity of the fluorescein-labeled oxidized carbon materials, (a) OCS_{FLU} , (b) OCT_{FLU} and (c) OGSh_{FLU} , on lipid bilayer membrane. It is clearly seen that the fluorescence intensity of OCS_{FLU} is obviously high around liposome's surface as compared with the others, suggesting that OCS_{FLU} possess higher ability to associate with the membrane than the others. OCT_{FLU} show partially association and no adhesion was observed for OGSh_{FLU} . In addition, the fluorescence signal could be observed inside only the liposomes which were mixed with OCS_{FLU} . This result implies that the OCS_{FLU} can penetrate through the lipid layer, and thus get inside the liposomes. Graphs on the left side of each image represent quantitative fluorescence intensity along the dash line of the corresponding image, acquired by the ImageJ software. The mechanism for penetration of OCSs through lipid bilayer membrane is thus proposed as follows: The OCSs associate well with lipid membrane and adsorption of phospholipid molecules onto their surface take place, resulting in transient pore formation around the area in which OCSs localized. The high level of membrane association for OCSs can be described using theory of membrane curvature. Adhesion of matter on membrane surface results in membrane deformation. The membrane will curve in order to wrap up the particulate which adheres on the membrane surface, allowing decrease in free energy of membrane adhesion. In this study, OGShs, the sheet shape oxidized carbon particle, possess geometric morphology with sharp edges and corners. So, it seems to be difficult for the membrane to wrap around this types of particle (due to abrupt curvature, Figure 4.11), resulting in high level of free energy and non-preferable adhesion of the OGShs on the membrane. On the other hand, OCSs possess more symmetry and round shape with no sharp edge. So, the free energy of OCS-membrane adhesion should be lower, allowing the more preferable association with lipid membrane than OCTs and OGShs (Figure 4.11). Comparing between OCT and OGSh, the latter is bigger than the former. Its bigger size together with no straight surface to make proper contact with membrane, probably make the OGSh shape particles the worst in association with the membrane.

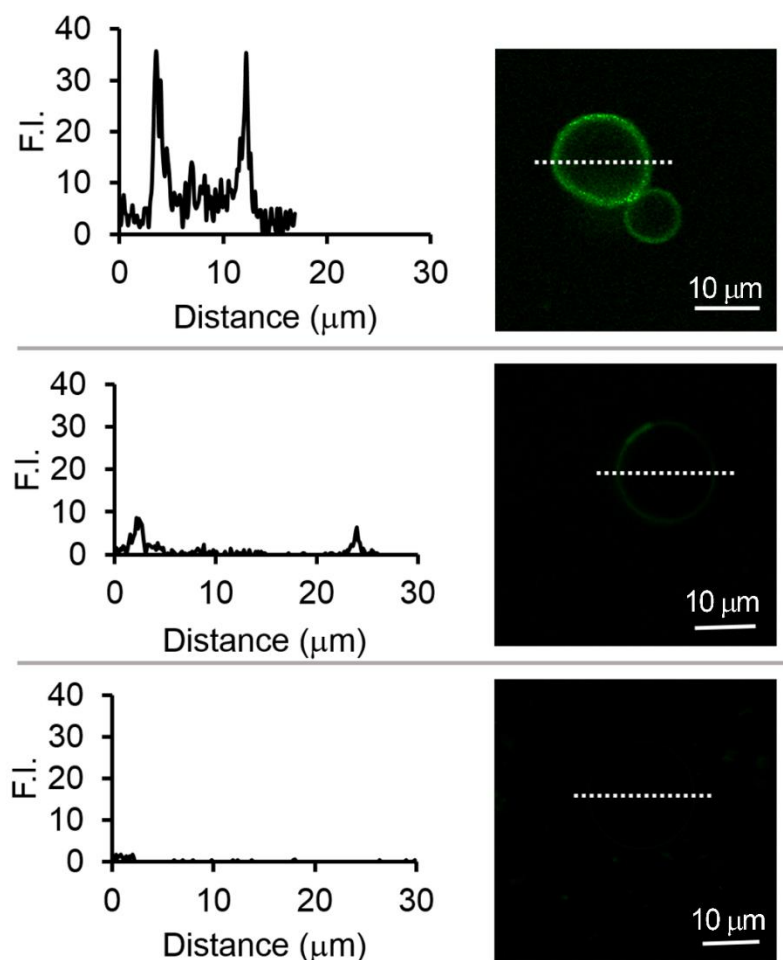


Figure 4.10 Association of OCSsFlu (top), OCTsFlu (middle) and OGShsFlu (bottom) with Ld liposomes at 30 min after mixing. The graphs shown on the left represent fluorescence intensity along the white dash line of each corresponding image obtained from ImageJ software.

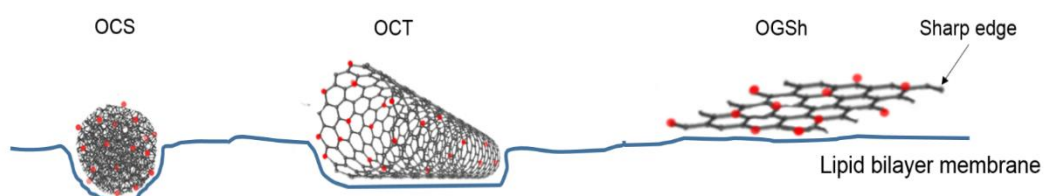


Figure 4.11 Schematic illustration of membrane association of OCS, OCT and OGSh.

The transient pore formation on the membrane induced by OCSs was further confirmed by dye leakage experiment. Ld liposomes filled with anthocyanin were incubated with OCSs and the mixture was observed by CLFM as a function of the incubation time, *i.e.*, 0, 30, 60 and 120 min. As shown in Figure 4.12, the anthocyanin-filled liposomes without OCSs (top row) shows the fluorescent signal of anthocyanin only in the liposome's interior, which means that all the anthocyanin remained inside the liposome. In the case of anthocyanin-filled liposome with the presence of OCSs, the anthocyanin signal could be detected at the outside of the liposomes immediately after the introduction of OCSs into the liposome suspension. The intensity becomes obvious after 30 min incubation time. At the same time, the fluorescent signal inside liposome decreased with the incubation time. Furthermore, the liposome morphology became distort after 120 min incubation time. This result suggests that the presence of OCSs induces the leakage of anthocyanin from the liposome's interior, probably through the transient pore formation.

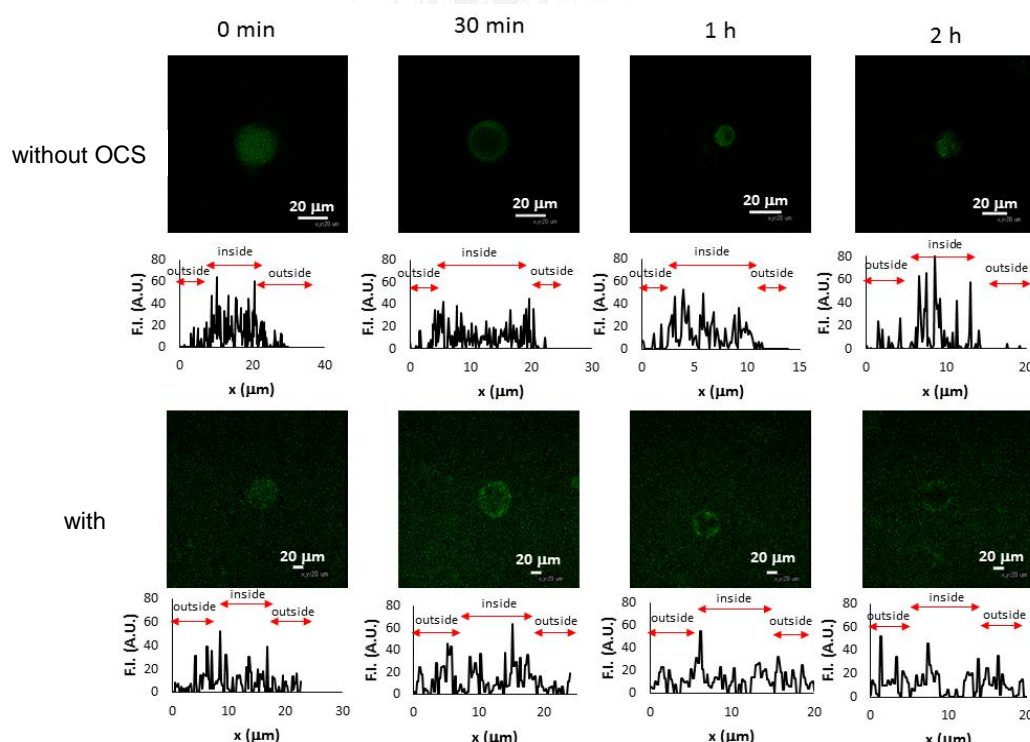


Figure 4.12 Anthocyanin leakage from the anthocyanin-filled liposome without (top) and with (bottom) OCSs at various incubation times, *i.e.*, 0, 30, 60 and 120 min.

4.3.2 Effect of Lipid Compositions of liposomes and Surface Functional Group of Oxidized Carbon

Then, the effect of lipid composition and surface functional group of OCSs on the particle-membrane interaction were investigated. Two types of liposome, liquid disordered liposomes (Ld) consisting of 1,2-dioleoyl-*sn*-glycero-3-phosphatidylcholine and liquid order liposomes (Lo) consisting of 1,2-dipalmitoyl-*sn*-glycero-3-phosphatidylcholine and cholesterol, were prepared. Next, OCS_{S_{FLU}} and mPEO-OCS_{S_{FLU}} were mixed with both Ld and Lo liposomes prior to the observation by CLFM. The result in Figure 4.13 indicates that both OCS_{S_{FLU}} and mPEO-OCS_{S_{FLU}} prefer to adhere on the Ld liposomes (Figure 4.13a) rather than the Lo liposomes (Figure 4.13c). This phenomenon can be explained based on membrane fluidity. Since the Ld membrane possesses high fluidity compared with the Lo membrane, the free energy of membrane curvature is, lower than that of the Lo membrane. Consequently, the Ld membrane is more flexible and able to curve around the particle's surface more easily. High association of OCSs on liposome surface makes the higher penetration of OCSs into the inside of the liposomes.

In addition, an ability of OCS_{S_{FLU}} and mPEO-OCS_{S_{FLU}} to adhere on the membrane surface was evaluated. As a result, OCS_{S_{FLU}} exhibit higher level of membrane association (Figure 4.13a and c), than that of mPEO-OCS_{S_{FLU}} (Figure 4.13b and d). This phenomenon could be observed when using both Ld and Lo membrane. This result suggests that surface functionality of the particles plays a significant role on the particle-membrane association. The modification of the OCSs' surface by mPEG reduces the surface activity of the OCSs. Therefore, the membrane adhesion, and also penetration ability of the mPEO-OCSs decreases as compared to the pristine OCSs.

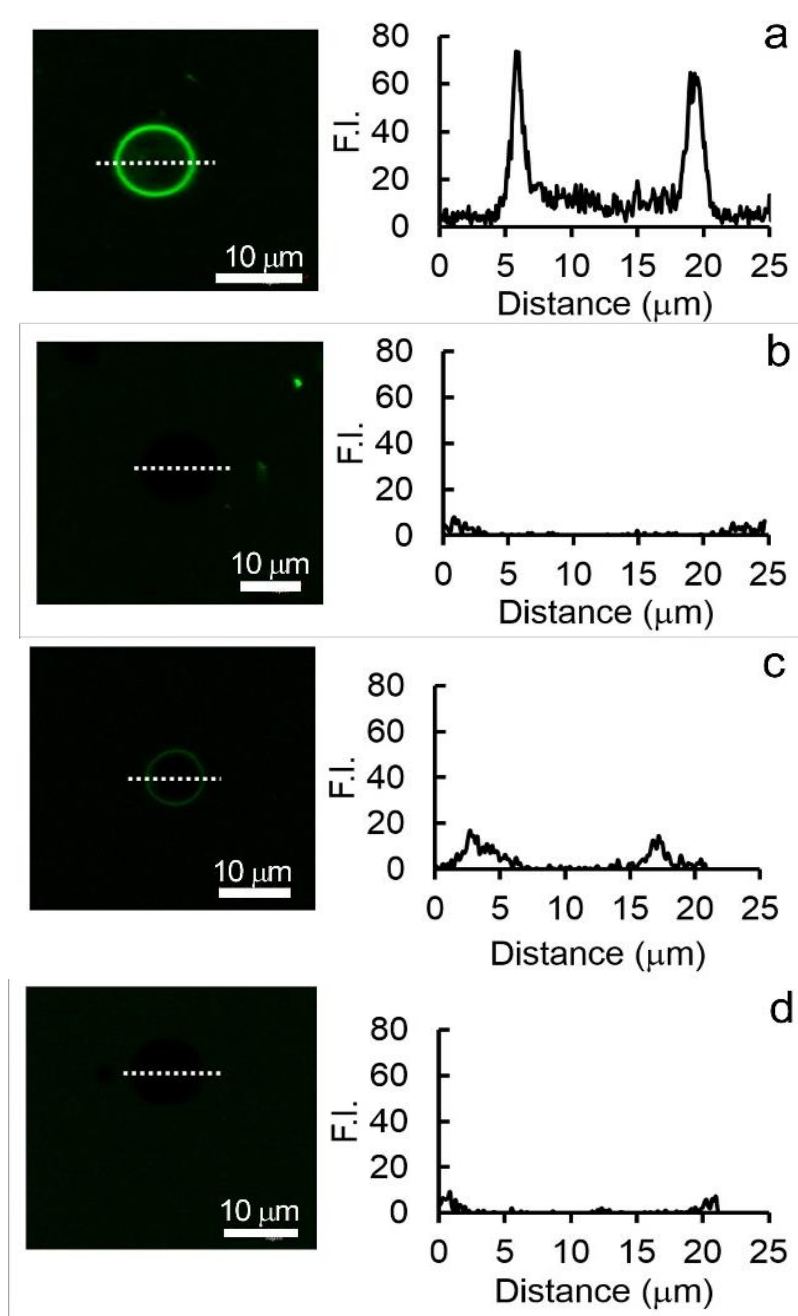


Figure 4.13 Association of OCS_{Flu} (a and b) and $\text{mPEO-OCS}_{\text{Flu}}$ (c and d) with Ld (a and c) and Lo (b and d) membranes after the incubation time of 30 min. Plots showing fluorescence intensity (F.I.) along the white dotted line of each image are shown next to the images.

The adhesion on the membrane surface and also the penetration through the membrane of OCS were further confirmed using BODIPY-labeled Ld liposomes and

OCS_{S_{Rho}}. Figure 4.14 shows fluorescent signal of BODIPY-labeled Ld liposome (top row) and BODIPY-labeled Ld liposome in the presence of OCS_{S_{Rho}} (bottom row). Column a represents BODIPY fluorescent signal, whereas the rhodamine fluorescent signal and differential interference contrast (DIC) image are shown in column b and c, respectively. As seen in the figure, the signal of rhodamine (covalently linked with OCSs) is clearly observed both on liposome's surface and inside as shown in the column b (bottom). This result strongly confirms that OCS possesses high ability to associate with membrane surface and eventually penetrate through the membrane.

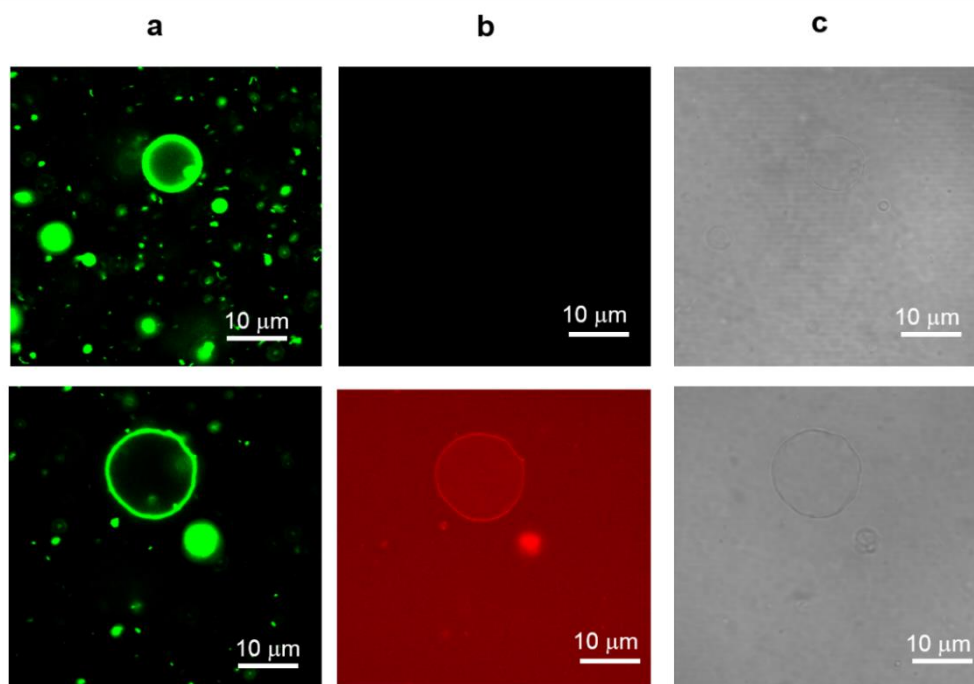


Figure 4.14 Association of OCS_{S_{Rho}} with BODIPY-labeled Ld liposome (bottom) compared to BODIPY-labeled Ld liposome without OCS_{S_{Rho}} (top) at the incubation time of 30 min. (a) BODIPY-labeled Ld liposome, (b) OCS_{S_{Rho}} and (c) DIC images.

4.3.3 Effect of Incubation Time

In the previous section, OCS is found to possess ability to adhere on the membrane surface and eventually, penetrate through the lipid bilayer. Therefore, the

effect of incubation time has to be considered. In this section, OCS_{Rho} were used to elucidate the particle-membrane association as a function of incubation time. The experiment was performed at 0, 1, 2, 3 and 4 h after mixing and the results are shown in Figure 4.15. The result indicates that OCS_{Rho} adhere on the membrane surface immediately after mixing (0 h). After 1 h incubation, the OCS_{Rho} completely penetrated into the liposome's interior and remained inside the liposome during the 4 h incubation. In the case of a liposome having multilayer, the penetration of OCS_{Rho} seems to occur only through the first layer of liposome as shown in Figure 4.16. Even though after 4 h incubation, there was no OCS_{Rho} inside the second layer of the liposomes. This phenomenon can be attributed to a decrease in surface activity of the OCS during their first layer penetration. It was likely that the particles adsorbed some lipid molecules onto their surface, leading to generation of the transient pore. Consequently, the lipid-coated OCSs were unable to adsorb more lipid molecules of the next layer, resulting in no transient pore formation and thus, no penetration through the second layer.

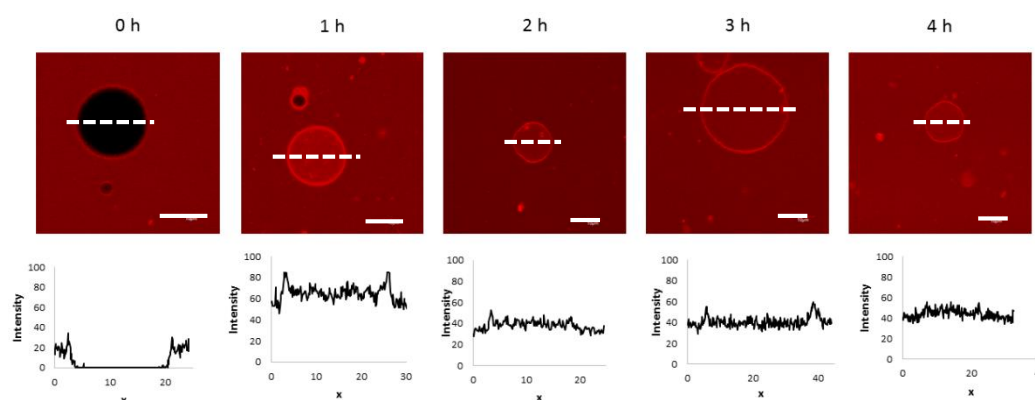


Figure 4.15 Association of OCS_{Rho} with Ld as a function of incubation time. The graphs below each corresponding image represent quantitative fluorescence intensity along the white dash line. Scale bars = 10 μm .

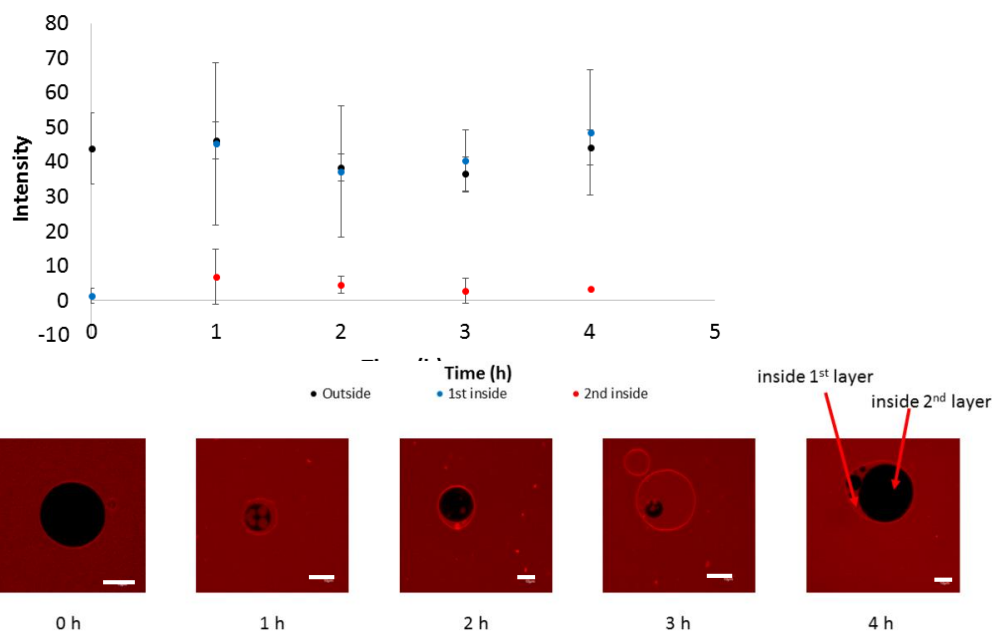


Figure 4.16 Fluorescence intensity of OCSRho outside, inside the first and second layer of liposome as a function of incubation time. Scale bars = 10 μm .

The decrease of surface activity of the OCS due to the adsorption of lipid molecules was further confirmed. The experiment was set up to observe the interaction between lipid-loaded OCS_{Rho} and Ld liposome. That is the phenomenon that the OCSs lose their surface activity by the adsorption of lipid was mimic. Ld membrane consisting of DOPC was prepared. In addition, the DOPC lipid was also loaded on the OCS_{Rho}'s surface. Then, the association of DOPC-loaded OCS_{Rho} on the Ld membrane was observed. Figure 4.17 shows the adhesion of OCS_{Rho} and the lipid-loaded OCS_{Rho} on the Ld membrane. As seen in the figure, OCS_{Rho} without DOPC loading could adhere and penetrate into the membrane effectively. After being loaded with DOPC, the ability of OCS_{Rho} to adhere and also, penetrate through the membrane significantly decreased. This agrees well with our hypothesis which is that the lower membrane penetration ability of OCSs (at the second layer in the liposome) is caused by lipid adsorption on liposome surface. The result also supports the hypothesis that the OCS can make transient pore on membrane through lipid adsorption.

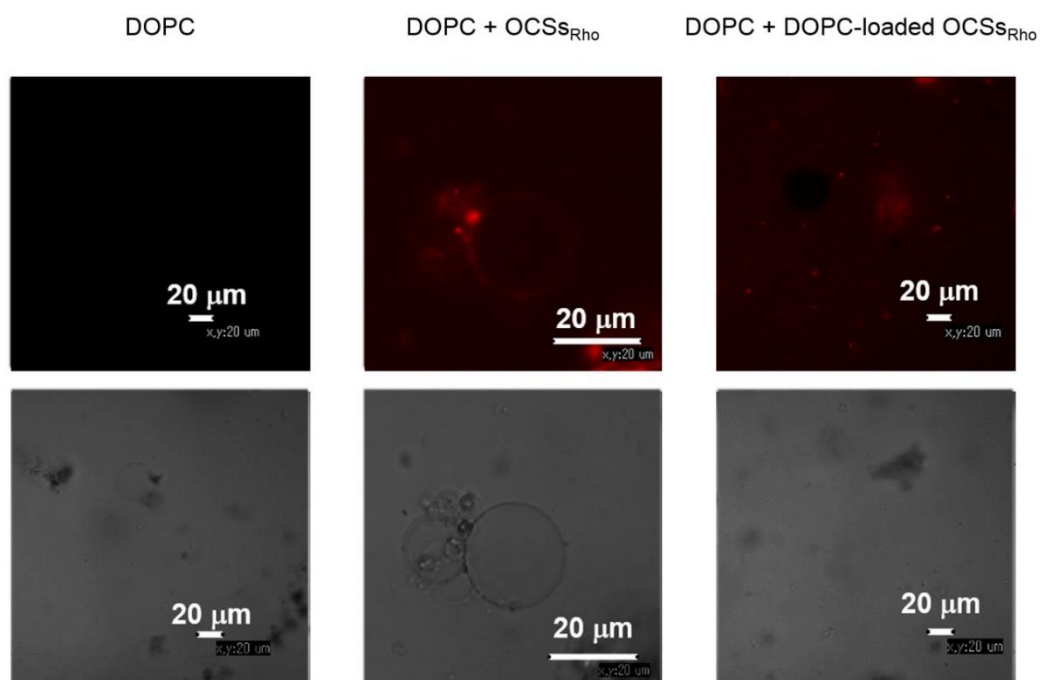


Figure 4.17 Association of OCSs_{Rho} and DOPC-loaded OCSs_{Rho} on the Ld membrane. The images were obtained with fluorescence mode (top) and DIC mode (bottom).

4.3.4 Effect of Cargo

Curcumin-loaded OCSs_{Rho} were studied in order to study the adhesion of OCSs on lipid bilayer membrane when some cargoes are loaded on the OCSs. In this experiment, Ld liposome, in which OCSs show high adhesion, was used. The OCSs_{Rho} were firstly loaded with curcumin at loading of 33 %. As seen in Figure 4.18, the fluorescent signal of rhodamine, which was attached on the OCSs' surface, could be detected both on the liposome's surface and the liposome's interior. In addition, the curcumin signal appears on the surface and also in the liposome interior. This result suggests that even with loading of some cargo, OCSs_{Rho} still show the association with lipid membrane. We speculate that the cargo-loaded OCSs still can adsorb some lipids, so membrane penetration could still take place. This may be a result of strong interaction of lipid molecules and OCSs.

The result here is slightly different from the PEO modification since curcumin is a small organic molecule comparing to long chain PEO. In particular, PEO chain can swell in aqueous and become a corona around OCS particles. This reduces surface activity of the OCS.

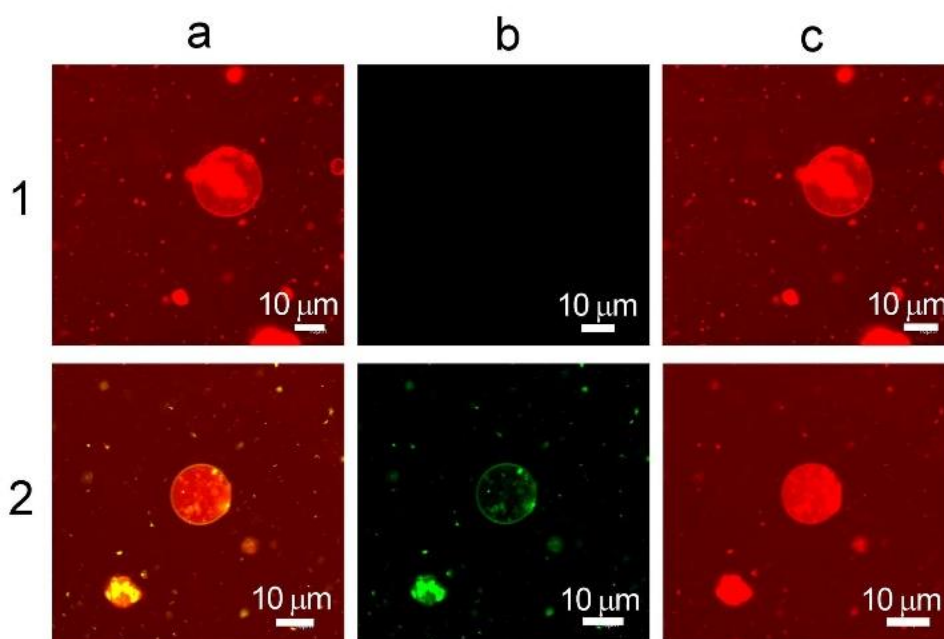


Figure 4.18 Interaction of OCSs_{Rho} (150 ppm) and curcumin-loaded OCSs_{Rho} (75 ppm curcumin, 150 ppm OCSs_{Rho}) with cell-sized liposomes (0.1 mM of the DOPC). Fluorescence images of the Ld liposomes after 30 min incubation with OCSs_{Rho} (row 1) and curcumin-loaded OCSs_{Rho} (row 2): shown as the merged images of both curcumin fluorescence and OCS_{Rho} fluorescence (column a), only curcumin signal (green, column b), and OCS_{Rho} signal (red, column c).

4.3.5 Effect of pH

Next, pH-dependence of OCS surface activity was evaluated. The adsorption of lipid molecules on the OCS' surface at pH 7.4 and 5.5 was investigated. The result in Figure 4.19 shows the amount of un-adsorbed fluorescence-labeled lipid, DMPE-RhB, extracted from the OCSs by centrifugal filtration. This result indicates that OCSs could adsorb lipids at both pH conditions as compared with control (no OCSs), but the

adsorption level at pH 5.5 is approximately two times higher than that at pH 7.4. It could be implied that the surface of OCS is more active in the slight acidic condition.

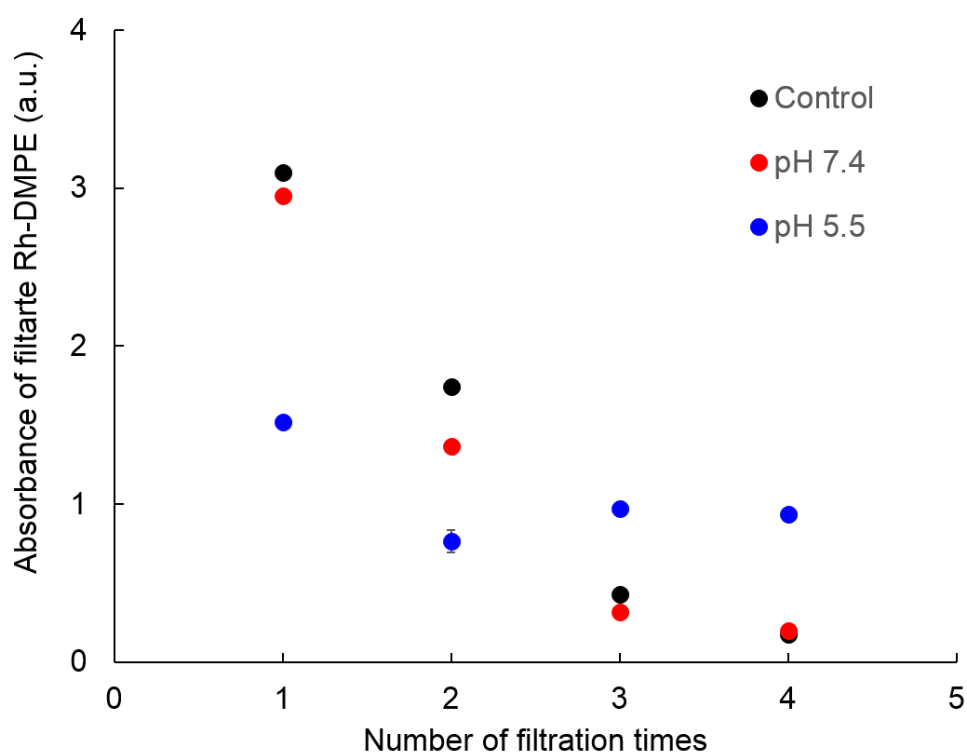


Figure 4.19 Amount of un-adsorbed DMPE-RhB as a function of filtration time at pH 7.4 (red) and 5.5 (blue) compared with control (no OCSs, black).

4.4 Cytotoxicity of Oxidized Carbon Materials

Toxicity of the oxidized carbon materials was investigated against adenocarcinomic human alveolar basal epithelial (A549) cells and the cells resistant to etoposide (A549RT-eto), which is the multidrug resistance (MDR) cells, identified by an overexpression of P-glycoprotein (P-gp). OCS, OCT, OGSh, mPEO-OCS, mPEO-OCT, and mPEO-OGSh suspension at various concentrations, 0.001, 0.01, 0.1, 1 and 10 $\mu\text{g}/\text{mL}$, were used to treat the cells. Both A459 and A549RT-eto were incubated with the samples for 72 h. Figure 4.20 shows cell viability (%) at various concentrations of

the oxidized carbon materials. Column a shows the cytotoxicity of OCS, OCT and OGSh, whereas column b represents the cytotoxicity of mPEO-OCS, mPEO-OCT and mPEO-OGSh. Toxicity of the oxidized carbon materials both with and without PEO modification are similar. The percentage of cell viability is higher than 80 % for the material concentration range of 0.001 to 1 $\mu\text{g/mL}$. In addition, the cell viability is above 50 % for the whole range of the tested concentrations. This implies that the oxidized carbon materials has no/little toxicity to both A549 and A549RT-eto cell lines. Furthermore, modification with PEO does not affect toxicity of the materials.

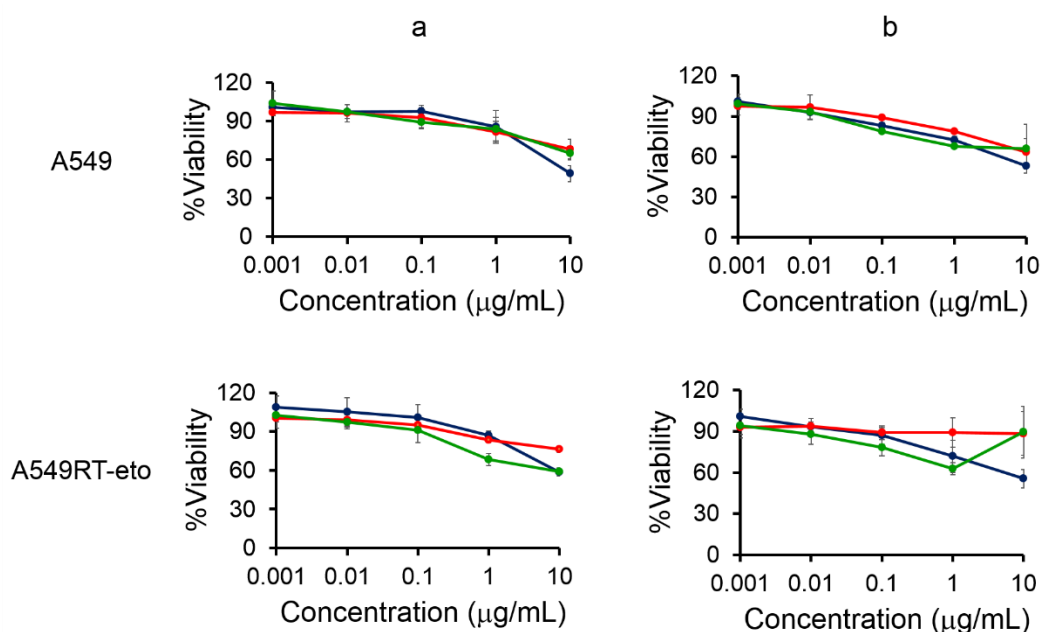


Figure 4.20 Cytotoxicity of (column a): OCS (blue), OCT (red) and OGSh (green) and (column b): mPEO-OCS (blue), mPEO-OCT (red) and mPEO-OGSh (green) against A549 and A549RT-eto cell lines at the incubation time of 72 h.

4.5 Cellular Uptake of Curcumin-loaded Oxidized Carbon Materials

The intracellular uptake of all materials was evaluated against A549 cell line. In this experiment, curcumin was used as a cargo, whereas rhodamine-labeled oxidized carbon materials, OCS_{Rho} , OCT_{Rho} , OGSh_{Rho} , $\text{mPEO-OCS}_{\text{Rho}}$, $\text{mPEO-OCT}_{\text{Rho}}$ and $\text{mPEO-OGSh}_{\text{Rho}}$, were used as carriers. The cells were treated with the oxidized carbon

materials having the concentration of 10 $\mu\text{g/mL}$ for 4 h prior to observation by CLFM with DIC and fluorescence modes. The excitation and emission wavelengths are as follows; $\lambda_{\text{ex}}/\lambda_{\text{em}} = 405/450$ nm (blue), 488/525 nm (green) and 561/595 nm (red). As shown in Figure 4.21, column a represents DIC image of A549 cell, whereas column b, c and d show the signal of nucleus staining with Hoechst, curcumin and rhodamine-labeled oxidized carbon materials. The result reveals that curcumin delivered by OCSs could be uptaken into the cells with the highest level, whereas OCTs could moderate deliver curcumin into cells, and OGShs could rarely deliver any curcumin into the cells at all. In addition, OCSs and curcumin signals could be detected in both cytosol and nucleus, indicating the the OCSs are able to bring curcumin into cytosol and nucleus of the cells. In the case of the delivery by OCTs, both curcumin and rhodamine (covalently linked with particles) signals appears only in cytoplasm. On the contrary, OGShs could rarely be uptaken into the cells. Therefore, delivery of curcumin by OGShs could not be achieved. In addition, modification of PEO seems to reduce the uptake ability because both curcumin and rhodamine signals drop down for the PEO-modified carriers. The uptake ability of oxidized carbon particulates into the cells strongly corresponds to the result from the above liposome experiments.

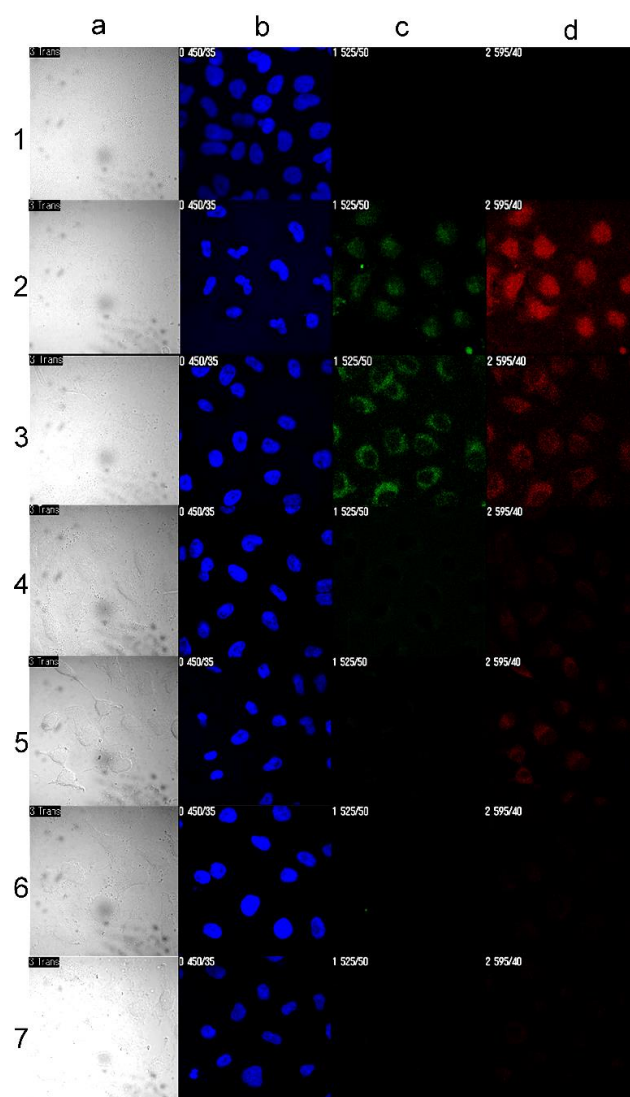


Figure 4.21 Delivery of curcumin into A549 cells by rhodamine-labeled oxidized carbon materials: control cells (row 1), cells incubated with curcumin-loaded OCS_{Rho} (row 2), curcumin-loaded OCT_{Rho} (row 3), curcumin-loaded OGSh_{Rho} (row 4), curcumin-loaded mPEO-OCS_{Rho} (row 5), curcumin-loaded mPEO-OCT_{Rho} (row 6), curcumin-loaded mPEO-OGS_{Rho} (row 7). Column a shows image in DIC mode, Column b-d represents the fluorescence mode showing the fluorescence signals from nucleus staining with Hoechst (blue, b), curcumin (green, c) and rhodamine-labeled oxidized carbon materials (red, d). The concentration of oxidized carbon materials was controlled at 10 $\mu\text{g/mL}$ with the incubation time of 4 h.

4.6 Anti-cancer Activity

OCSs were used to deliver hydrophobic (paclitaxel) and hydrophilic (doxorubicin) anti-cancer drugs into A549 and A549RT-eto cells. The drugs were loaded on the OCSs' surface with the loading efficiency of 6.3 %. Then, anti-cancer activity was evaluated compared with free drugs. Figure 4.22 shows cell viability (%) after being treated with OCSs, free PTX, PTX-loaded OCSs, free DOX and DOX-loaded OCSs for 72 h. As seen in the result, delivery of PTX and DOX by OCSs exhibit same level of anti-cancer activity compared to the free drug with the OCS concentration exceeds 1 $\mu\text{g/mL}$ for both A459 and A549Rt-eto cell lines. For A549Rt-eto cell lines, the delivery of PTX by OCSs, however, shows significantly high anti-cancer activity as compared to that of free PTX in DMSO at the OCS concentration of 10 $\mu\text{g/mL}$. In the case of DOX, it is partially soluble in water and able to be effectively uptaken into cell with no need of delivery system. Therefore, the OCS carrier could not efficiently increase DOX activity. The particles seems to decrease DOX activity. This is likely a result of drug adsorption on the particles.

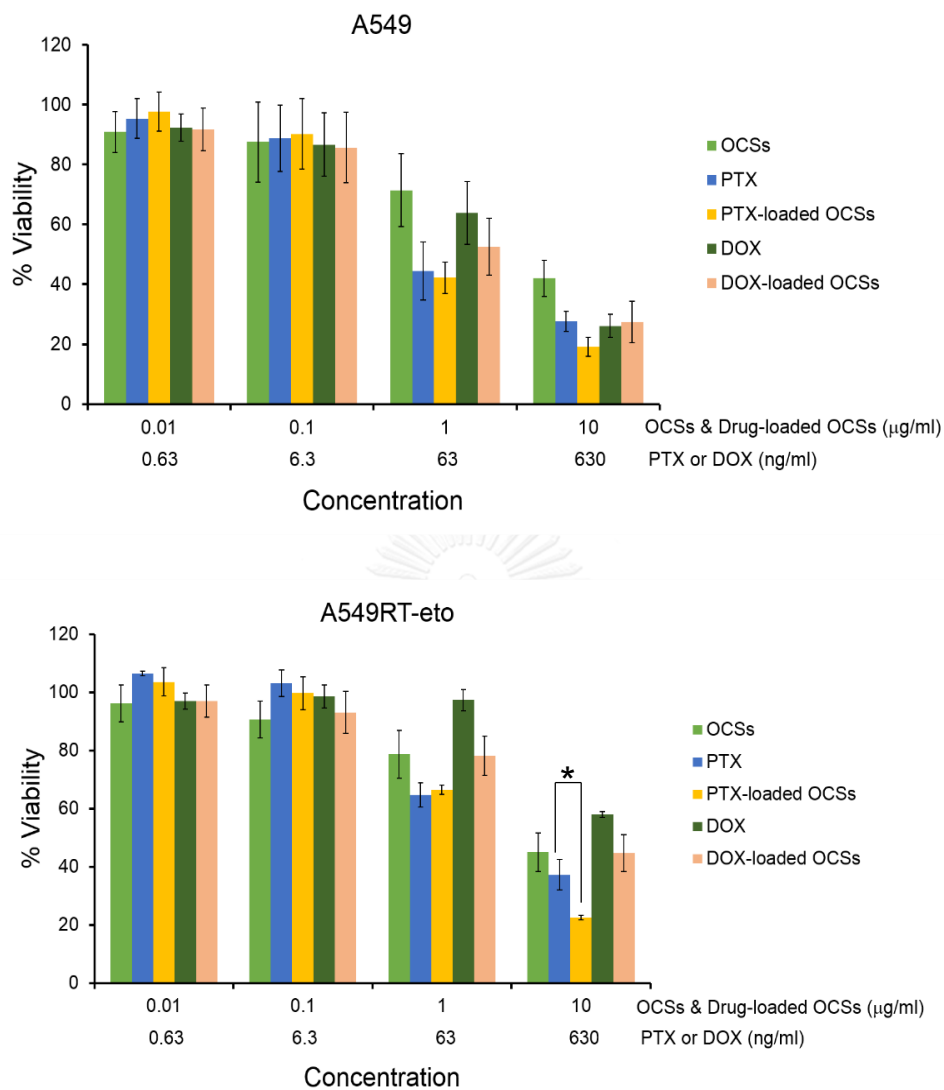


Figure 4.22 Anti-cancer activity against A549 (top) and A549RT-eto (bottom) cell lines of OCSs, PTX, PTX-loaded OCSs, DOX and DOX-loaded OCSs with various concentrations. Incubation time was 72 h. Statistical significant difference was calculated using one-way ANOVA (* $p < 0.01$).

CHAPTER V

CONCLUSION

In this research, oxidized carbon particulates having various morphologies were used as drug carrier. I have prepared three different shaped oxidized carbon particulates: 1) cluster of carbon nanosphere, or the so called oxidized carbon nanosphere (OCS), which is a spherical oxidized carbon particle with the diameter of 100-200 nm, 2) oxidized carbon nanotube (OCT), a tubular oxidized carbon particulate with an aspect ratio of 10, and 3) oxidized graphene sheet (OGSh) which is a sheet shape oxidized carbon particulate with the dimension of 0.5 x 0.5 μm . Interaction with lipid bilayer membrane was investigated using cell-sized liposome. Among the three shaped particulates, the OCSs showed highest ability to associate with lipid bilayer membrane, and the highest ability to penetrate into the liposomes' interior. The penetration of OCS across the lipid bilayer membrane occurred through the transient pore formation mechanism. OCTs possess a moderate adhesion to lipid bilayer membrane but showed no penetration across the membrane. OGShs exhibit no adhesion. These results can be explained based on membrane curvature theory. Since spherical shape contains no edge and corner, its adhesion to membrane allowed smooth membrane curvature with low free energy of particle-membrane association, leading to the preferable adhesion. Furthermore, the OCSs were found to more preferably adhere on liquid-disordered phase (Ld) liposomes as compared to the liquid-ordered phase (Lo). Surface functionalization of the OCSs by mPEG was found to reduce their ability to associate with lipid bilayer membrane. Loading of the cargo, *i.e.*, curcumin, on the OCSs did not decrease the ability of the particles to associate with the membrane. OCSs could deliver curcumin into the interior of the Ld liposomes. OCSs surface activity was found to be more active in acidic condition than in the neutral pH. Among the three shaped oxidized carbon particulates, OCSs showed the highest efficiency in delivering curcumin into the A549 lung cancer cells, and curcumin and OCSs accumulated in both cytoplasm and nucleus of the cells. This phenomenon could not be observed when using OCTs and OGShs. In the case of OCTs, curcumin

could be delivered only into the cytosol, whereas no curcumin existed in the cells when delivered by OGSs. In addition, delivery of the hydrophobic anti-cancer drug into A549 human lung cancer cells by OCSs resulted in the same anti-cancer activity as when the drug was used as solution in organic solvent.



REFERENCES

- [1] Bertrand, N. and Leroux, J.-C. The journey of a drug-carrier in the body: An anatomo-physiological perspective. Journal of Controlled Release 161(2) (2012): 152-163.
- [2] Casanovas, O. Cancer: Limitations of therapies exposed. Nature 484(7392) (2012): 44-46.
- [3] Bråve, A., Ljungberg, K., Wahren, B., and Liu, M.A. Vaccine delivery methods using viral vectors. Molecular Pharmaceutics 4(1) (2007): 18-32.
- [4] Kanintronkul, Y., et al. Overcoming multidrug resistance in human lung cancer with novel benzo[a]quinolizin-4-ones. Anticancer Research 31(3) (2011): 921-7.
- [5] Zhang, W., Guo, Z., Huang, D., Liu, Z., Guo, X., and Zhong, H. Synergistic effect of chemo-photothermal therapy using pegylated graphene oxide. Biomaterials 32(33) (2011): 8555-8561.
- [6] Gao, Z., Zhang, L., and Sun, Y. Nanotechnology applied to overcome tumor drug resistance. Journal of Controlled Release 162(1) (2012): 45-55.
- [7] Li, P., Nielsen, H.M., and Müllertz, A. Impact of lipid-based drug delivery systems on the transport and uptake of insulin across Caco-2 cell monolayers. Journal of Pharmaceutical Sciences (2016): 1-9.
- [8] Sönke, S. Carrier-based drug delivery. in Carrier-based drug delivery, pp. 2-23: American Chemical Society, 2004.
- [9] Sahoo, S.K., Jain, T.K., Reddy, M.K., and Labhasetwar, V. Nano-sized carriers for drug delivery. in Shoseyov, O. and Levy, I. (eds.), Nanobiotechnology: Bioinspired devices and materials of the future, pp. 329-348. Totowa, NJ: Humana Press, 2008.
- [10] Martín del Valle, E.M., Galán, M.A., and Carbonell, R.G. Drug delivery technologies: The way forward in the new decade. Industrial & Engineering Chemistry Research 48(5) (2009): 2475-2486.

- [11] Zhang, Y., Ali, S.F., Dervishi, E., Xu, Y., Li, Z., Casciano, D., and Biris, A.S. Cytotoxicity effects of graphene and single-wall carbon nanotubes in neural pheochromocytoma-derived PC12 cells. ACS Nano 4(6) (2010): 3181-3186.
- [12] Ghosh Chaudhuri, R. and Paria, S. Core/shell nanoparticles: Classes, properties, synthesis mechanisms, characterization, and applications. Chemical Reviews 112(4) (2011): 2373-2433.
- [13] Carbon nanotubes in cancer therapy and drug delivery. Journal of Drug Delivery 2012 (2012).
- [14] Chertok, B., Webber, M.J., Succi, M.D., and Langer, R. Drug delivery interfaces in the 21st Century: From science fiction ideas to viable technologies. Molecular Pharmaceutics 10(10) (2013): 3531-3543.
- [15] Dinauer, N., Balthasar, S., Weber, C., Kreuter, J., Langer, K., and von Briesen, H. Selective targeting of antibody-conjugated nanoparticles to leukemic cells and primary T-lymphocytes. Biomaterials 26(29) (2005): 5898-5906.
- [16] Yang, X., et al. Folate-encoded and fe₃o₄-loaded polymeric micelles for dual targeting of cancer cells. Polymer 49(16) (2008): 3477-3485.
- [17] Casi, G. and Neri, D. Antibody–drug conjugates: Basic concepts, examples and future perspectives. Journal of Controlled Release 161(2) (2012): 422-428.
- [18] Lammers, T., Kiessling, F., Hennink, W.E., and Storm, G. Drug targeting to tumors: Principles, pitfalls and (pre-) clinical progress. Journal of Controlled Release 161(2) (2012): 175-187.
- [19] Mahon, E., Salvati, A., Baldelli Bombelli, F., Lynch, I., and Dawson, K.A. Designing the nanoparticle–biomolecule interface for “targeting and therapeutic delivery”. Journal of Controlled Release 161(2) (2012): 164-174.
- [20] Poelstra, K., Prakash, J., and Beljaars, L. Drug targeting to the diseased liver. Journal of Controlled Release 161(2) (2012): 188-197.
- [21] An, X., Zhan, F., and Zhu, Y. Smart photothermal-triggered bilayer phase transition in AuNPs–liposomes to release drug. Langmuir 29(4) (2013): 1061-1068.
- [22] Eloy, J.O., Claro de Souza, M., Petrilli, R., Barcellos, J.P.A., Lee, R.J., and Marchetti, J.M. Liposomes as carriers of hydrophilic small molecule drugs:

- Strategies to enhance encapsulation and delivery. Colloids and Surfaces B: Biointerfaces 123 (2014): 345-363.
- [23] Cai, K., et al. Dimeric drug polymeric nanoparticles with exceptionally high drug loading and quantitative loading efficiency. Journal of the American Chemical Society 137(10) (2015): 3458-3461.
- [24] Cosco, D., et al. Ultradeformable liposomes as multidrug carrier of resveratrol and 5-fluorouracil for their topical delivery. International Journal of Pharmaceutics 489(1-2) (2015): 1-10.
- [25] Chariou, P.L., Lee, K.L., Pokorski, J.K., Saidel, G.M., and Steinmetz, N.F. Diffusion and uptake of tobacco mosaic virus as therapeutic carrier in tumor tissue: Effect of nanoparticle aspect ratio. The Journal of Physical Chemistry B (2016): doi: 10.1021/acs.jpccb.6b02163.
- [26] Janas, C., Mostaphaoui, Z., Schmiederer, L., Bauer, J., and Wacker, M.G. Novel polymeric micelles for drug delivery: Material characterization and formulation screening. International Journal of Pharmaceutics 509(1-2) (2016): 197-207.
- [27] Koren, E. and Torchilin, V.P. Cell-penetrating peptides: Breaking through to the other side. Trends in Molecular Medicine 18(7): 385-393.
- [28] Haeri, A., Zalba, S., ten Hagen, T.L.M., Dadashzadeh, S., and Koning, G.A. EGFR targeted thermosensitive liposomes: A novel multifunctional platform for simultaneous tumor targeted and stimulus responsive drug delivery. Colloids and Surfaces B: Biointerfaces (2016): doi:10.1016/j.colsurfb.2016.06.012.
- [29] Nasongkla, N., et al. Multifunctional polymeric micelles as cancer-targeted, mri-ultrasensitive drug delivery systems. Nano Letters 6(11) (2006): 2427-2430.
- [30] Ma, L.L., et al. Small multifunctional nanoclusters (nanoroses) for targeted cellular imaging and therapy. ACS Nano 3(9) (2009): 2686-2696.
- [31] Yang, X., et al. Multi-functionalized graphene oxide based anticancer drug-carrier with dual-targeting function and ph-sensitivity. Journal of Materials Chemistry 21(10) (2011): 3448-3454.
- [32] Ajima, K., Yudasaka, M., Murakami, T., Maigné, A., Shiba, K., and Iijima, S. Carbon nanohorns as anticancer drug carriers. Molecular Pharmaceutics 2(6) (2005): 475-480.

- [33] Sun, X., et al. Nano-graphene oxide for cellular imaging and drug delivery. Nano Research 1(3) (2008): 203-212.
- [34] Bottini, M., Rosato, N., and Bottini, N. Peg-modified carbon nanotubes in biomedicine: Current status and challenges ahead. Biomacromolecules 12(10) (2011): 3381-3393.
- [35] Kim, H., Namgung, R., Singha, K., Oh, I.-K., and Kim, W.J. Graphene oxide–polyethylenimine nanoconstruct as a gene delivery vector and bioimaging tool. Bioconjugate Chemistry 22(12) (2011): 2558-2567.
- [36] Liao, K.-H., Lin, Y.-S., Macosko, C.W., and Haynes, C.L. Cytotoxicity of graphene oxide and graphene in human erythrocytes and skin fibroblasts. ACS Applied Materials & Interfaces 3(7) (2011): 2607-2615.
- [37] Arayachukeat, S., Palaga, T., and Wanichwecharungruang, S.P. Clusters of carbon nanospheres derived from graphene oxide. ACS Applied Materials & Interfaces 4(12) (2012): 6808-6815.
- [38] Grazú, V., Moros, M., and Sánchez-Espinel, C. Chapter 14 - nanocarriers as nanomedicines: Design concepts and recent advances. in Jesus, M.d.l.F. and Grazu, V. (eds.), Frontiers of nanoscience, pp. 337-440: Elsevier, 2012.
- [39] Chan, H.-K. Dry powder aerosol drug delivery—opportunities for colloid and surface scientists. Colloids and Surfaces A: Physicochemical and Engineering Aspects 284–285 (2006): 50-55.
- [40] Langer, R. and Peppas, N.A. Advances in biomaterials, drug delivery, and bionanotechnology. AIChE Journal 49(12) (2003): 2990-3006.
- [41] Prausnitz, M.R., Mitragotri, S., and Langer, R. Current status and future potential of transdermal drug delivery. Nature Reviews Drug Discovery 3(2) (2004): 115-124.
- [42] Rehman, Z.u., Hoekstra, D., and Zuhorn, I.S. Mechanism of polyplex- and lipoplex-mediated delivery of nucleic acids: Real-time visualization of transient membrane destabilization without endosomal lysis. ACS Nano 7(5) (2013): 3767-3777.

- [43] Bell, P.C., et al. Transfection mediated by gemini surfactants: Engineered escape from the endosomal compartment. Journal of the American Chemical Society 125(6) (2003): 1551-1558.
- [44] Gupta, R., Shea, J., Scaife, C., Shurlygina, A., and Rapoport, N. Polymeric micelles and nanoemulsions as drug carriers: Therapeutic efficacy, toxicity, and drug resistance. Journal of Controlled Release 212 (2015): 70-77.
- [45] Kim, Y., Pourgholami, M.H., Morris, D.L., and Stenzel, M.H. Effect of cross-linking on the performance of micelles as drug delivery carriers: A cell uptake study. Biomacromolecules 13(3) (2012): 814-825.
- [46] Rapoport, N., Gupta, R., Kim, Y.-S., and O'Neill, B.E. Polymeric micelles and nanoemulsions as tumor-targeted drug carriers: Insight through intravital imaging. Journal of Controlled Release 206 (2015): 153-160.
- [47] Alexis, F., Pridgen, E., Molnar, L.K., and Farokhzad, O.C. Factors affecting the clearance and biodistribution of polymeric nanoparticles. Molecular Pharmaceutics 5(4) (2008): 505-515.
- [48] Lin, G., Zhang, H., and Huang, L. Smart polymeric nanoparticles for cancer gene delivery. Molecular Pharmaceutics 12(2) (2015): 314-321.
- [49] Zhou, H., et al. Synthesis and characterization of amphiphilic glycidol-chitosan-deoxycholic acid nanoparticles as a drug carrier for doxorubicin. Biomacromolecules 11(12) (2010): 3480-3486.
- [50] Wang, Y.-C., Wang, F., Sun, T.-M., and Wang, J. Redox-responsive nanoparticles from the single disulfide bond-bridged block copolymer as drug carriers for overcoming multidrug resistance in cancer cells. Bioconjugate Chemistry 22(10) (2011): 1939-1945.
- [51] Nasrolahi Shirazi, A., Mandal, D., Tiwari, R.K., Guo, L., Lu, W., and Parang, K. Cyclic peptide-capped gold nanoparticles as drug delivery systems. Molecular Pharmaceutics 10(2) (2013): 500-511.
- [52] Han, Y., et al. Highly uniform α -NaYF₄:Yb/Er hollow microspheres and their application as drug carrier. Inorganic Chemistry 52(16) (2013): 9184-9191.

- [53] Czapar, A.E., et al. Tobacco mosaic virus delivery of phenanthriplatin for cancer therapy. ACS Nano 10(4) (2016): 4119-4126.
- [54] Li, M., Jiang, Y., Gong, T., Zhang, Z., and Sun, X. Intranasal vaccination against HIV-1 with adenoviral vector-based nanocomplex using synthetic TLR-4 agonist peptide as adjuvant. Molecular Pharmaceutics 13(3) (2016): 885-894.
- [55] Everts, M., et al. Covalently linked au nanoparticles to a viral vector: Potential for combined photothermal and gene cancer therapy. Nano Letters 6(4) (2006): 587-591.
- [56] Roiter, Y., Ornatska, M., Rammohan, A.R., Balakrishnan, J., Heine, D.R., and Minko, S. Interaction of nanoparticles with lipid membrane. Nano Letters 8(3) (2008): 941-944.
- [57] Zhang, S., Li, J., Lykotrafitis, G., Bao, G., and Suresh, S. Size-dependent endocytosis of nanoparticles. Advanced Materials 21 (2009): 419-424.
- [58] Chen, K.L. and Bothun, G.D. Nanoparticles meet cell membranes: Probing nonspecific interactions using model membranes. Environmental Science & Technology 48(2) (2014): 873-880.
- [59] Khalil, I.A., Kogure, K., Akita, H., and Harashima, H. Uptake pathways and subsequent intracellular trafficking in nonviral gene delivery. Pharmacological Reviews 58(1) (2006): 32-45.
- [60] McMahon, H.T. and Boucrot, E. Molecular mechanism and physiological functions of clathrin-mediated endocytosis. Nature Reviews Molecular Cell Biology 12(8) (2011): 517-533.
- [61] Shang, L., Nienhaus, K., and Nienhaus, G.U. Engineered nanoparticles interacting with cells: Size matters. Journal of Nanobiotechnology 12(1) (2014): 1-11.
- [62] Oh, N. and Park, J.-H. Endocytosis and exocytosis of nanoparticles in mammalian cells. International Journal of Nanomedicine 9 (2014): 51-63.
- [63] Chithrani, B.D. and Chan, W.C.W. Elucidating the mechanism of cellular uptake and removal of protein-coated gold nanoparticles of different sizes and shapes. Nano Letters 7(6) (2007): 1542-1550.

- [64] Pelkmans, L. and Helenius, A. Endocytosis via caveolae. Traffic 3(5) (2002): 311-320.
- [65] Nabi, I.R. and Le, P.U. Caveolae/raft-dependent endocytosis. The Journal of Cell Biology 161(4) (2003): 673-677.
- [66] Pelkmans, L. Secrets of caveolae- and lipid raft-mediated endocytosis revealed by mammalian viruses. Biochimica et Biophysica Acta (BBA) - Molecular Cell Research 1746(3) (2005): 295-304.
- [67] Swanson, J.A. and Watts, C. Macropinocytosis. Trends in Cell Biology 5(11) (1995): 424-428.
- [68] Lim, J.P. and Gleeson, P.A. Macropinocytosis: An endocytic pathway for internalising large gulps. Immunology & Cell Biology 89(8) (2011): 836-843.
- [69] Sulheim, E. Mechanisms of cellular uptake and intracellular degradation of polymeric nanoparticles. Master Thesis, Norwegian University of Science and Technology, 2014.
- [70] Orsi, M. and Essex, J.W. Chapter 4 passive permeation across lipid bilayers: A literature review. in Molecular simulations and biomembranes: From biophysics to function, pp. 76-90: The Royal Society of Chemistry, 2010.
- [71] Varkouhi, A.K., Scholte, M., Storm, G., and Haisma, H.J. Endosomal escape pathways for delivery of biologicals. Journal of Controlled Release 151(3) (2011): 220-228.
- [72] Gujrati, M., Malamas, A., Shin, T., Jin, E., Sun, Y., and Lu, Z.-R. Multifunctional cationic lipid-based nanoparticles facilitate endosomal escape and reduction-triggered cytosolic siRNA release. Molecular Pharmaceutics 11(8) (2014): 2734-2744.
- [73] Cardarelli, F., Pozzi, D., Bifone, A., Marchini, C., and Caracciolo, G. Cholesterol-dependent macropinocytosis and endosomal escape control the transfection efficiency of lipoplexes in cho living cells. Molecular Pharmaceutics 9(2) (2012): 334-340.
- [74] Kobayashi, S., et al. Cytosolic targeting of macromolecules using a pH-dependent fusogenic peptide in combination with cationic liposomes. Bioconjugate Chemistry 20(5) (2009): 953-959.

- [75] Jayakumar, M.K.G., Bansal, A., Huang, K., Yao, R., Li, B.N., and Zhang, Y. Near-infrared-light-based nano-platform boosts endosomal escape and controls gene knockdown *in vivo*. ACS Nano 8(5) (2014): 4848-4858.
- [76] Kwon, Y.J. Before and after endosomal escape: Roles of stimuli-converting siRNA/polymer interactions in determining gene silencing efficiency. Accounts of Chemical Research 45(7) (2012): 1077-1088.
- [77] Zha, Z., Li, J., and Ge, Z. Endosomal-escape polymers based on multicomponent reaction-synthesized monomers integrating alkyl and imidazolyl moieties for efficient gene delivery. ACS Macro Letters 4(10) (2015): 1123-1127.
- [78] Belting, M., Sandgren, S., and Wittrup, A. Nuclear delivery of macromolecules: Barriers and carriers. Advanced Drug Delivery Reviews 57(4) (2005): 505-527.
- [79] Strunze, S., Trotman, L.C., Boucke, K., and Greber, U.F. Nuclear targeting of adenovirus type 2 requires crm1-mediated nuclear export. Molecular Biology of the Cell 16(6) (2005): 2999-3009.
- [80] Wagstaff, K.M. and Jans, D.A. Nuclear drug delivery to target tumour cells. European Journal of Pharmacology 625(1-3) (2009): 174-180.
- [81] Schultz, M., Olubummo, A., and Binder, W.H. Beyond the lipid-bilayer: Interaction of polymers and nanoparticles with membranes. Soft Matter 8(18) (2012): 4849-4864.
- [82] Shimoni, O., Yan, Y., Wang, Y., and Caruso, F. Shape-dependent cellular processing of polyelectrolyte capsules. ACS Nano 7(1) (2013): 522-530.
- [83] Tree-Udom, T., et al. Shape effect on particle-lipid bilayer membrane association, cellular uptake, and cytotoxicity. ACS Applied Materials & Interfaces 7(43) (2015): 23993-24000.
- [84] Hamada, T., et al. Size-dependent partitioning of nano/microparticles mediated by membrane lateral heterogeneity. Journal of the American Chemical Society 134(34) (2012): 13990-13996.
- [85] Li, S. and Malmstadt, N. Deformation and poration of lipid bilayer membranes by cationic nanoparticles. Soft Matter 9(20) (2013): 4969-4976.

- [86] Hamada, T. and Yoshikawa, K. Cell-sized liposomes and droplets: Real-world modeling of living cells. Materials 5(11) (2012): 2292.
- [87] Campelo, F., Arnarez, C., Marrink, S.J., and Kozlov, M.M. Helfrich model of membrane bending: From Gibbs theory of liquid interfaces to membranes as thick anisotropic elastic layers. Advances in Colloid and Interface Science 208(0) (2014): 25-33.
- [88] Prato, M., Kostarelos, K., and Bianco, A. Functionalized carbon nanotubes in drug design and discovery. Accounts of Chemical Research 41(1) (2008): 60-68.
- [89] Allen, M.J., Tung, V.C., and Kaner, R.B. Honeycomb carbon: A review of graphene. Chemical Reviews 110(1) (2009): 132-145.
- [90] Wang, K., et al. Biocompatibility of graphene oxide. Nanoscale Research Letters 6(1) (2010): 1-8.
- [91] Choi, H., Kim, H., Hwang, S., Choi, W., and Jeon, M. Dye-sensitized solar cells using graphene-based carbon nano composite as counter electrode. Solar Energy Materials and Solar Cells 95(1) (2011): 323-325.
- [92] Kasry, A., Afzali, A.A., Oida, S., Han, S.-J., Menges, B., and Tulevski, G.S. Detection of biomolecules via benign surface modification of graphene. Chemistry of Materials 23(22) (2011): 4879-4881.
- [93] Li, H., Pang, S., Wu, S., Feng, X., Müllen, K., and Bubeck, C. Layer-by-layer assembly and UV photoreduction of graphene-polyoxometalate composite films for electronics. Journal of the American Chemical Society 133(24) (2011): 9423-9429.
- [94] Liang, J., Wei, W., Zhong, D., Yang, Q., Li, L., and Guo, L. One-step *in situ* synthesis of SnO₂/graphene nanocomposites and its application as an anode material for Li-ion batteries. ACS Applied Materials & Interfaces 4(1) (2011): 454-459.
- [95] Robinson, J.T., et al. Ultrasmall reduced graphene oxide with high near-infrared absorbance for photothermal therapy. Journal of the American Chemical Society 133(17) (2011): 6825-6831.
- [96] Miao, X., et al. High efficiency graphene solar cells by chemical doping. Nano Letters 12(6) (2012): 2745-2750.

- [97] Gracia-Espino, E., López-Urías, F., Terrones, H., and Terrones, M. Chapter 1 - novel nanocarbons for adsorption. in Tascón, J.M.D. (ed.) Novel carbon adsorbents, pp. 3-34. Oxford: Elsevier, 2012.
- [98] Liu, F., Choi, J.Y., and Seo, T.S. Graphene oxide arrays for detecting specific DNA hybridization by fluorescence resonance energy transfer. Biosensors and Bioelectronics 25(10) (2010): 2361-2365.
- [99] Bussy, C., Ali-Boucetta, H., and Kostarelos, K. Safety considerations for graphene: Lessons learnt from carbon nanotubes. Accounts of Chemical Research (2012).
- [100] Shao, G., Lu, Y., Wu, F., Yang, C., Zeng, F., and Wu, Q. Graphene oxide: The mechanisms of oxidation and exfoliation. Journal of Materials Science 47(10) (2012): 4400-4409.
- [101] Di, Y., et al. Functional graphene oxide as a plasmid-based stat3 sirna carrier inhibits mouse malignant melanoma growth *in vivo*. Nanotechnology 24(10) (2013): 105102.
- [102] Tripathi, S.K., Goyal, R., Gupta, K.C., and Kumar, P. Functionalized graphene oxide mediated nucleic acid delivery. Carbon 51(0) (2013): 224-235.
- [103] Liu, Z., et al. Drug delivery with carbon nanotubes for *in vivo* cancer treatment. Cancer Research 68(16) (2008): 6652-6660.
- [104] Varkouhi, A.K., et al. Sirna delivery with functionalized carbon nanotubes. International Journal of Pharmaceutics 416(2) (2011): 419-425.
- [105] Hummers, W.S. and Offeman, R.E. Preparation of graphitic oxide. Journal of the American Chemical Society 80(6) (1958): 1339-1339.
- [106] Marcano, D.C., et al. Improved synthesis of graphene oxide. ACS Nano 4(8) (2010): 4806-4814.
- [107] Tian, B., Wang, C., Zhang, S., Feng, L., and Liu, Z. Photothermally enhanced photodynamic therapy delivered by nano-graphene oxide. ACS Nano 5(9) (2011): 7000-7009.
- [108] Liu, Z., Robinson, J.T., Sun, X., and Dai, H. Pegylated nanographene oxide for delivery of water-insoluble cancer drugs. Journal of the American Chemical Society 130(33) (2008): 10876-10877.

- [109] Zhang, Y., et al. Mechanistic toxicity evaluation of uncoated and pegylated single-walled carbon nanotubes in neuronal PC12 cells. ACS Nano 5(9) (2011): 7020-7033.
- [110] Pasut, G. and Veronese, F.M. State of the art in pegylation: The great versatility achieved after forty years of research. Journal of Controlled Release 161(2) (2012): 461-472.



APPENDIX

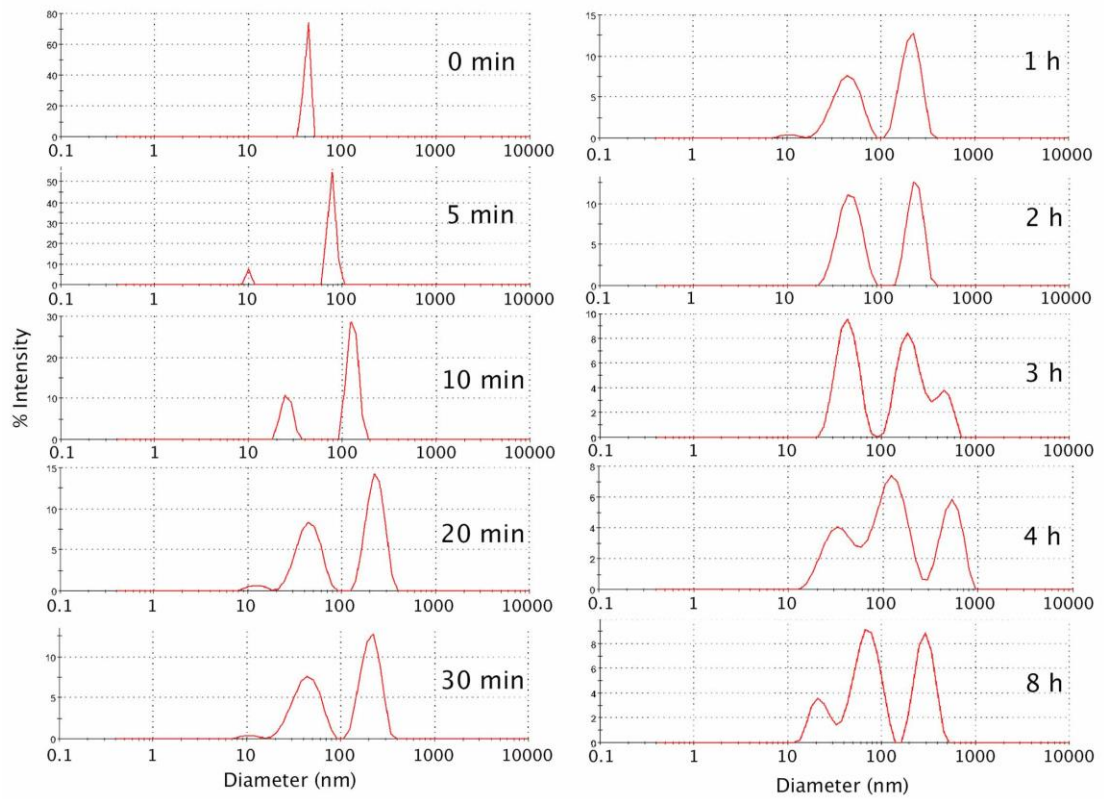


Figure A1 Hydrodynamic size distributions of an aqueous suspension of OCSs obtained at various times post sonication.

VITA

Miss Jiraporn Seemork was born on May 3, 1987 in Bangkok. She received a Bachelor's Degree of Science in Chemistry from Kasetsart University in 2009. After that, she received a Master degree in the Program of Petrochemistry and Polymer Science, Faculty of Science, Chulalongkorn University. She has started Doctoral degree in the Program of Petrochemistry, Faculty of Science, Chulalongkorn University under the supervision of Associate Professor Supason Wanichwecharungruang. After that, she has started Dual Doctoral degree between Chulalongkorn University and Japan Advance Institute Science and Technology (JAIST) in 2013. She has started Doctoral degree in school of Materials science, JAIST under the supervision of Professor Masayuki Yamaguchi.

Her address is 422/740 Ratchavithi Road, Tungphayathai, Ratchathewi, Bangkok 10400, Tel. 086-0526360.